Improving
Persistent Scatterer Interferometry Results for Deformation Monitoring

(Case study on the Gardanne mining site)

Sami Samiei-Esfahany
MSc. Geomatics

TU Delft

Improving
Persistent Scatterer Interferometry results for Deformation Monitoring

(Case study on the Gardanne mining site)

MSc. Geomatics
Thesis

TUDelft

Delft University of Technology

_____

Sami Samiei Esfahany
July 2008

Mathematical Geodesy and Positioning (MGP)
Department of Earth Observation and Space Systems
Faculty of Aerospace Engineering, Delft University of Technology

Supervisors: Prof.dr.ir. R.F.Hanssen,
                  Ir. F.J. van Leijen
Co-Reader: C.N. Bremmer, MSc. (from TNO)
Chairman of the defense committee: Dr.ir. B.Gorte

Preface

This thesis is the product of one year research as the final part of the Geomatics master program at Delft university of technology. The story of this MSc. project starts during the *radar remote sensing and deformation monitoring* course in the Spring of 2006 when I was introduced to a relatively new space-geodetic technique: *persistent scatterer interferometry (PSI)*. For me as a student with the background in geodesy and surveying engineering, this new technique with capability of wide scale measuring of the earth's surface deformation with a few millimeters accuracy from 800 km out in space was both impressing and fascinating. This was the main motivation to choose my master thesis topic related to deformation monitoring by PSI.

From a perspective of Geomatics engineering, PSI is perfectly embedded in the interdisciplinary context of the Geomatics program including acquisition, processing and application of geo-information. With combining the characteristics of large-scale electromagnetic imaging (Remote sensing) and quantitative distance measurement (one of the basic geodetic observables), PSI includes a lot of topics related to acquisition of geo-information. From processing point of view, this technique requires a vast processing steps such as time series analysis and signal processing, multivariate geo-statistics, adjustment and testing theory, image processing, and GIS analysis and visualization for interpretation of results. Finally, the PSI results can provide indispensable information about earth's surface deformation in different application fields (especially related to geo-hazard studies) such as ground subsidence detection, monitoring of potentially unstable structures, seismic and volcanic deformation analysis, and landslide monitoring.

The radar remote sensing group at TUDelft has been involved in development of a methodology for geodetic deformation analysis using radar interferometry during the last decade. The main focus of activities is on stochastic aspects of entire process and products of radar interferometry, and on developing autonomous capabilities in InSAR and PSI processing. In this work, I hope to contribute to improved PSI methodology for extending its capabilities in deformation monitoring.

Acknowledgments

I would like to take this opportunity to recognize the ones who have been supportive on finalizing my thesis and express my appreciation to them. First of all, I would like to thank my supervisor Ramon Hanssen for his great supervision and for the critical but constructive feedbacks and comments he provided me. He continuously challenged me to make further improvements, which greatly enhanced the quality of the thesis. I am also most indebted to my daily supervisor Freek van Leijen for his guidance through the early months of confusion about PSI concepts and algorithm, for his new ideas and advices, and for his patience during reading and correcting the draft of this thesis. I would also thank Ben Gorte, coordinator of the Geomatics program, for his helps and supports during my study in delft. I am grateful for the chance he gave me to attend Envisat Symposium 2007. The ideas which I gained from this conference helped me a lot in defining the direction of this research. Furthermore, I like to thank the members of the Delft radar group for providing nice environment for research and also the valuable discussions that I had with them about my results. Special thanks to Petar Marinkovic and Freek van Leijen for their helps in computer stuff and InSAR processing. I remember that I was stopping by their office with a new question each 10 minutes some days. Thank you guys. I would also like to thank Tjerk Bermon for providing the

code of the PSI results visualization.

I am greatly thankful to all my friends in Delft. Special thanks to Siamak and Kasra for their support and care which helped me to overcome my not too few moments of depression during my thesis project. I greatly value their friendship. I would like to deeply thank all my friends (Ghazale, Sheida, Siamak, Katayoon, Anahita, Mahtab, Kasra, Arman, Saman, and Nikoo) whose rooms were *occupied* by me during the last months of my project, with special thanks to Mahtab for her support and kindness during the first months of writing this thesis. I would also like to thank my aunt Giti and her husband Jalal for their great hospitality and kindness during my stay in Brussels.

Last and most importantly, I would like to thank my parents. I am extremely grateful to my mother for her continuous love, support, and encouragement in every stage of my life. I would like to thank her to make my studies possible and pleasant. I would also like to memorialize my father who was enthusiasticly looking for my graduation, and was always encouraging me to continue my studies in the higher levels. Unfortunately I lost him during the last steps of my thesis project. It is difficult to express how much he was meant to me. Thank you father for all your supports and love which you gave me in my life and during my study abroad.

Sami Samiei-Esfahany
Delft, The Netherlands
August 2008

Abstract

The persistent scatterer interferometry (PSI) is a relatively new technique in radar interferometry which has matured, within a last decade, to a practical technique for measuring the deformation of the Earth's surface. PSI overcomes the main limitations of conventional InSAR methods by identifying radar targets, called persistent scatterers (PS), which have stable backscattering characteristics in time. In 2003, ESA (European space agency) initiated the PSI Codes Cross-comparison and Certification (PSIC4) project to produce reliable information about accuracy and validity of PSI methodologies. The results of the experiment clearly indicated that different PSI approaches resulted in different number of detected PS (or PS density). Especially in deforming areas with strong deformations, the experience shows the low PS density. This causes that main areas of subsidence could not be assessed and identified. This lack of PS in deforming areas raises the hypothesis of type-I errors (falsely rejected PS) due to imperfections in the mathematical model of PSI processing. The background of this thesis is formed by the idea of using the results of the PSIC4 study to evaluate algorithm performance and assess which approaches are most suitable to retrieve reliable deformation parameters at a high spatial density. In this study, the contribution of four different sources of type-I errors is investigated, and some approaches to improve the PS density are proposed. The Gardanne mining area (the test site for PSIC4) was chosen as the case study for validation of the proposed approaches. The following optimizations are addressed in this study.

Initial network optimization. The first step in the PSI algorithm is to establish a reference network of most coherent points, called 1st order PS (PS1). The points are initially selected per previously defined grid cells based on their amplitude variation in time (amplitude dispersion). Applying an alternative approach to have at least one PS1 candidate in each grid cell (even with large amplitude dispersion) results in denser network in deforming areas, leading to significant improvement in the PS density.

Optimized atmospheric phase screen (APS) estimation. The APS estimation approach including trend and turbulence estimation is presented and applied on the Gardanne dataset. The estimated APS signals are compared against tandem interferograms. This comparison shows the better performance of the new approach than the conventional approach which does not include the trend estimation. This optimization also results in 35% improvement in the PS density. Also, the new method for vertical stratification estimation is presented based on the linear relation between stratification signal and elevation. The results show that the estimated stratification signal is either not significant or it is not captured properly by the proposed method. This can be due to the low level of details of the used DEM, or the low signal to noise ratio of the stratification signal.

Azimuthal subpixel position estimation. The new method for detection of pixels with large azimuthal subpixel position is presented. It is shown that pixels with a large azimuthal subpixel position can be detected by evaluating the correlation between their residuals and Doppler baselines. Three different methods are proposed to deal with the azimuthal subpixel position of PS. Applying these method on the Gardanne dataset reveals that it is better to deal with an azimuthal subpixel position stochastically rather than functionally. Adaptation of the stochastic model for detected pixels with large azimuthal subpixel position results in 9% improvement in the PS density in the Gardanne deforming area.

Non-linear deformation modeling The sequential hypothesis testing methodology with adaptive deformation models is applied. The proposed method shows to be an effective and resulted in an increase in the number of detected PS. Especially the double breakpoint deformation model shows effective capability in detection of

PS in areas in which the deformation mechanism can be characterized by two breakpoint. The improvement in the PS density significantly improves the results in capturing the deformation signal. However, the results using adaptive deformation models are more affected by unreliable estimation of ambiguities (or unwrapping errors).

In addition to these optimizations, the new approach for the final selection of PS is presented. Spatio-temporal consistency (STC) is introduced as a quality assessment for the final selection of PS. The advantage of using STC is that it can reduce the dependency of the PS quality assessment to the assumed deformation model and therefore it is better indicator for the observations precision.

Integration of all proposed optimizations together results in 236% improvement in the number of detected PS in the Gardanne deforming area, leading to the improved identification of the Gardanne deformation field. Results of the study show that application of the proposed optimizations can improve the PS density. However, detected PS in areas with fast deformation mechanisms suffer from the unreliable estimation of ambiguities (unwrapping errors), resulting in unreliable estimates of deformation time series. The main reason for this localized effect (as it occurs mostly in deforming areas) is the fast evolution of deformation mechanisms. For example, in the case study of this thesis, the deformations range from few centimeters up to some decimeters occurred in few months. These deformations are strong "fast deformation" for the view point of C-band radar (with wavelength of 5.6 cm) with at most monthly acquisition of ERS data. Different methods with restricted or relaxed conditions for removing unwrapping errors are presented. The decision for removing unwrapping errors from final selected PS or relaxing the acceptance condition of unwrapping errors is dependent to the application of PSI results. However, in order to deliver the PSI results including unwrapping errors to end users, a PS quality description which contains the quality of estimated ambiguities is required.

.

Contents

List of Figures

List of Tables

Chapter 1

Introduction

1.1 Background

In the last decades, interferometric synthetic aperture radar (InSAR) has shown great capability in detecting and measuring land ground deformation with accuracies starting at the sub-cm level on a wide spatial scale. Numerous studies have reported successful results in monitoring the earth's surface deformation caused by earthquakes (Massonnet et al., 1993; Zebker et al., 1994; Hanssen et al., 2000), volcanism (Massonnet and Vadon, 1995; Amelung et al., 2000), subsidence phenomena (Hanssen et al., 1998; Amelung et al., 1999; Shimoni et al., 2002) and ice motion (Joughin, 1995; Meyer, 2004). While InSAR has proven very effective in measuring different deformation phenomena, the obtained results revealed the main limitations of the technique. Under unfavorable conditions, i.e. smaller displacement in more humid environments and over a long time period, InSAR may not observe the deformation due to the atmosphere interference, temporal decorrelation (i.e., decrease of signal coherence due to changing the scattering characteristics of the earth's surface and incoherent movement of individual scattering elements) and geometrical decorrelation (i.e., decrease of signal coherence due to different viewing angles).

In the late 1990s, it was discovered that some radar targets have stable backscattering characteristics for a period of months or years (Usai, 1997; Usai and Hanssen, 1997), and the phase information of these stable targets (hereafter called Persistent Scatterers or PS) can be used even over a long time period. This led to the development of innovative methodologies called Persistent Scatterer Interferometry (PSI), that enable us to measure earth surface deformation at millimeter level (Ferretti et al., 2000, 2001). In contrast to conventional InSAR, where only a small number of SAR interferograms are analyzed, the PSI technique allows to analyze time series of interferograms. In this way, PSI addresses the three main limitations of conventional InSAR: 1) temporal deccorelation is minimal due to the stable backscattering characteristics of PS, 2) geometrical decorrelation is minimal due to point-like scattering and small size of PS, and 3) atmospheric signal can be modeled and filtered based on the spatial and temporal behavior of the atmosphere. During the last couple of years PSI techniques have provided unique and indispensable information in many different application fields such as land subsidence (e.g., due to water, gas, oil, or minerals extraction), seismic and volcanic movements, landslides, and even deformation monitoring of structures such as buildings, dams, and dikes.

During the Fringe 2003 workshop (Advances in SAR interferometry from ERS and ENVISAT missions) organized by ESA, it was recognized that despite satisfactory PSI results in different applications, there is uncertainty about the accuracy and reliability of the PSI measurements among end users and researchers. The reasons for this concern could be that the nature of PSI algorithms is technically advanced and complex for the end users, while there are different approaches and strategies for PSI processing which could lead to different results, and the potential of the technique in the case of precision and reliability is different for different case studies. This questionability motivated ESA to perform the Persistent Scatterer Interferometry Codes Cross-Comparison And Certification
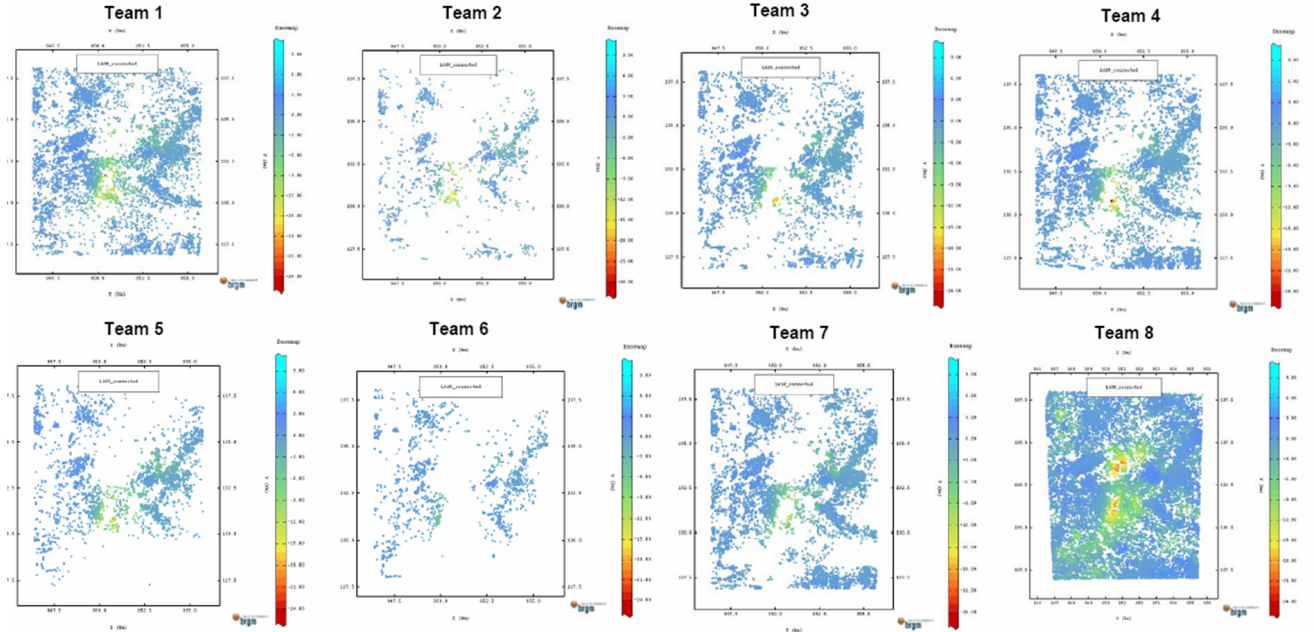
Figure 1.1: *PSIC4 results : scatterplot of detected PS of eight teams participated in the project, each map is centered on the deforming area. Colors show annual linear deformation scaled from -25 (red) to 9 cm/year (blue) (Racoules et al., 2006)*

.

(PSIC4) project to produce reliable information about the accuracy and validity of PSI methodologies. During the project, eight independent radar specialist teams used the same set of SAR data acquired over a test site (Gardanne mining area in France), and processed the data with their own PSI methodology without any a priori knowledge about the nature and location of deformation in the test area. The PSI results of these eight groups were compared against external validation benchmarks such as leveling points and among each other.

The experiment proved to be highly successful in terms of revealing the intrinsic differences in radar processing methodologies. It clearly indicated that different approaches resulted in different results, in terms of spatial point density, temporal deformation behavior, phase ambiguity resolution, and precision and reliability. Results showed a trade-off between one or more of the above characteristics, and a high sensitivity to chosen threshold values. As PSIC4 was a blind experiment, where no a-priori information on the location, magnitude, temporal behavior, and other characteristics of the deformation was available, it raises the question to what extent a-priori information can and should be used in PSI processing. Information, or assumptions, either on temporal or spatial behavior appear to be very important in the processing results.

The background of this thesis is formed by the idea of using the results of the PSIC4 study to evaluate algorithm performance and assess which approaches are most suitable to retrieve reliable deformation parameters at a high spatial density. One of the main results of PSIC4 is the different spatial point density for different processing approaches. The eight maps in Fig. 1.1 show the PS line-of-sight velocity map of each team. These maps correspond to a subset of the SAR dataset processed by each team that has been centered on the deforming area. A first visual assessment of these maps stresses a low PS density in the deforming area for most of the teams. The PSIC4 final report showed that for the case under consideration the main area of subsidence could not or only partly be assessed and identified by all teams except team 8. The main reason for this has been the low density of persistent scatterers in the area of interest. This thesis discusses the main causes of this low PS density, presents some new approaches to improve the density of persistent scatterers, and discusses the price that needs to be paid for higher point density.

1.2 Problem formulation and research objectives

At the start of this study, the main objective of the research was defined as:

> *"present strategies to increase the density of detected persistent scatterers, especially in deforming areas"*

Before discussing potential improvements, it is important to define clearly what we mean with increasing the PS density. We should consider that it is relatively easy to increase the number of PS by decreasing the quality condition (or threshold) of accepting the pixel as PS. That is, there is always a trade off between the quality (e.g., precision and reliability) of PS and density of points. In fact, the acceptable improvement is to increase density without quality compromises.

The main causes of the low PS density in the Delft radar processing methodology can be hypothesized as:

1. **Lack of coherent scatterers in the area:** Here we mean that there are simply no scatterers that are coherent over the time interval of consideration. In other words, the absence of scatterers with stable scattering characteristics.

2. **Pixels missed in initial selection:** As interferograms contains millions of pixels, checking all of them as potential PS is very inefficient and slow in terms of computational time. For this reason, in the first stage of the PSI processing, a subset of pixels is usually selected as PS candidates based on a certain criteria (e.g., temporal amplitude variation), and only these PS candidates are analyzed and tested in the next steps. As a result, there could be undetected PS after the evaluation just because they do not satisfy the criteria to become candidates, hence, their phase behavior is simply not evaluated.

3. **Falsely rejected PS:** These are pixels which are identified as candidates, but during the testing procedure, they are falsely rejected to be PS, whereas they should have been accepted. Hereafter, we call these pixels type-I errors (falsely rejected PS).

In order to formulate potential improvements, we first investigate these main causes of the low PS density. The first cause is dependent on the physical scattering properties of the Earth's surface in the area of interest, and therefore it is not possible to optimize the PS algorithm to deal with it. Second cause can be improved by optimization of initial selection method. Different methods are addressed by Ferretti et al. (2001), Adam et al. (2004), Kampes (2005), and Hooper et al. (2004), and some optimization are proposed by Humme (2007). However, in this research, we decided to process all pixels in the area of interest in order to evaluate the main reason of rejection of PS and also gather statistics about all detected PS and try to comment on a initial selection approach by analyzing these statistics. So this research mainly concentrate on the 3rd cause that is type-I errors.

The PSI processing chain can be divided into two general phases [1]:

1. **Preliminary estimation:** The goal of this phase is to estimate the atmospheric phase in order to separate the atmosphere phase from other effects. This separation is performed using a sequence of filters, as described by Ferretti et al. (2001), at a network of the presumably most coherent pixels or first order PS candidates (PS1c).

2. **Densification:** After estimation of atmospheric phase on 1st order PS, the atmospheric phase of other PS candidates (i,e., second order PS candidates (PS2c)) is interpolated and subtracted. Then the unknown parameters for each PS2c are estimated and the final set of PS is selected based on some quality criteria.

---

[1]Note that the exact meaning of the terminology used here will be discussed in the following chapters.

To narrow the scope of this study, it will focus mainly on the densification step. So, the central research question of this study is formulated as:

> *"How can the density of persistent scatterers be improved by optimizing the PSI densification algorithm?"*

Improvements that are addressed in this study are related to the following aspects.

Atmospheric phase screen estimation. One of the main steps of PSI processing is separation of atmosphere from other effects (e.g. deformation, noise, topography). In the standard PSI methodology, the atmospheric effect is isolated using different spatial and temporal filters on a coarse grid of 1st order PS per acquisition, see e.g., Ferretti et al. (2001). Based on the correlation of the atmosphere in space and its decorrelation in time, a combined smoothing and interpolation operation using kriging is used to derive the APS (i.e., the atmosphere signal for the whole scene). After subtraction of the APS from the original differential phase, the estimation procedure can be repeated for all pixels or 2nd order PS. This approach is optimal for interpolation of the turbulence signal of the atmosphere. However filtered residuals not only contain the turbulence signal but also orbit errors and the vertical stratification signal of the atmosphere, see Hanssen (2001). These effects can be a source of error in the final estimation and cause PS to be falsely rejected especially in areas with low signal to noise ratio (e.g. non-urban areas with high non-linear deformation mechanism). Based on this hypothesis, in this study the APS interpolation step using kriging is extended to a three-steps interpolation procedure, containing de-trending, vertical stratification estimation and kriging. The quality of the estimated APS is analyzed and the sensitivity of the APS estimation on the final PS results is explored.

PS subpixel position. The sub-pixel position of a PS induces an additional phase component in the PSI observation. Neglecting this effect results in imperfection of the mathematical model of PSI estimation causing type-I errors. This study investigates this source of type-I errors and presents different functional and stochastic approaches to cope with it. It is studied how we can detect pixels with subpixel position and how the estimation approach can be optimized to deal with this effect in order to improve the PS density.

Deformation model. In PSI processing, the identification of PS points is largely based on the deviation of the observation from an a priori deformation model. Using an imperfect deformation model causes large deviations between observations and the model, leading to false rejection of the PS (type-I error). Standard PSI processing frequently uses a linear deformation model as a priori model. In this study, it is investigated whether higher order deformation mechanisms are the reason for the low density of PS in the test site. The mathematical model is extended to higher order and more complex models. Moreover, the new strategy based on alternative hypothesis testing is evaluated in order to get denser PS results.

Final selection of PS. The quality assessment of PS candidates for accepting the as PS (e.g., using ensemble coherence or the a-posteriori variance factor) is based on the assumption of ergodicity, i.e., it is assumed that the precision of a scatterer can be estimated by evaluating its behavior in time. This implies that the phase of an arbitrary prior model (usually a linear model) is subtracted before the estimation of the quality. Therefore this quality assessment is also dependent to the model imperfections. In order to reduce this dependency, the new quality assessment based on spatial and temporal consistency of PS is presented and evaluated. Besides the mentioned drawback, all the PS quality assessment methods assume correct estimation of ambiguities and they do not convey any information about the quality of the estimated ambiguities. As a results the final set of selected PS contains PS with incorrect estimated ambiguities (unwrapping errors). Different strategies for removing these errors are presented. It is investigated whether these strategies are too strict and how the quality condition for the unwrapping errors can be relaxed.

At the start of this study, the research questions were limited to only the improvements on the PS densification step. However, during the project it became clear that the density of the initial network (i.e., the result of the preliminary estimation step) has a significant influence on the final density of PS. Therefore, the optimization of the initial network was added to the addressed improvements of this research.

Initial network. The initial selection of 1st order PS candidates is frequently based on a threshold on the normalized amplitude dispersion of pixels. This approach may lead to a limited number of 1st order PS (PS1) in some areas. It is studied whether the density of PS1 can be increased by optimization of the initial selection of 1st order PS candidates and to what extend the density of final PS is sensitive to the density of the initial network.

1.3   Limitations

The PS technique based on the TU Delft implementation is the basis for this study. The principal estimation strategy is not questioned, i.e., a single master stack of complex differential interferograms is used. To narrow the scope, this study will focus on the sources of type-I error only in the PS estimation algorithm. For example, it will not elaborate on errors induced in preprocessing steps and interferogram formation (e.g., coregistration). Neither will it discuss the image selection step or choice of master image and its effect on final results. The temporal unwrapping step is based on the integer bootstrapping method (Teunissen, 2001; Hanssen et al., 2005).

1.4   Outline

This thesis is organized as follows. The review of InSAR principles and standard PSI processing is given in Chapter 2. The PSI processing algorithm is explained in details, and the mathematical framework of PSI estimation is presented. Chapter 3 presents and discusses the methodology which used in this research for different improvements together with approaches for validation of results. Also a Short introduction to the test area (Gardanne mining area) is given and different possible improvements are discussed in detail. The next chapters focus on these improvements. Chapter 4, 5 , and 6 present improvements related to APS interpolation, subpixel position, and deformation model, respectively; Each of them contains a theory part, methodology for improvements, results, validation, and discussion. In Chapter 7, the integration of different proposed approaches is presented followed by discussion about feasibility and contribution of each approach. Chapter 8 reports the final conclusions, and gives recommendations for future research.

Chapter 2

The Persistent Scatterer Interferometry Technique

This chapter reviews the basic concepts of the PSI technique. PSI is an extension of conventional InSAR, so we first present a short introduction of InSAR and its principles and discuss some of its main limitations. We then review the PSI technique and explain in details the PSI processing chain. The mathematical framework of PSI is a basis for the methodology of this study and it is covered in the last section of this chapter.

2.1   InSAR principles

Deformation monitoring using InSAR is based on the principle of distance measurements with electromagnetic waves. If the sensor transmits a pulse to the object and records the return pulse, the time difference between these two pulses shows the distance between the sensor and the object. In other words, the time delay of the echo (reflected pulse) measures the distance of the sensor to the object. This time delay can be measured as the phase difference between transmitted and received wave. With two acquisitions, the difference in measured phases shows the variation in the sensor-object distance.

Similarly, a SAR sensor transmits a signal to the earth and measures the amplitude and phase of the backscattered signal. The phase of the signal that is backscattered from the radar target on the earth is related to the sensor-target distance (Fig. 2.1). A SAR image is actually a set of pixels characterized by both amplitude and phase values which construct the complex image. That is, each pixel in a SAR image has a complex value, or *phasor*. The absolute value of this complex number represents the amplitude of a pixel and its argument represents the phase. In practice, an interferogram is produced by multiplying the first complex SAR image by the complex conjugate of the second image. Generally, the second image is acquired from a slightly different position so it is first resampled to the same geometrical framework as the first image. The phase of the resulting interferogram is the phase difference between the two SAR images.

The basic principle of interferometry is based on measuring these phase differences. Assume that two different radar images are obtained from exactly the same position in space. If nothing has changed, the measured phase of the second image should be exactly the same as the previous phase measurement in the first image. If there is any change in distance between the satellite and the earths surface due to deformation, the phases will differ. This phase difference shows the deformation in the direction of the satellite Line of Sight (LOS). This is based on the assumption that both images have exactly the same acquisition geometry and that the only change between two images is the deformation of the surface. However, in practice there are other factors causing differences between
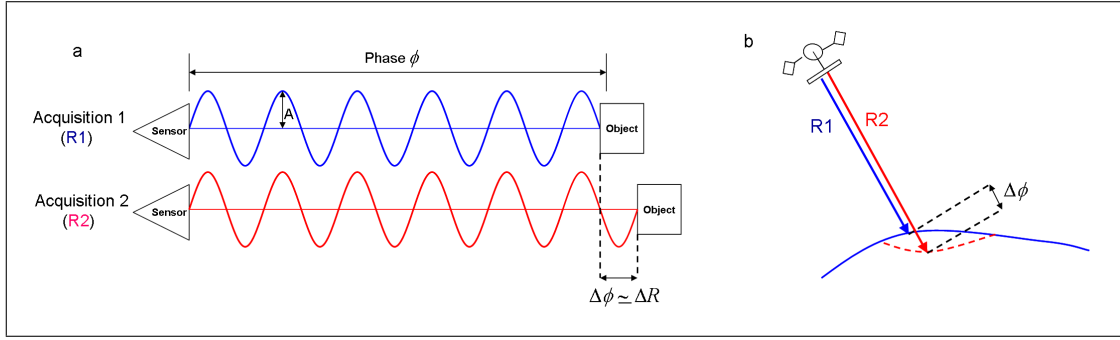
Figure 2.1: *Phase difference measurement: a) relation between a phase difference $\Delta\phi$ and the variation in the sensor-object distance ΔR, b) the same principle for satelite measurements and the earth deformation.*

two images, such as atmospheric conditions, acquisition geometry and scattering characteristics of the earth's surface. These factors superimpose some additional phase differences on the interferometric phase measurements. Therefore, the interferometric phase observation per resolution cell (pixel) contains the contribution of different factors (Hanssen, 2001):

$$
\begin{aligned}
\phi &= 2\pi a + \phi_{topo} + \phi_{defo} + \phi_{orb} + \phi_{atm} + \phi_{scat} + \phi_{noise} \\
&= 2\pi a + \frac{-4\pi B_\perp}{\lambda R sin(\theta)} H + \frac{-4\pi}{\lambda} D + \phi_{orb} + \phi_{atm} + \phi_{scat} + \phi_{noise},
\end{aligned}
\tag{2.1}
$$

The first term on the right hand side (a) denotes the unknown integer number of full phase cycles or phase ambiguity and λ is a Radar wavelength. ϕ_{atmo} is a phase shift due to the atmospheric delay, ϕ_{defo} is the phase shift due to deformation D in the radar line of sight, and ϕ_{scat} is the phase shift due to a change in the scatter characteristics of the earth's surface. The topographic phase ϕ_{topo} is a function of the perpendicular baseline $B_\perp$ (i.e., effective distance between two satellites), incidence angle θ, the slant range R from the master platform to the earth surface, and height above the reference frame H. ϕ_{noise} represents the remaining noise term caused by e.g., thermal noise, coregistration errors, and interpolation errors.

For deformation monitoring, the topographic phase ϕ_{topo} can be removed using an external DEM. This technique is known as Differential InSAR. After removing topography, some residual topographic phase is left due to the DEM inaccuracy. So in differential interferometry Eq. (2.1) is changed to:

$$
\phi = 2\pi a + \frac{4\pi B_\perp}{\lambda R sin(\theta)} \Delta H + \frac{4\pi}{\lambda} D + \phi_{orb} + \phi_{atm} + \phi_{scat} + \phi_{noise},
\tag{2.2}
$$

where ΔH is a residual height. After the removal of the influence of topography, the unknown integer number of full phase cycles has to be resolved in the phase unwrapping procedure. In order to obtain deformation signal, the other unknown parameters have to be estimated and removed as good as possible or a deformation signal should be so dominant to ignore other effects (More information on this topic can be found in Bamler and Hartl (1998), Massonnet and Feigl (1998), Rosen et al. (2000), and Hanssen (2001)). However in most cases it is not possible to retrieve the deformation signal especially due to interference of ϕ_{scat} and ϕ_{atmo} with the deformation signal. These effects form the main shortcomings of the technique which can be summarized as follows:

1. **Temporal decorrelation:** The change in the reflection characteristics (e.g., distribution of scatterers or their electrical characteristics) of the Earths surface within a resolution cell results in a phase difference

contained in ϕ_{scat}, leading to temporal decorrelation. This effect makes the InSAR measurements unfeasible in vegetated areas and in other areas where the scattering characteristics or the positions of the scatters change in time within a resolution cell. As there is a too wide range of temporal changes in different areas, this effect cannot be modeled or predicted quantitatively. Considering only the temporal decorrelation due to movements of the scatterers, Zebker and Villasenor (1992) approximate this effect based on the rms of the displacement.

2. **Geometrical decorrelation:** The different viewing angles from the two platforms (due to the non-zero perpendicular baseline and due to the different squint angle) to the same resolution cell on the ground cause a spectral shift in the observation and introduce a noise in ϕ_{scat} defined as geometric decorrelation. Zebker and Villasenor (1992) approximate this effect as a function of perpendicular baseline: the higher the perpendicular baseline, the more geometrical decorrelation. The critical baseline is the minimum value of $B_\perp$ for which the backscatter signal from each pixel is completely decorrelated. So interferograms with $B_\perp$ higher than the critical baseline cannot be exploited. Geometrical decorrelation is also dependent on the radar cross section so the size of the scatterer (Zebker and Villasenor, 1992; Gatelli et al., 1994). For pixels with totally distributed scatterers, geometrical decorrelation is maximal. In contrast, it is minimal for pixels with a dominant point like scatterer due to the small size of the scatterer.

3. **Atmospheric inhomogeneities:** The spatially and temporally variable state of the atmosphere superimposes another signal (ϕ_{atmo}) that infers with the deformation signal specially in the case of small deformation (e.g., millimeter range). Most of the atmospheric phase variation is due to variation in the distribution of water vapor in the atmosphere and it is locally correlated in space (Hanssen, 2001) . The atmospheric effect is generally only correlated in time on the scale of hours to days. As the time between two acquisition is of the order of one month, the atmospheric signal is effectively decorrelated in time. One of the common methods for reducing atmospheric signal is stacking multiple interferograms acquired over time in order to filter out the temporal decorrelated atmosphere signal (Sandwell and Price, 1998; Sandwell and Sichoix, 2000). However, using stacking any variation in the spatial or temporal nature of deformation over the period of the stack is lost.

2.2 Persistent Scatterer InSAR

As described in the previous section, deformation monitoring using InSAR is hampered by signal decorrelation due to temporal changes in scattering characteristics (i.e., physical or geometrical) of objects on the earth surface. In the late 1990s, it was recognized for the first time that some features have stable backscattering characteristics over long time intervals (Usai, 1997; Usai and Hanssen, 1997). That is, for these targets, ϕ_{scat} is close to zero. This led to the development of an innovative methodology called Permanent Scatterer Interferometry (Ferretti et al., 2000, 2001), which uses these points to estimate the deformation over long time periods and overcome the main limitations of conventional InSAR. The main characteristics of this multi-image processing method are that it utilizes a single master stack of differential interferograms (even long baseline interferograms), and that only coherent pixels (or permanent scatterers) are considered. Since the invention of the permanent scatterer technique by Ferretti et al. (2000), other methods were introduced using comparable concepts, e.g., see (Kampes, 2005; Hooper et al., 2004). Nowadays, Persistent Scatterer Interferometry (PSI) is a term which is used to explain all these methodologies which use a single master of differential interferograms and only consider the coherent pixels (i.e., persistent scatterers) for measuring deformation of the earth's surface.

2.2.1 PSI concepts

The idea of the PSI technique is based on discerning coherent radar signal from incoherent contributions in order to obtain only those observations which are physically interpretable. The degree of decorrelation of radar signals depends on the distribution of scattering centers within a pixel. If the phase of the pixel were determined by just one
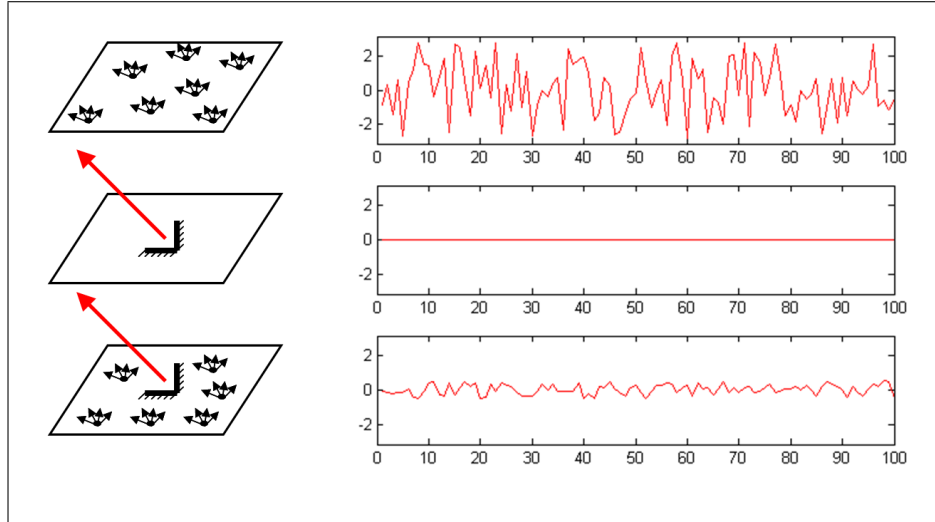
Figure 2.2: *Different scattering resolution cell. Top: a distributed scatterer resolution cell, Middle: point scatterer resolution cell, below: dominant point scatterer resolution cell. The plots on the left show the phase behavior of different scattering resolution cell for 100 simulations.*

stable point scatterer, the decorrelation would be reduced to zero. Although it is never the case for real surfaces, there are pixels which behave somewhat like point scatterers, and for which decorrelation is greatly reduced. Fig. 2.2 shows the difference between the distributed scattering pixel and the pixel with a dominant scatterer (or PS), and shows the different phase behavior for different resolution cells. Hence in an interferogram, a limited number of pixels will exhibit less decorrelation than others. These pixels are called Persistent Scatterers (PS). In other words, a PS is an isolated point with constant backscatter characteristics in time, so the ϕ_{scat} in Eq. (2.2) is approximately zero for these points in all interferograms. The PS scatterers are usually small features (small with respect to the pixel size) with a dominant reflection in a resolution cell. Most of the PS are man made features, so there is a high density of them in urban areas and on infrastructures such as bridges, roads, dams and dikes. Also in mountain areas, some rocks and boulders can play the role of natural PS.

It is possible to avoid many limitations of conventional InSAR by analyzing only PS points which retain some degree of correlation. Due to the stable phase behavior of PS in time, temporal decorrelation becomes minimal in PSI. Furthermore, because of the small dimension of PS with respect to the resolution cell, geometrical decorrelation is also minimal, which leads to good coherence even for interferogram pairs with a large perpendicular baseline. Also, using time series of interferograms allows us to estimate the atmospheric phase and to remove this effect from the final results. The contribution of topography, deformation and atmosphere can be estimated and separated from each other based on their different temporal and spatial behavior . The space-time behavior of these factors can be summarized as: topography is not dependent on time, but scales linearly with the perpendicular baseline; deformation is independent of the baseline, but is correlated in time; and atmosphere is independent of baseline, uncorrelated in time, but spatially correlated per interferogram (Hanssen, 2003). The final result of the PSI technique for deformation monitoring, after removing the atmospheric effect, is time-series of deformation, time-series of atmospheric phase, and residual height of each PS.

2.2.2 PSI processing chain

In this section the algorithms used for PSI processing in this study are described. Fig. 2.3 shows a flow diagram of the process. The whole PSI processing chain can be divided in two main phases:
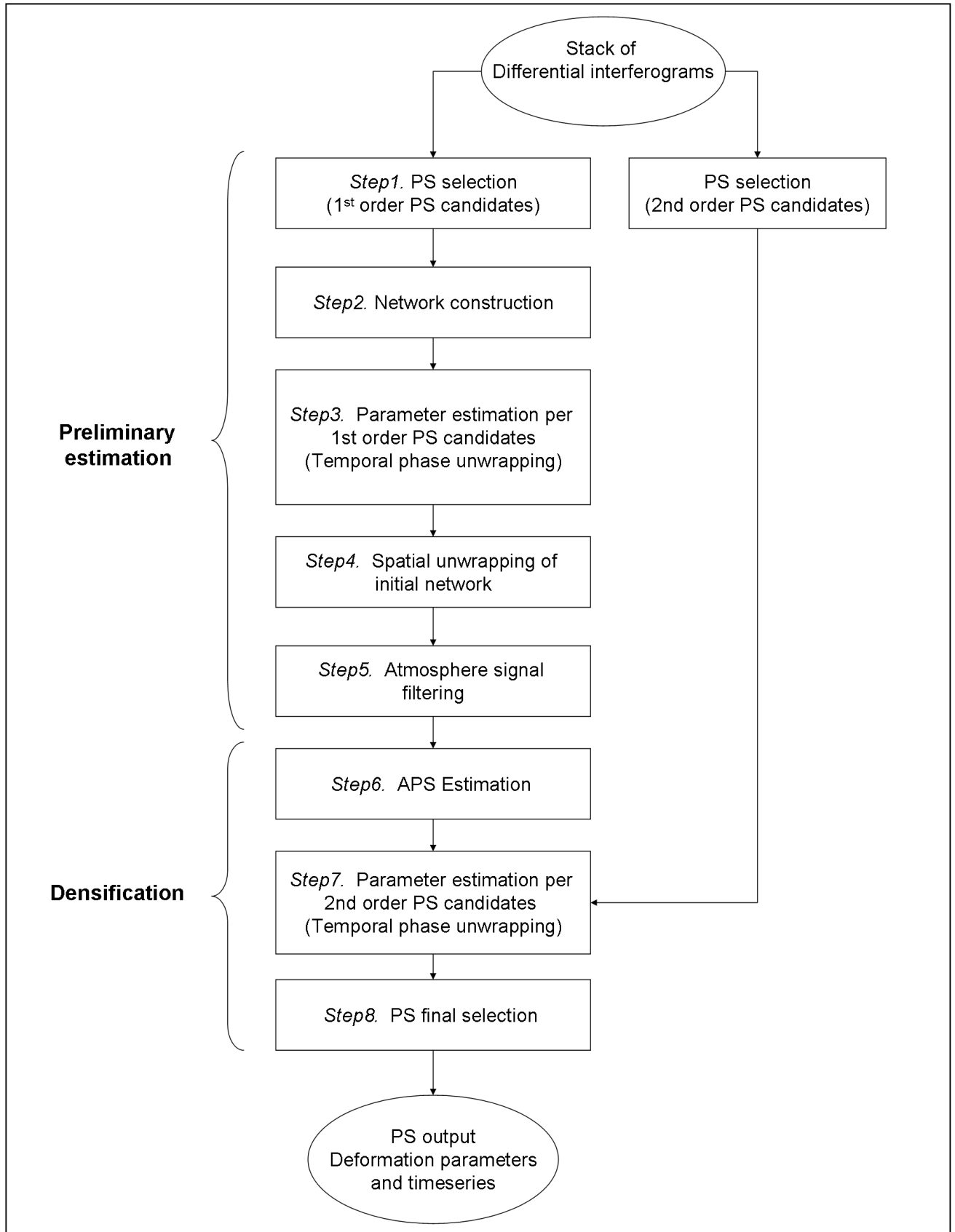
Figure 2.3: *PSI processing flow diagram.*

1. **Preliminary estimation:** The goal of this step is to 1) estimate the atmospheric phase in order to separate the atmosphere phase from other effects and 2) define a first order network of reliable 'benchmarks', which serves as a reference for the densification phase. The first goal is done by filtering of residual phase after estimation of the height residuals and deformation rate, based on the spatial correlation and temporal decorrelation of the atmospheric signal. Preliminary estimation is performed at a network of the presumably most coherent pixels or first order PS candidates (PS1c). This estimation can be separated in five processing steps (i.e., steps 1 to 5) which are described in the next paragraphs.

2. **Final estimation/Densification:** After separation of atmospheric signal from the interferometric phase of 1st order PS (PS1), a full atmospheric phase screen (APS) is interpolated and subtracted from the phase of other PS candidates (second order PS candidates (PS2c)). Then the unknown parameters for each PS2c are estimated. After this estimation, the final selection of PS is performed based on some quality threshold. So, in this step, the initial network of 1st order PS is actually densified by 2nd order PS (PS2). The densification step is divided to three steps (i.e., steps 6 to 8) which are described below.

PSI input

An input of the PSI process is a stack of differential interferograms coregistered to a selected master interferogram. The master image is selected in such a way to maximize the (predicted) total coherence of the interferometric stack, based on the perpendicular baseline, temporal baseline and the mean Doppler centroid frequency difference (Kampes, 2005).

Step1. PS selection

To initiate the PS algorithm, a set of 1st order PS candidates is selected. These PS should have a stable temporal phase behavior. However, the observed wrapped interferometric phase can not be used to identify these stable points due to the juxtaposition of different effects. Therefore, different methods using intensity or amplitude were proposed for initial selection of PS. Examples are the amplitude dispersion (Ferretti et al., 2001) and Signal to Clutter ratio (SCR) (Adam et al., 2004). The amplitude dispersion method is based on an amplitude time series analysis. Each pixel is quantified by the ratio between the standard deviation σ_a and the mean μ_a of the amplitudes through time. The relation of an amplitude dispersion D_a and phase standard deviation σ_ϕ can defined as:

$$D_a = \frac{\sigma_a}{\mu_a} \approx \sigma_\phi. \tag{2.3}$$

Fig. 2.4 shows the relation between σ_ϕ and D_a. We can see that points with a smaller amplitude dispersion index are expected to have a smaller phase standard deviation. Thus, a threshold on D_a can be used as a practical way to select pixels with stable phase behavior. A commonly used threshold is 0.25 for 1st order PS.

In order to use amplitude-based methods for the selection of PS candidates, SAR amplitude calibration is performed prior to the PS selection. The reason for that is to avoid amplitude variations due to sensor characteristics and viewing geometry. Different calibration methods can be used as described in Laur et al. (2002), and Ketelaar et al. (2005).

The main objective of selection of 1st order PS candidates is to establish a reference network of coherent points, which are preferably distributed homogeneously over the area of interest in order to interpolate the estimated atmospheric signal. To ensure a homogeneous distribution of the PS1c, a selection grid is used. For each grid cell the pixel with minimal dispersion is identified and its value is compared to the selection criteria (threshold). To avoid the selection of neighboring pixels, the grid is shifted half a grid size in both directions, each time selecting the optimal pixel (Kampes and Adam, 2003). This guarantees a minimum distance between points equal to the grid width.

In addition to 1st order PS candidates, a set of 2nd order PS candidates is also selected using a higher (less strict) threshold. These pixels are used in the densification phase where the final PS are determined based on their phase behavior. The main reason for this selection is to avoid the evaluation of all pixels in the densification and consequently increase the computational speed. As a result, there may be undetected PS after densification.
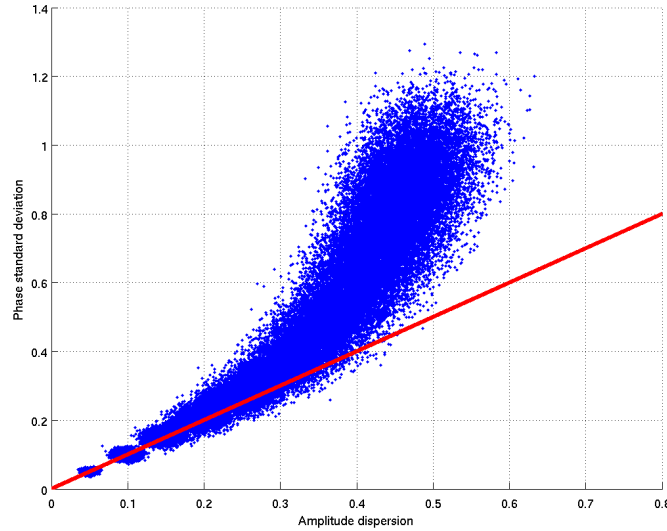
Figure 2.4: *Simulated scatter plot of the relation between amplitude dispersion and phase standard devia-tion.(Ferretti et al., 2001). A complex variable z=s+n is simulated at 3000 points. The signal was fixed to s=1, while the noise standard deviation on the real and imaginary parts of n was gradually incremented from 0.05 to 0.8. 73 data sets are supposed to be available . Small values of the amplitude dispersion index are a good estimate for the phase standard deviation.*

Step2. Network construction

In this step, PS1c are connected in the form of a network to make relative phase observations. The length of the network arcs are restricted to a certain maximum arc length in order to minimizing the influence of some errors such as atmospheric signal delay and orbital errors. Different approach can be used to construct the network such as Delauny triangulation or more redundant network. Note that it is important to have redundant network in order to enable the detection of unwrapping errors in the step 4.

Step3. Parameter estimation per 1st order PS candidates (including ambiguity resolution)

After the formation of a network and calculation of relative phase observation per arc, the phases are unwrapped per arc in time together with the estimation of the parameter of interests. The basic task is to estimate the pa-rameter of interest (e.g., relative deformation rate, residual height difference, etc.) and integer ambiguities from wrapped phase values. There is no direct inversion for this problem (Teunissen et al., 1995). The solution can only be obtained by using the fact that ambiguities are integer numbers. There are various algorithms for temporal unwrapping: ambiguity function (Counselman and Gourevitch, 1981; Ferretti et al., 2001), integer bootstrapping (Teunissen, 2001; Kampes and Hanssen, 2004), and integer least-squares (Teunissen, 1993; Kampes and Hanssen, 2004). An assumption for the deformation model is necessary in this step. Without any a priori knowledge about deformation, a linear deformation mechanism is usually assumed.

Using the ambiguity function (also known as the periodogram technique), the problem is solved by a direct search of the parameter solution space in order to maximize the coherence in time. This approach is simple and quick. However, disadvantages are 1) the solution space is strictly bounded, 2) the computation time increases expo-nentially by adding more unknown parameters, 3) it does not take into account the stochastic properties of the observations and correlation between them.

The integer bootstrapping technique considers the stochastic properties and *some* of the correlation between the observations. The problem is solved by sequential conditional rounding of the ambiguities. In this technique, additional parameters can be easily added to the model without increasing the computation time. However, it requires a priori knowledge about the stochastic properties of the observations, i.e., covariance functions describing

the temporal behavior of the atmosphere and deformation phenomena in the area of interest. Especially in the areas without a priori knowledge about deformation mechanism it is difficult to construct the covariance function of the deformation. Kampes (2005) proposed to use Variance Component Estimation (VCE) to estimate the variance-covariance (vc) matrix of the observations per arc directly from the data. In this way, the vc matrix is not dependent on any a-priori assumptions. The bootstrapping technique is based on the mathematical model described in the next section (Section 2.3).

The integer least-squares technique accounts for the full stochastic properties and correlation between the observations. The mathematical framework is the same as for the bootstrapping technique. Besides the properties of bootstrapping, the advantage of integer least-squares is that the maximum likelihood solution is obtained in the case of normal distributed data. However, the computation time of the technique is larger.

Step4. Spatial unwrapping in initial network

After parameter estimation per arc, the unwrapped (absolute) interferometric phases and parameters of interests are relative in space. So they should be spatially unwrapped and integrated with respect to a single reference point (reference PS) in order to obtain absolute values [1]. Assuming that all ambiguities are estimated correctly, spatial unwrapping can be carried out simply by path integration of temporally unwrapped phases without residues. However, in practice, non-zero residues are found at the arcs of the network, due to incorrect relative estimations at certain arcs due to noise in the observations. So, the unwrapping errors should be detected and corrected. This is done by using the spatial network in a 3-step procedure:

1. The arcs with very low temporal coherence estimates (i.e., with large least-squares residues) are removed.

2. Arcs which cannot be evaluated are removed. In order to detect unwrapping errors the PS should be connected by at least three arcs (with 2 arcs, it is also possible to detect the error, however by using 3 arcs we can decide which one is wrong). So the 1st order PS candidates which are connected by less than 3 arcs are removed.

3. The unwrapping errors are identified and corrected until the whole network fits. Also, points surrounded with several removed arcs are removed.

After identification and adaptation of unwrapping errors, the remaining points in the initial network can be assumed to be unwrapped correctly. These points form the set of 1st order PS. The parameter of interests are estimated once again with corrected unwrapped phases.

The choice of reference point is arbitrary, because the relative accuracy between points does not depend on the reference point choice. However, for interpretation purpose it is more convenient to choose the reference point in an area that is assumed to be not affected by any deformation. Note that all the final results of PSI are relative to this reference point. For absolute interpretation, the deformation parameters have to be connected to an external datum.

Step5. Atmosphere signal filtering

Once the unwrapped phases are obtained per 1st order PS, atmospheric delay phases can be filtered. As topography and modeled deformation (e.g., linear) were estimated already in step 3, the residual phase includes atmospheric delay, unmodeled deformation, orbit errors, and noise. In the filtering step, the contribution of atmosphere (and orbits) is separated from unmodeled deformation. This filtering is based on the assumption that the atmospheric effect is uncorrelated in time, whereas the unmodeled deformation is temporally correlated. So, the separation can be performed using a high pass filter of residual phases in the time domain, as suggested by Ferretti et al. (2000). Note that the filtered phase contains not only atmosphere and orbit effects but also noise. The noise effect is separated from the atmosphere in the next step.

Step6. Prediction of atmosphere phase screen

After separation of the atmospheric phase contribution of the 1st order PS, the atmospheric signal for the whole

---

[1] Here we mean absolute with respect to the reference PS.

scene is predicted per interferogram using Kriging (BLUP) interpolation. The result is known as the atmospheric phase screen (APS). Kriging uses a covariance function (or variogram) which describes the spatial behavior of the atmosphere in order to estimate APS. This interpolation acts as a low pass filter in the spatial domain. As atmospheric signal is spatially correlated in contrast to noise effect which has no correlation in space, Kriging with nugget filtering is used to remove the noise effect.

After prediction of the atmospheric phase for each pixel, this signal is subtracted from the original interferometric phase.

Step7. Parameter estimation per 2nd order PS candidates (including ambiguity resolution)
Once all interferograms are corrected for atmospheric effects, the interferometric phases are unwrapped and the parameters of interest are estimated for all 2nd order PS candidates. Effectively, each PS2c is unwrapped relative to the closest PS1c. One of the three methods used in step 3 can be used.

Also it is possible to test the estimated ambiguities in this step. If each PS2c is unwrapped relative to three closest PS1c, it is possible to check the correctness of the ambiguities. When all three independent estimates are equal, the pixel is fixed. It is also possible to relax this condition and accept a PS when at least two of the three estimates are equal. The output of step 7 consists of estimated ambiguities and other parameters of interests for each 2nd order PS candidate.

Step8. PS final selection
After estimation of the unknown parameters and integer ambiguities, the corresponding PS candidate is tested and a final set of PS is selected. There are two general quality criteria which can be used for accepting a PS-candidate as a PS:

1. **temporal ensemble coherence (Ferretti et al., 2001)**: In the standard PSI technique the absolute value of the complex ensemble coherence

$$\hat{\gamma}_{x,y} = \frac{1}{N} \sum_{n=1}^{N} \exp(je_{x,y}^n) \tag{2.4}$$

   is used as a quality criterion for accepting PS, where j is the imaginary unit, N is the number of interferograms, and $e_{x,y}^n$ is the difference between observations and modeled DD phase between points x and y in interferogram n. The "hat" in $\hat{\gamma}$ is used to emphasize that Eq. (2.4) represents the estimation of the unknown coherence. PS candidates which have $\hat{\gamma}$ larger than a certain threshold are accepted as PS.

2. **a-posteriori variance factor**: Kampes (2005) introduced the a-posteriori variance factor as a testing criterion for accepting a PS. This factor is defined as:

$$\hat{\sigma}^2 = \frac{e^T Q_\psi^{-1} e}{r}, \tag{2.5}$$

   where e is the vector of residuals between the unwrapped phase and the deformation model and r is the redundancy in the functional model (i.e., number of observations minus number of estimated parameters). A $\hat{\sigma}^2$ of 1.0 indicates that the covariance matrix used in the estimation process correctly describes the dispersion of the observations. A value of 2.0 means that the stochastic model used is a factor two too optimistic (assuming that the functional model is correct). PS candidates which have $\hat{\sigma}^2$ smaller than a certain threshold are accepted as PS.

The final set of PS is the union of PS1 and PS2. For final PS, the topographic height (i.e., subtracted topography plus estimated height residual), deformation parameters, atmospheric phase, and residual phase (assumed to represent unmodeled deformation) are known relative to a single reference point.

2.3   Mathematical framework

In the PSI processing chain, the parameter estimation step (i.e., steps 3 and 7) is based on the mathematical model which consist of the functional and the stochastic model. The functional model describes the relation between the observations and the unknown parameters, whereas the stochastic model formulates the stochastic properties of the observations.

The general mathematical model for PSI is formulated using the Gauss-Markov model:

$$
\begin{aligned}
E\{y\} &= Aa + Bb \\
D\{y\} &= Q_y,
\end{aligned}
\tag{2.6}
$$

where the first part shows the functional model and the second part the stochastic model. $E\{.\}$ is the expectation operator, $D\{.\}$ the dispersion, y the vector of phase observations, a is the vector of integer valued ambiguities and b represents the unknown real valued parameters. A and B are design matrices which describe the functional relation between the observation and the integer- and real-valued unknown parameter vectors respectively. Q_y is the covariance matrix which describes the stochastic properties of the y vector. This mathematical model is based on the double-difference (DD) phase observations. That is, a spatial network among pixels has already been constructed and the estimation of the unknown parameters is performed per arc of the network.

In this section, first the functional model is described, followed by a description of the stochastic model. Finally, the basic concepts of integer ambiguities estimation using the bootstrapping and integer least-squares techniques are presented.

2.3.1   Functional model

The structure of the functional model is based on Eq. (2.2). The functional model for a single master stack, where the master is indicated by a zero and N slave acquisitions, is formulated as:

$$
E\left\{
\begin{bmatrix}
\psi^{01} \\
\vdots \\
\psi^{0N} \\
S^* \\
\Delta H^* \\
D_1^* \\
\vdots \\
D_P^*
\end{bmatrix}
\right\}
=
\underbrace{
\begin{bmatrix}
-2\pi & & \\
& \ddots & \\
& & -2\pi
\end{bmatrix}
}_{A}
\underbrace{
\begin{bmatrix}
a^{01} \\
\vdots \\
a^{0N}
\end{bmatrix}
}_{a}
+
\underbrace{
\begin{bmatrix}
\frac{-4\pi}{\lambda} & \beta^{01} & \alpha_1(t^{01}) & \dots & \alpha_P(t^{01}) \\
\vdots & \vdots & \vdots & \ddots & \vdots \\
\frac{-4\pi}{\lambda} & \beta^{0N} & \alpha_1(t^{0N}) & \dots & \alpha_P(t^{0N}) \\
1 & & & & \\
& 1 & & & \\
& & 1 & & \\
& & & \ddots & \\
& & & & 1
\end{bmatrix}
}_{B}
\underbrace{
\begin{bmatrix}
S \\
\Delta H \\
D_1 \\
\vdots \\
D_P
\end{bmatrix}
}_{b},
\tag{2.7}
$$

where ψ are the DD phase observations, S is the atmospheric delay of the master acquisition, ΔH the residual height, D_p are deformation parameters with $p = 1 \dots P$, λ is the radar wavelength, and α_p describes a deformation model as function of temporal baseline t. β^{0n} is the height-to-phase conversion factor for the nth interferogram:

$$
\beta^{0n} = \frac{-4\pi B_\perp^n}{\lambda R \sin(\theta)}
\tag{2.8}
$$

In the functional model, $(.)^*$ denotes a pseudo-observations needed to solve for the rank deficiency of the system (Kampes and Hanssen, 2004). The rank deficiency is caused by the fact that for each observed phase an ambiguity needs to be estimated, together with the parameters of interest. As a result, the number of unknowns exceeds

the number of observations and the system is under-determined. With the introduction of pseudo-observations, the mathematical model is regularized. Without a-priori knowledge of the topography and deformation in the area, the pseudo-observations are set to zero. Note that this can cause the solution to be biased.

Comparison of Eqs. (2.1) and (2.7) reveals that only the first three phase contributions on the right hand side of Eq. (2.1) are taken into account in the functional model (i.e., phase ambiguities a , ϕ_{defo}, and ϕ_{topo}). The reason is that the expectation value for the scattering phase ϕ_{scat} is assumed to be approximately zero for PS. Atmospheric phase ϕ_{atmo} and orbital phase ϕ_{orb} are not considered based on the assumption that these effects are reduced due to using differential phases between two neighboring PS candidates in the spatial network. Also these effects are already reduced for 2nd order PS candidates in the filtering and APS estimation steps. The remaining atmospheric and orbital phases together with the noise effect ϕ_{noise} are accounted for in the stochastic model.

2.3.2 Stochastic model

The stochastic model contains the statistical characteristics of the observation vector y and is presented in the form of the covariance matrix Q_y. As the observation vector y comprises both DD phase observations and pseudo-observations, the Q_y also has two parts:

$$D\{\underbrace{\begin{bmatrix} \psi \\ y^* \end{bmatrix}}_{y}\} = Q_y = \begin{bmatrix} Q_\psi & 0 \\ 0 & Q_{y^*} \end{bmatrix},$$ (2.9)

where Q_ψ is the covariance matrix of the phase observations, and y^* and Q_{y^*} is the vector of pseudo-observations and its covariance matrix respectively. Q_ψ is defined as:

$$D\{\begin{bmatrix} \psi^{01} \\ \vdots \\ \psi^{0N} \end{bmatrix}\} = \begin{bmatrix} \sigma^2_{\psi^{01}} & & & & \\ \sigma_{\psi^{01},\psi^{02}} & \sigma^2_{\psi^{02}} & & \text{sym} & \\ \sigma_{\psi^{01},\psi^{03}} & \sigma_{\psi^{02},\psi^{03}} & \sigma^2_{\psi^{03}} & & \\ \vdots & & & \ddots & \\ \sigma_{\psi^{01},\psi^{0N}} & \sigma_{\psi^{02},\psi^{0N}} & \sigma_{\psi^{03},\psi^{0N}} & \cdots & \sigma^2_{\psi^{0N}} \end{bmatrix}.$$ (2.10)

Hanssen (2004) constructed the components of Q_ψ by propagating the (co-)variances of the single look complex (SLC) phases, leading to the variances:

$$\sigma^2_{\psi^{0N}} = \sum_{p=i,j} \sum_{q=0,n} \sigma^2_{\phi_p^q} - 2(\sigma_{\phi_i^0,\phi_j^0} + \sigma_{\phi_i^n,\phi_j^n} + \sigma_{\phi_i^0,\phi_i^n} + \sigma_{\phi_j^0,\phi_j^n})$$ (2.11)

and the covariances:

$$\sigma^2_{\psi^{0n},\psi^{0m}} = \sum_{p=i,j} \sigma^2_{\phi_p^0} - 2\sigma_{\phi_i^0,\phi_j^0} - \sigma_{\phi_i^0,\phi_i^n} - \sigma_{\phi_j^0,\phi_j^n} - \sigma_{\phi_i^0,\phi_i^m} - \sigma_{\phi_j^0,\phi_j^m} + \sigma_{\phi_i^m,\phi_i^n} + \sigma_{\phi_j^m,\phi_j^n}$$ (2.12)

where the

- $\sigma^2_{\phi_i^n}$ is total variance of a SLC phase observation, consisting of thermal noise, scattering noise, remained atmospheric and orbital signal for the ith pixel in the nth image.

- $\sigma_{\phi_i^n, \phi_j^n}$ is the covariance between two positions (i.e., ith and jth pixels) at the same time (i.e., nth image). This component is mainly dependent on the atmospheric and orbital signal, so it is a function of the distance between the two points.

- $\sigma_{\phi_i^m, \phi_i^n}$ is the covariance at one position (ith pixel) between two times (i.e., at mth and nth image). This component is mainly contains the effect of temporal coherence.

The index 0 in these factors corresponds to the master image. Assuming approximately equal temporal coherence among the interferograms, equal atmospheric variability for all interferograms, and comparable arc lengths, Q_ψ can be simplified to:

$$Q_\psi = (\sigma_{\phi_p^q}^2 - \sigma_{\phi_i,\phi_j} - \sigma_{\phi^0,\phi^n}) \begin{bmatrix} 4 & 2 & \ldots & 2 \\ 2 & 4 & & \vdots \\ \vdots & & \ddots & \\ 2 & \ldots & & 4 \end{bmatrix}. \tag{2.13}$$

The second part of the stochastic model is the covariance matrix of pseudo-observations Q_{y^*} :

$$D\left\{ \begin{bmatrix} S^* \\ H^* \\ D_1^* \\ \vdots \\ D_P^* \end{bmatrix} \right\} = Q_{y^*} = \begin{bmatrix} \sigma_{S^*}^2 & & & & \\ & \sigma_{\Delta H^*}^2 & & 0 & \\ & & \sigma_{D_1^*}^2 & & \\ & 0 & & \ddots & \\ & & & & \sigma_{D_P^*}^2 \end{bmatrix}. \tag{2.14}$$

where $\sigma_{S^*}^2$ is the variance of master atmospheric delay , $\sigma_{\Delta H^*}^2$ is the variance of the residual height, $\sigma_{D_p^*}^2$ are variances of deformation parameters. Different covariance functions can be used to fill the components of Q_{y^*} based on the time interval and length of the arc and a-priori knowledge about the DEM, the master atmosphere and the deformation mechanism., see Hanssen (2004). The components of Q_{y^*} bound the solution space of the corresponding unknown parameters.

2.3.3 Integer ambiguities and parameter estimation

Using the mathematical model of Eqs. (2.7) and (2.9), the unknown parameters can be estimated by least-squares estimation. The procedure is divided into three steps (Teunissen, 1993):

1. First the float solution is estimated by disregarding the integerness of the ambiguities. So, standard least-squares adjustment is performed to estimate $\hat{a}$, $\hat{b}$ and the accompanying variance matrix

$$\begin{bmatrix} Q_{\hat{a}} & Q_{\hat{a}\hat{b}} \\ Q_{\hat{b}\hat{a}} & Q_{\hat{b}}. \end{bmatrix} \tag{2.15}$$

2. After obtaining the float solution, integer ambiguities $\check{a}$ are estimated by mapping the float ambiguity $\hat{a}$ to the corresponding integer (fixed) ambiguity by a mapping operator $S : \mathbb{R} \mapsto \mathbb{Z}$, so

$$\check{a} = S(\hat{a}). \tag{2.16}$$

There are different integer estimators to obtain the fixed ambiguity. Teunissen (1999) introduced three admissible integer estimators: *integer rounding*, *integer bootstrapping*, and *integer least-squares*. The integer
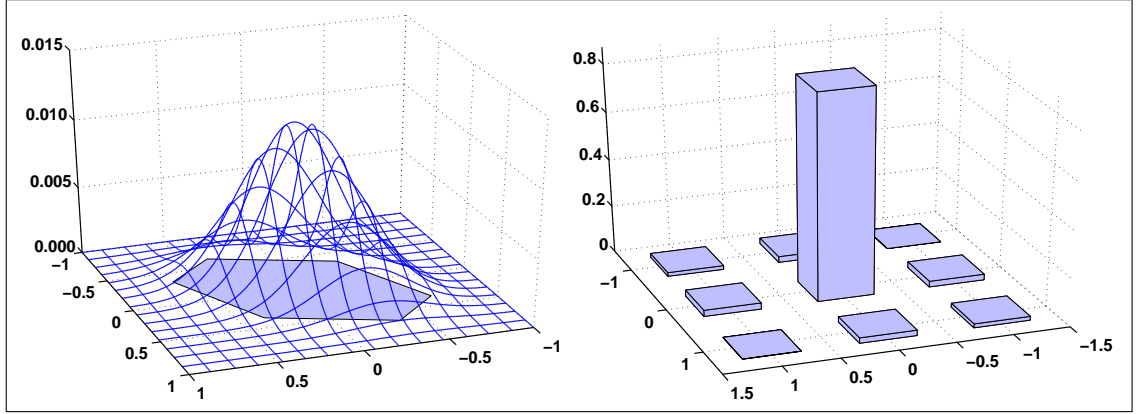
Figure 2.5: *Left: Example of the float ambiguity PDF in 2D, Right: Example of the integer ambiguity PMF in 2D.*

rounding estimator rounds the entries of the float ambiguity solution to their nearest integer values. The disadvantage of the integer rounding method is that it does not take the correlation between float ambiguities into account. In contrast, the integer bootstrapping estimator considers *some* of the ambiguity correlation. The bootstrapping method is based on sequential conditional rounding. The first ambiguity is simply rounded to its nearest integer. Then, the real-valued estimates of the remaining ambiguities are corrected using their correlation with the first ambiguity. In a next step, the second corrected ambiguity is rounded to its nearest integer, and so on (Teunissen, 1998, 2001). The integer least-squares estimator is the only estimator which accounts for all the correlation among float ambiguities by solving the minimization problem (Teunissen, 1993):

$$\min_{a \in \mathbb{Z}} (\hat{a} - a)^T Q_{\hat{a}}^{-1} (\hat{a} - a). \tag{2.17}$$

The integer least-squares estimator obtains the maximum likelihood solution for normally distributed data. The disadvantage of the technique is that its computational time is larger in comparison with the bootstrapping method.

3. Once the fixed ambiguity $\breve{a}$ is obtained by one of the admissible estimators, the float solution of the parameter of interests $\hat{b}$ is updated using the fixed ambiguities. The fixed solution reads:

$$\hat{b}_{|a} = \hat{b} - Q_{\hat{b}\hat{a}} Q_{\hat{a}}^{-1} (\hat{a} - \breve{a}) \doteq \breve{b} \tag{2.18}$$

$$Q_{\breve{b}} = Q_{\hat{b}} - Q_{\hat{b}\hat{a}} Q_{\hat{a}}^{-1} Q_{\hat{a}\hat{b}} + Q_{\hat{b}\hat{a}} Q_{\hat{a}}^{-1} Q_{\breve{a}} Q_{\hat{a}}^{-1} Q_{\hat{a}\hat{b}}, \tag{2.19}$$

where

$$Q_{\breve{a}} = \sum_{z \in \mathbb{Z}} (z - a)(z - a)^T P(\breve{a} = z) \tag{2.20}$$

Hence, the variance of the fixed solution is not only dependent on the variance of the float solution, but also on the chance of success in the ambiguity resolution. This chance of success is denoted by the *success rate* $P(\breve{a} = a)$. Because of its discrete nature, the fixed ambiguities $\breve{a}$ have a probability mass function (PMF) and the fixed solution a multi-modal probability density function (see Fig. 2.5).

Chapter 3

Initial settings and Methodology

This chapter presents the general methodology applied in this study. It introduces the Gardanne mining site and reviews the main characteristics of its deformation field. The specific settings of the PSI algorithm are described, followed by the description of the initial PSI result which is the point of departure for this study. The general methodology for identification and reduction of type-I errors is presented, as well as the methodology for the validation of the final results.

3.1   Gardanne mining test site

This section describes the main characteristics of the Gardanne mining site as summarized by Racoules et al. (2006). the Gardanne mining site is the test site selected for the PSIC4 project. The area of interest is located around the city of Gardanne (South France) in the sedimentary basin of 'I Arc' between the Sainte Victire mountain, the cities of Marselles and Aix en Province, see Fig. 3.1.

The coal exploitation in the area started during the Middle Ages but the structural industrial production began during the 19th century. The maximum of production occurred in the 1965-1993 period. The exploitation of the concession stopped on February 1, 2003. During the period of interest (i.e., the period that radar data were available 1991-2004), the observed ground subsidence is associated to the coal mining exploitation using the long wall mining technique. This technique has particular consequences in terms of size and evolution (fast evolution). With the long wall mining technique, a long wall (about 250 m long typically) of coal is mined in a single slice (typically 1-2m thick). The long wall 'panel' is typically some km long and 250m wide. The long wall equipment consists of a number of hydraulic jacks, which are placed in a long line up to 400 m in length in order to support the roof. The coal is cut by a shearer that moves along the length of the face extracting the coal. As the shearer removes the coal, the equipment move forward into the newly created cavity. As mining progresses, the cavity behind the long wall collapses under the weight of the overlying materials. In fact, typically, when a panel is mined, we expect that half of the displacement is produced in the first 2 months and the residual deformation during the 3 following years (Racoules et al., 2006). A point at the surface can be influenced by several mined panels and therefore the deformation may last on longer periods. Fig. 3.2 shows the long wall panels in the area of interest overlaid on differential InSAR data. This interferometric data was obtained by stacking interferograms between 1995 and 2000 (Racoules et al., 2006).

We can see in Fig. 3.2 that there is no clear relationship between the geological faults in the area and the maximum deformation. Also, it is possible to see that the maximum subsidence during this time interval is related to the westernmost mined panels of both the northern and southern areas, especially panels P1-4, and P24-26. The time
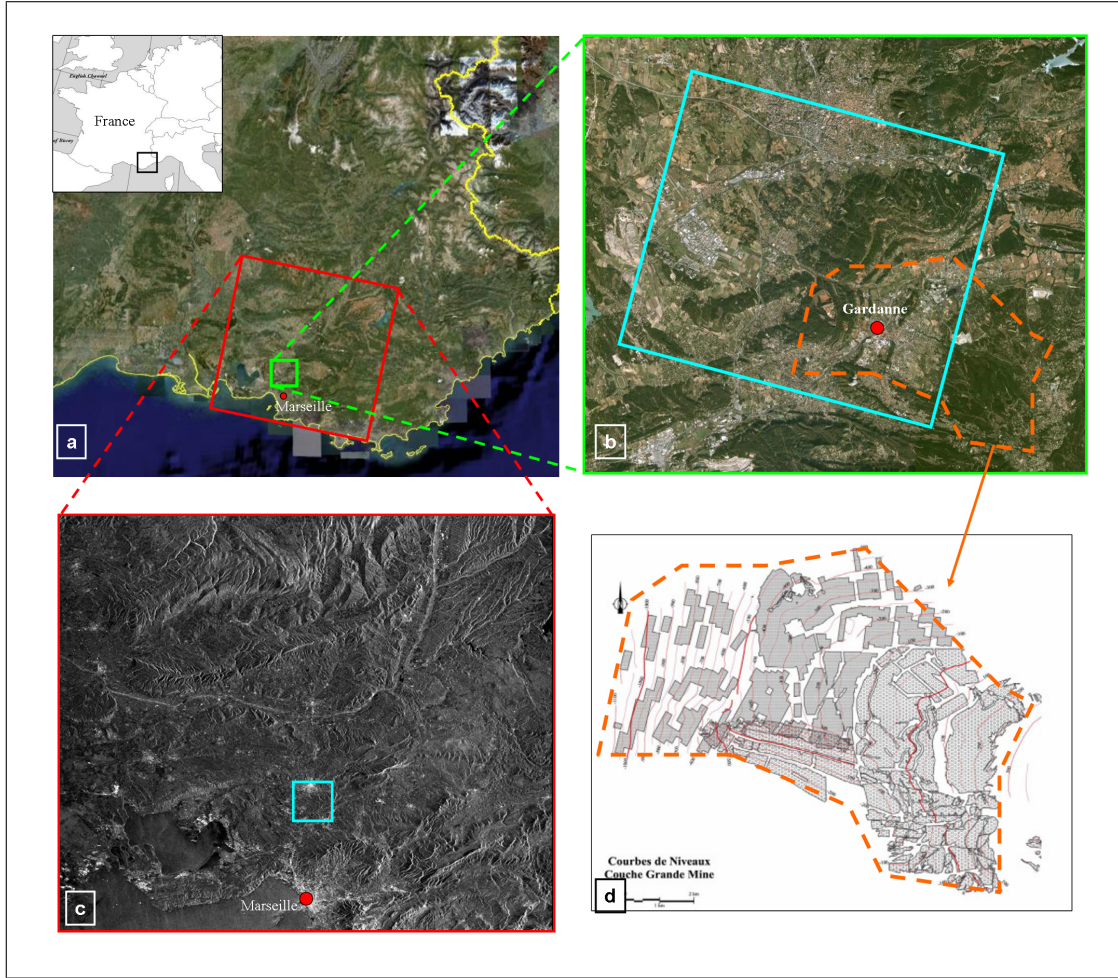
Figure 3.1: *The Gardanne mining area: a) location of the test site, the red rectangle is the location of the SAR scene used in this study, b) the mining area: orange rectangle is the mining area, blue rectangle is the SAR crop which is used in this study, c) The SAR amplitude image and the used crop, d) detailed plan of the underground mining panels (Racoules et al., 2006).*

interval between start and end of the mining activities in these panels are presented in Table 3.1.

Deformation monitoring by leveling

The land deformation in the area has been monitored continuously from 1972 up to 2005 by leveling. The leveling data consists of 12 survey lines along a railway line, along canals, etc. with a point distance of 40 to 50 m at more or less regular time intervals (every 6 months on average). The standard deviation of height differences measured point-to-point is 0.7 mm and the standard deviation of height measurements in 1 km one way leveling is 1.5 mm (Racoules et al., 2006). Fig. 3.3 shows the location of the survey lines overlaid on the location of long wall mining panels and the annual cumulative deformation (i.e., the total amount of deformation that occurred over the time period 1992-2004 divided by time) estimated by leveling data.

Fig. 3.3 confirms that the maximum deformation is related to mining activities in panels P1-4 and P24-26 (see Fig. 3.2). We divides the area in five different subsidence areas (Fig. 3.3b):

1. main subsidence area (S1 area)
2. small subsidence area in Simaiane and Collongue (S2 area)
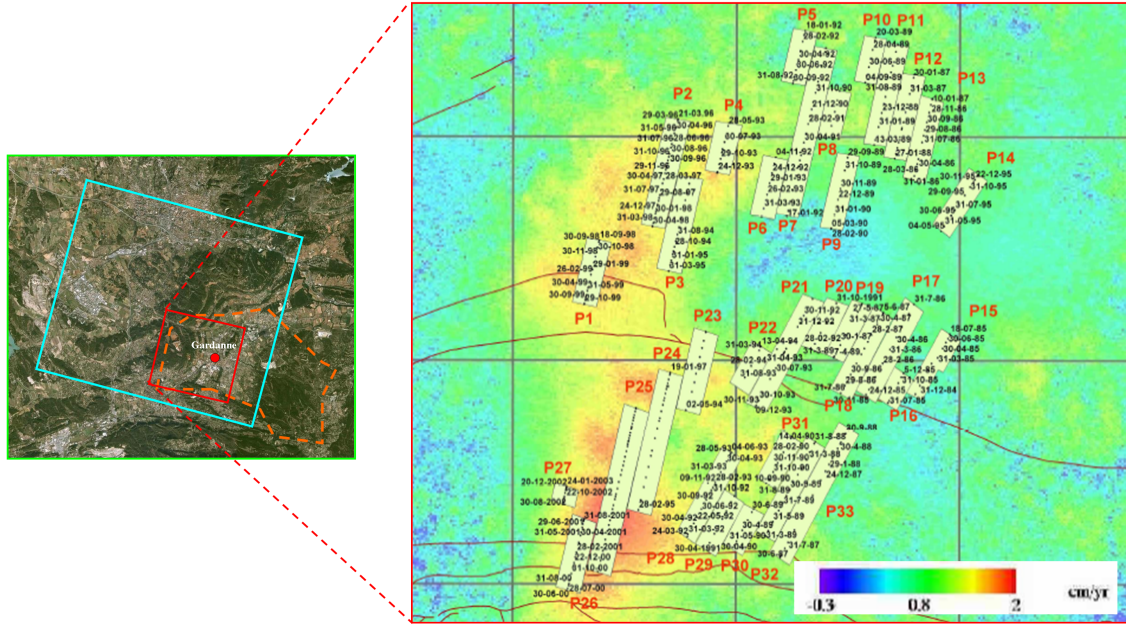
Figure 3.2: *Mining panels constructed during the 1991-2004 time interval, with dates, overlaid on the DInSAR data. Red lines in the right figure are geological faults. Blue rectangle is the SAR crop which is used in this study and orange polygon is the mining area (Racoules et al., 2006).*

Panel	Start time	End time
P1	18/09/1998	29/10/1999
P2	21/03/1996	30/04/1998
P3	31/08/1994	31/03/1995
P4	28/05/1993	24/12/1993
P24	19/01/1997	28/02/1995
P25	31/10/2000	31/08/2001
P26	30/06/2000	26/09/2001

Table 3.1: *Time interval between start and finish of the mining activities in the relevant mining panels.*

3. small subsidence area in Gardanne (S3 area)
4. subsidence area North-West of Gardanne (S4 area)
5. subsidence area west of Gardanne (S5 area).

The leveling data shows that the maximum displacement observed within a year is about 170 mm, and occurs in 1991 (prior to the SAR acquisitions). In average, taking into account the leveling points that remain stable, the average annual displacement is always lower than 5 mm. For a given point, 70 percent of the subsidence occurs within the first three months after the arrival of the mining works in the corresponding area. Two years after, these points became stable. When several works overlapped, their influences cumulate and the point continued to move for more than two years (Racoules et al., 2006).

Based on information we obtained from Fig. 3.3, the characteristics of each subsidence area are summarized in Table 3.2. Note that deformation rates are obtained by qualitative (visual) assessment of the plots and they are not
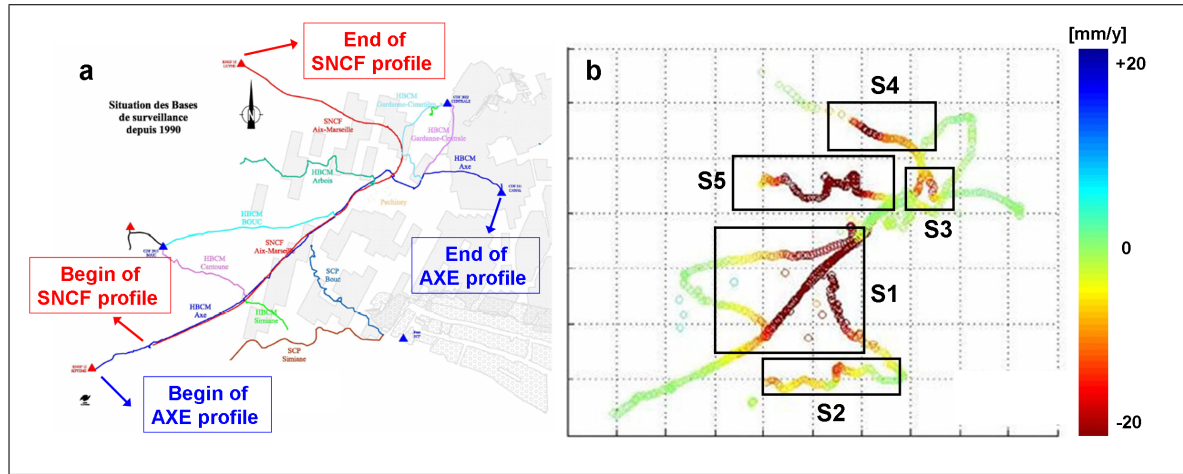
Figure 3.3: *a) Location of the leveling profile. b) Vertical velocities from leveling data, and 5 different subsidence areas (between 1992 and 2005)(Racoules et al., 2006).*

imply exact quantitative measurements. [1]

Name	Related panels	Landscape	mining time interval	Average annual Def.	Maximum annual Def.
S1	P24 abd 25-27	Urbanized/Agricultural	(1995 - 1997) and (2000-2002)	-10 mm/y	$\geq$ 20 mm/y
S2	P25-26	Urbanized/forest	(2000-2001)	-10 mm/y	$\approx$ 20 mm/y
S3	P3-P4 and P6-P8	Urbanized	(1993-1995) and (1991-1993)	-6 mm/y	$\approx$ 10 mm/y
S4	P5-13	Forest/Agricultural	(1991-1993)	-10 mm/y	$\approx$ 20 mm/y
S5	P1-3	Forest	(1994-1999)	-10 mm/y	$\geq$ 20 mm/y

Table 3.2: *Characteristics of different subsidence areas (obtained from (Racoules et al., 2006) based on the visual assessment of the leveling figures*

The detailed time series of the two main leveling sections (SNCF and AXE) are shown in Figs. 3.4 and 3.5. These spatio-temporal profiles show the leveling transect as discrete leveling points on the horizontal axis and time as acquisition date on the vertical axis. The cumulative displacement is color coded. The corresponding subsidence areas are also indicated in these profiles. The section corresponding to the S1 area is extended over the overlapping section of both leveling profiles and shows a distinctive subsidence process starting in the first quarter of 1993 and ending in 2002 which is comparable with mining time interval(see Table 3.2). The SNCF leveling profile also shows deformation in S3 and S4 areas but does not fully cover them. The deformation on S3 is small and started around 1996 and continued until 2002. These dates are not comparable with the mining activities of the related panels. This can be due to the influence of the neighboring mining panels. The S4 deformation started in 1993 and ended in 2002. The starting date of the deformation is comparable with the mining operation, and continuation of the deformation until 2002 can be due to the superposition of S5 deformation.

Landscape and topography

Fig. 3.6a shows the landscape of the deforming areas. We can see that a large part of deforming areas consist of forest and agricultural land which is not optimal for PSI. Figs. 3.6 A, B, and C show examples of the landscape in this area. There is also some deformation in the urbanized area, for example in the S3 area and some parts of the S1 area (see Table 3.2). The mining area is located in the hilly terrain with maximum elevation difference of 400 m. Fig. 3.7 shows the SRTM DEM of the area.

---

[1] As the original leveling data were not made accessible, we can only use the qualitative and graphical information obtained from the PSIC4 final report (Racoules et al., 2006).
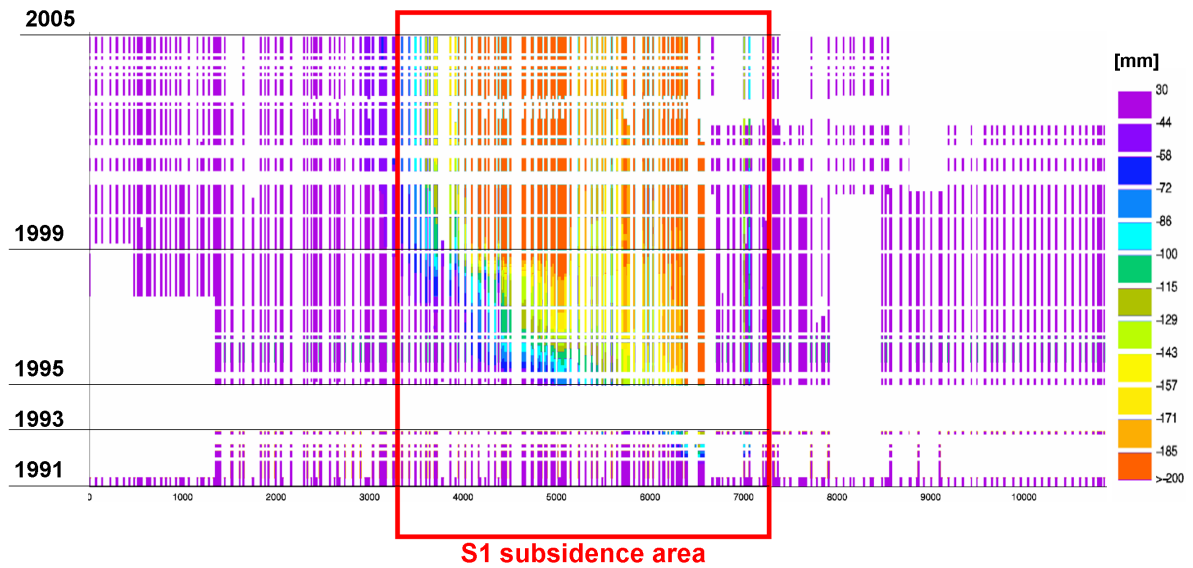
Figure 3.4: *Spatio-temporal profile of the leveling data along leveling section AXE (cumulative displacement in mm; horizontal lower axis: distance in m along leveling line; vertical axis: time; The Red box is the section corresponding to the S1 subsidence area (Racoules et al., 2006).*
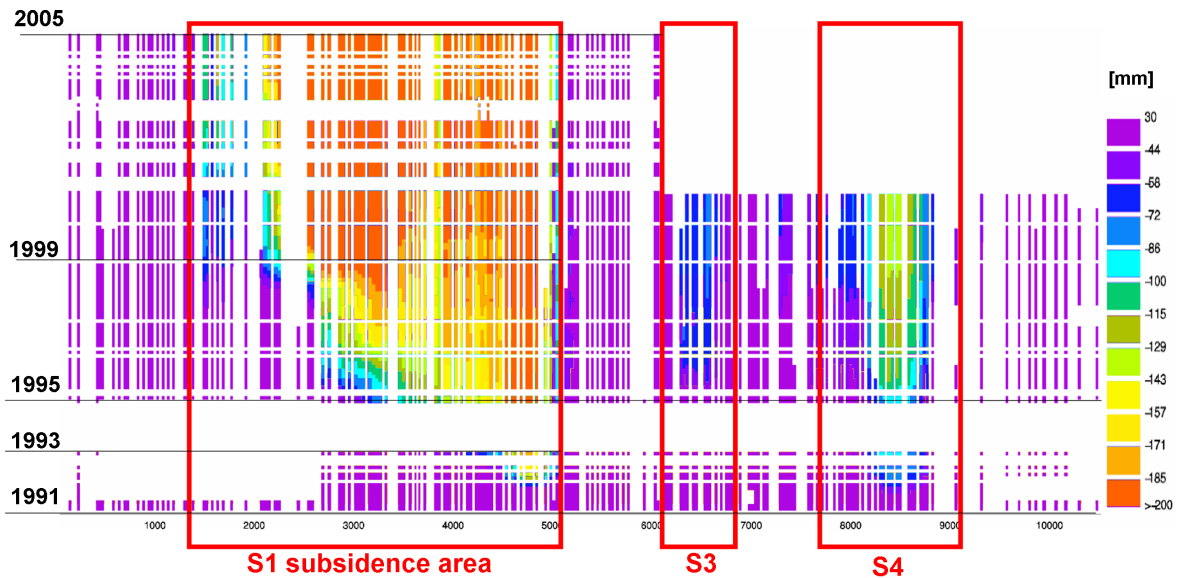
Figure 3.5: *Spatio-temporal profile of the leveling data along leveling section SNCF (cumulative displacement in mm; horizontal lower axis: distance in m along leveling line; vertical axis: time; Red boxes are sections corresponding to S1, S2 and S4 subsidence areas (Racoules et al., 2006).*
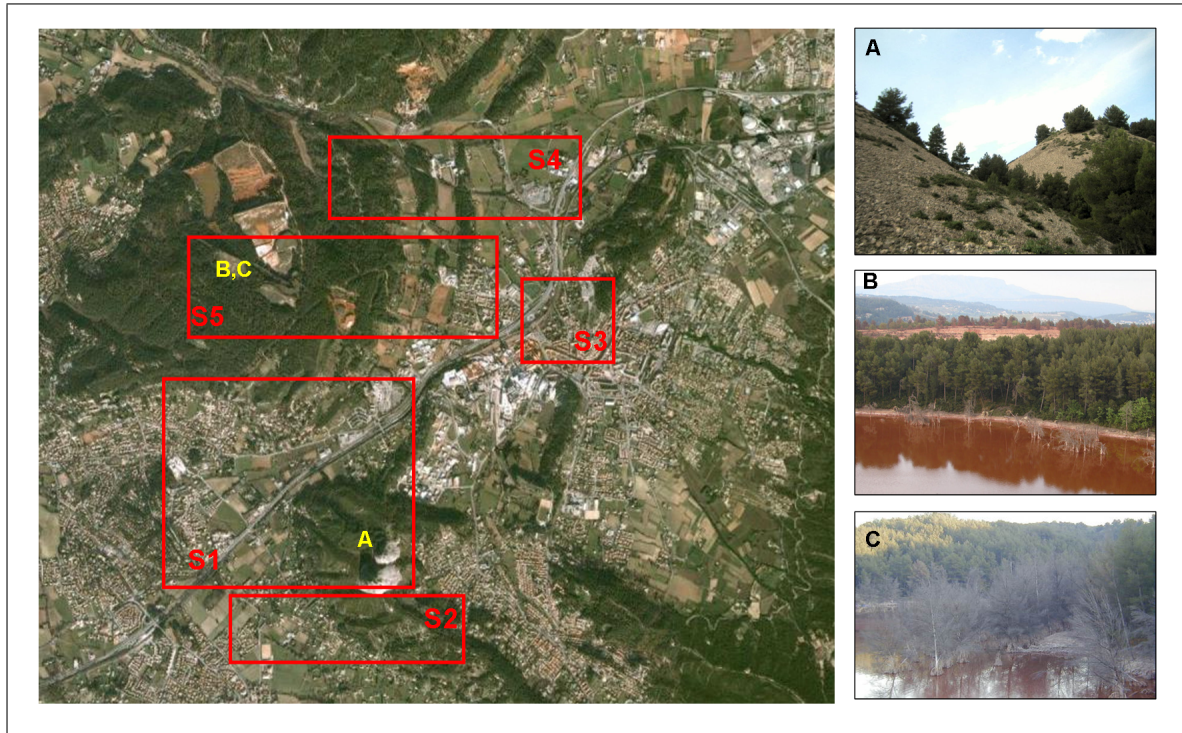
Figure 3.6: *Gardanne landscape. Red rectangles outline the different subsidence areas. A, B, and C are examples of landscape in non-urban areas (Taken from Google earth).*
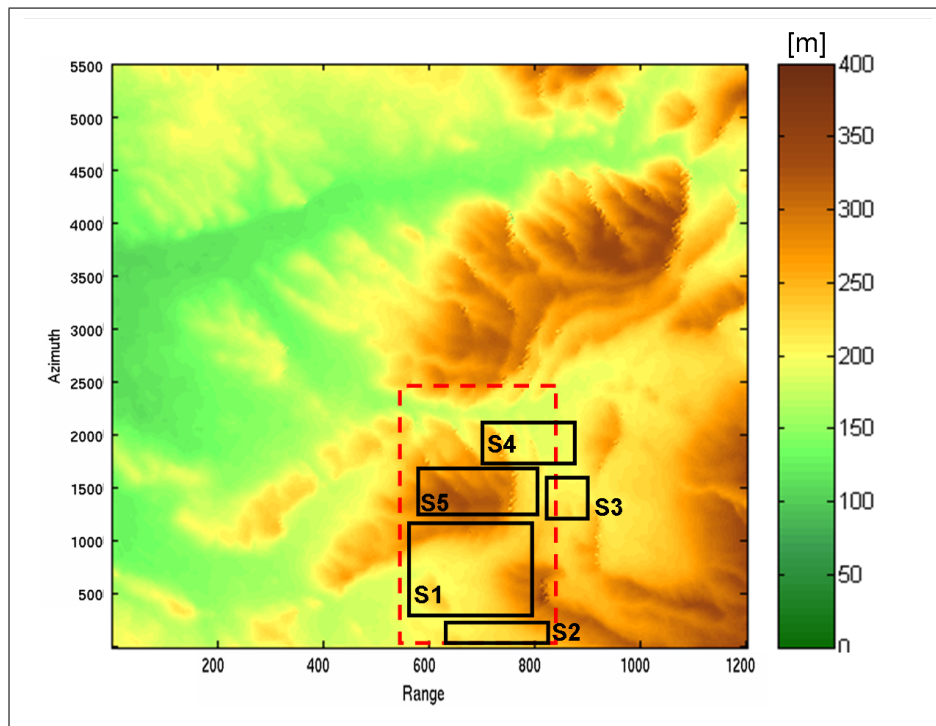
Figure 3.7: *Gardanne SRTM digital elevation model.*
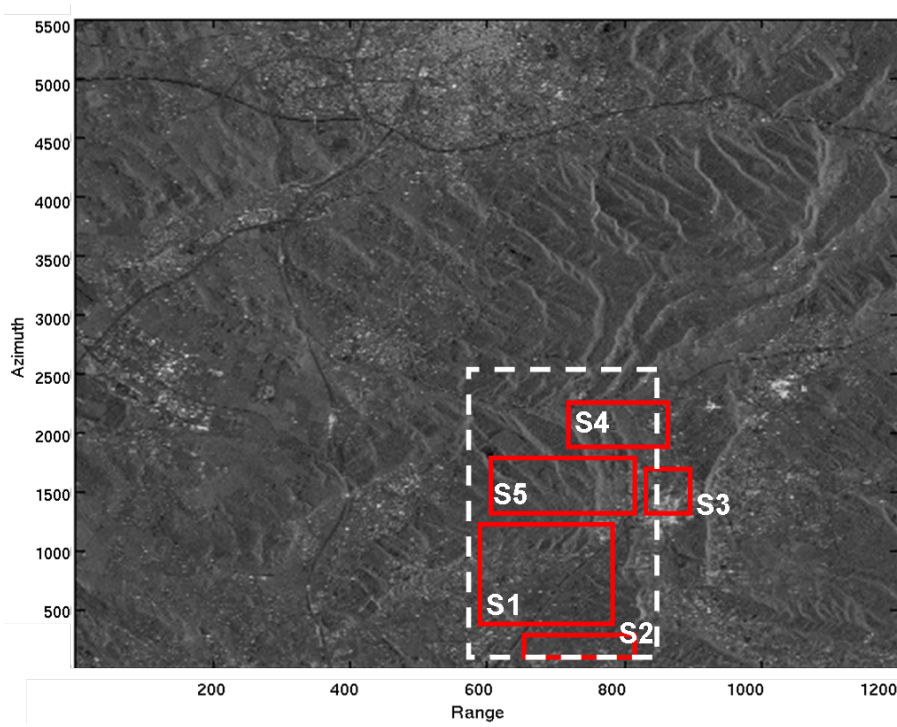
Figure 3.8: *The crop used in this study: the white rectangle is the whole deforming area in which all pixels are evaluated. Red rectangles are the five subsidence areas.*

3.2   General settings and remarks

The point of departure for this study is formed by the initial PSI results which we obtained using the standard PSI approach described in chapter 2. Before describing the results, some general settings are explained.

3.2.1   Initial settings

Dataset
Totally, there are 107 ERS1/2 images and 9 ENVISAT images available. All images are from the descending track. Because of the small amount of available ENVISAT data and also difficult application of cross-interferometry between ERS and ENVISAT data, we decided to use only ERS1/2 data. (See appendix A for a listing of the used images).

Interferogram formation
Interferograms are constructed using the Delft object-oriented radar interferometric software (Doris) (Kampes and Usai, 1999). The ERS2 image of 20th of March 1999 is used as the master image. The processing is limited to the small crop on the area of interest (i.e., blue rectangle in Fig. 3.1). As the difference in the Doppler centroid value of each SAR image affects the phase and therefore PSI results, it was decided to use only interferograms with the Doppler difference smaller than 500 Hz. This results in excluding 34 interfreograms due to the high Doppler difference. The topographic phase is subtracted from all interferograms using the SRTM digital elevation model. Hence, the PSI algorithm in this study estimates the residual height (or DEM error) of each PS, not the full topographic height. No filtering has been applied to the interferograms in order to preserve the original radar observations.
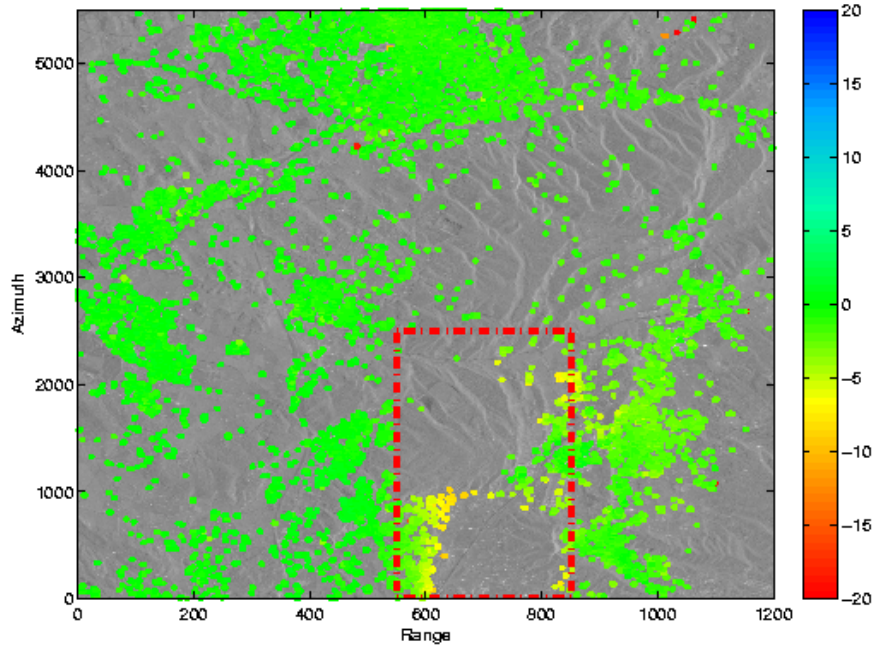
Figure 3.9: *Initial results: PS deformation rate. Red dash rectangle is the deforming area. The colorbar unit is [mm/y].*

After the interferogram formation step, in total 72 differential interferograms cropped on the area of interest are available. The crop contains 5500 and 1200 pixels in the azimuth and range directions respectively. The size of each pixel is 10 meter in range direction and 2 meter in azimuth direction. Note that the original pixel size of ERS SAR images is 20 by 4 meter. Due to oversampling of pixels with a factor two the size is reduced to 10 by 2 meter. Therefore the used crop covers about 11000x12000 square meter.

PSI processing/Preliminary estimation

First order PS candidates (PS1c) are selected using an amplitude dispersion threshold of 0.25, using a grid size of 300 m (see Section 2.2.2). In order to avoid amplitude variations due to sensor characteristics, empirical calibration (Ketelaar et al., 2005) is performed on amplitude images. During the first PSI analysis, it appeared that most of the selected PS1c are rejected in the preliminary estimation step. It appeared that using the amplitude of images with nominal instead of extracted replica pulse power can strongly influence the PS1c selection leading to selection of incoherent pixels and so rejection of most of them. In the data stack used in this study, there are five images processed with nominal replica pulse power. Using even one of these images for PS candidate selection can totally bias the results. Therefore, these images are excluded from the amplitude dispersion computations. Note that for PSI processing, the phases of these images are included.

The maximum length of the arcs in the initial network is restricted to 3 km. The arcs are temporally unwrapped using the integer bootstrapping method assuming linear deformation model. A covariance matrix is obtained using variance component estimation. Standard deviations of pseudo-observations are set to 40 m for residual heights, 0.01 m for master atmosphere, and 0.02 m for linear deformation. The reference point is set to the 1st order PS with the highest ensemble coherence. After spatial unwrapping, the unwrapping errors are removed using the spatial network, and the initial network is adopted (see Section 2.2.2). The atmosphere signal is filtered using the low pass filter with a triangle kernel of 3 year length.

Recall that this study only focuses on improvements in the densification step. Therefore, the preliminary estimation for all results presented in this study is the same and is based on the described settings.

PSI processing/Densification

The atmospheric phase screen (APS) of each interferogram is estimated using universal kriging. A Gaussian covariance function with a range of 3 km is used for kriging. The variance factor of the covariance function is estimated from the data.

For second order PS candidates (PS2c) selection, the crop is divided into two areas: 1) the deforming area (white rectangle in Fig. 3.8) and 2) the stable area (remaining parts). In the stable area, PS2c are selected using an amplitude dispersion threshold of 0.45. For the deforming area, it was decided to regard *all* pixels as PS2c.

Parameter estimation per PS2c is performed using the integer bootstrapping method. A covariance matrix is obtained using variance component estimation. For initial results, a linear deformation is assumed. The main reason not to choose the integer least squares method in this study is the time limitation.

The a-posteriori variance factor is used as a quality criterion for accepting PS. A threshold of 3 is used for final selection. Unwrapping errors are not removed in this step.

Also, sidelobes of strong point scatterers are not filtered out. As a result, a cluster of these points may appear around PS in the final results. Note that the estimated deformation of these points is homogeneous.

Post-processing

The main post processing step applied to the final results is removing the falsely accepted PS. These points are incoherent radar targets that show, by coincidence, a low variance and are detected as PS. We call them type-II errors. They are usually isolated points with extreme value of estimated deformation rate, and with large height difference. Type-II errors are removed in this study based on their estimated deformation rate, their estimated height difference and their ensemble coherence. Based on our a priori knowledge about the deformation field, the lower threshold for deformation rate is set to -30 mm/y. The upper bound threshold set to +1 mm/y as no uplift is expected in the area (Note that the reference point is located in the assumed stable area). The threshold for height difference is set to -/+50 meter. Finally, a lower bound threshold of 0.2 is used for ensemble coherence. Therefore, accepted PS with deformation rate outside the range -30 to 1 mm/y, absolute height difference larger than 50 m, and ensemble coherence smaller than 0.2 are assigned as type-II errors and excluded from the final results. Note that with these thresholds, some actual PS points are also removed as they have, for example, high subsidence rate due to unwrapping errors. So in this step not only incoherent points are removed but also some coherent PS are removed due to unwrapping errors.

3.2.2   Initial results

Using the standard PSI approach described in the Section 2.2.2 and the initial setting which is described in the previous section, we obtained the initial PSI results. This result is the starting point of this study. That is, all hypothesizes used for improvements are made by looking at this result and final improvements are compared with this result. The term "*initial results*" in this thesis refers to the results of this processing run.

Fig. 3.9a shows the detected PS and their displacement rates. The number of detected PS is 43786 in the whole crop and 2380 in the deforming area (red dash rectangle). As expected the PS are mainly located in urban areas. There are also some isolated PS in rural areas. The western side of the S1 subsidence area can easily be distinguished with average deformation rates up to 10 mm/y which is comparable to the leveling data (see Fig. 3.3). No PS is detected in the S2 and S5 areas. There is also a small amount of PS in the S3 area and on eastern side of the S4 area.
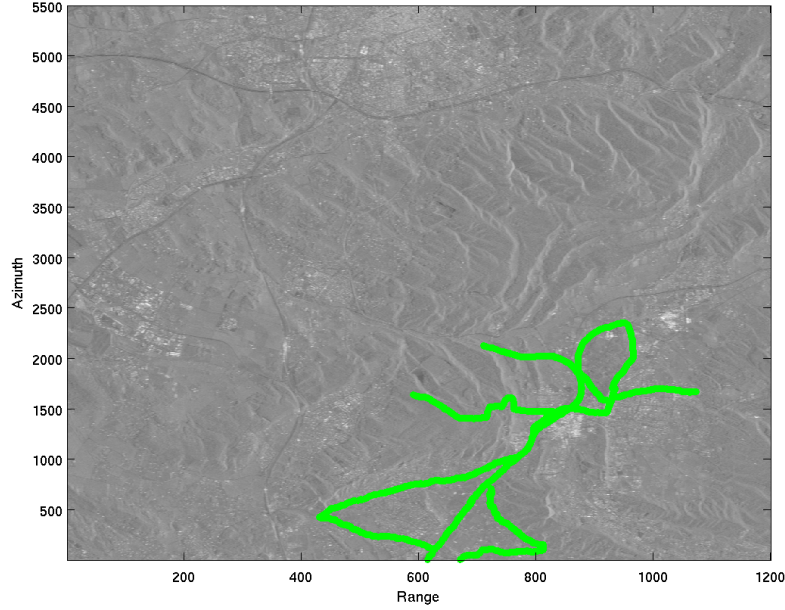
Figure 3.10: *Digitized leveling network (green points).*

3.3 Methodology for type-I error reduction

The first visual assessment of the initial results reveals the lack of PS in the main deforming areas. This lack of PS or limited number of PS in the area of interest raises the hypothesis of type-I errors. This section presents the generic methodology for refinement of these errors.

For analyzing of type-I errors, we need first to investigate the sources of them. Type-I error means that PS candidates are falsely rejected to be PS due to a large a-posteriori variance factor $\hat{\sigma}^2$ (see Eq. (2.5)) which is the criterion for accepting or rejecting a PS candidate. A large $\hat{\sigma}^2$ implies large deviation between observations and assumed mathematical model. The a-posteriori variance factor is an appropriate criterion assuming the hypothesis that the employed mathematical model (see Eqs. (2.7) and (2.9)) correctly models the relation between observations and unknown parameters and stochastic properties of observations. We call this hypothesis *the null hypothesis*. So testing $\hat{\sigma}^2$ is a general test (or overal model test(OMT)) of the validity of observations with respect to the null hypothesis. The false rejection of the null hypothesis or type-I error can be caused by one of these three factors: (Teunissen et al., 2005):

1. An inappropriate functional model which cannot capture the relation of the observations with the unknowns. That is, imperfection in the functional model which is formulated with the design matrix B and the unknown parameters (b vector), see Eq. (2.7).

2. A poor specification of the observables' noise characteristics in the stochastic model (matrix Q_y)

3. Errors in the observed data which are not covered by the null hypothesis. (i.e., unaccounted errors in the observation vector y.)

In this study, we hypothesize that the reason for type-I errors in PS selection is due to existence of some unaccounted factors (or phase contributions) and so imperfection in the mathematical model. We name these missing
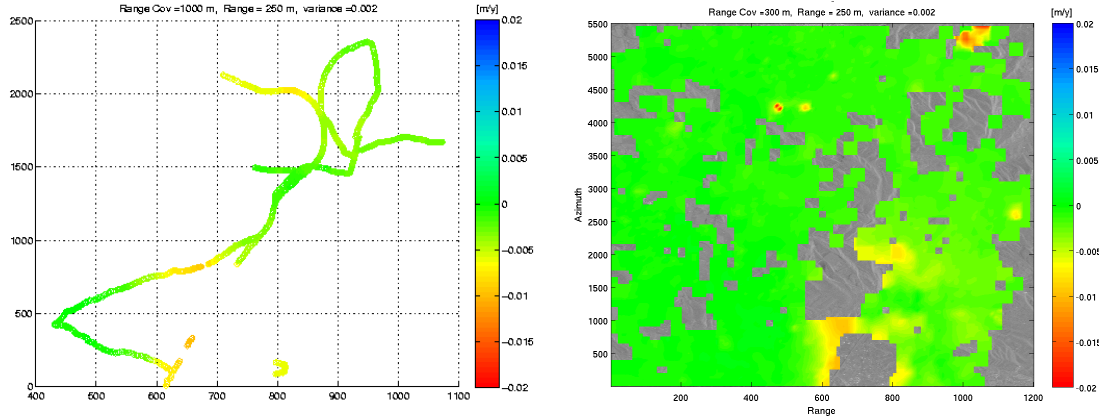
Figure 3.11: *Radar based velocity map of the initial results on a) the leveling profile location and b) the whole crop.*

factors *the alternative hypotheses*. The adaptation of the mathematical model for particular alternative hypothesis can be done in three general ways (based on three general causes of type-I errors):

1. **Adding the alternative hypothesis to the functional model:** This approach introduces a new unknown parameter (the missing factor) in the b vector of Eq. (2.7) and formulating its relation to the observations in the design matrix B. So, this approach requires appropriate knowledge about the missing factor in order to model it mathematically. Note that using an extended functional model with additional parameters leads to decreased rank of the estimation problem as the number of observations does not change.

2. **Adding the alternative hypothesis to the stochastic model:** It means considering the missing factor as noise and introducing its stochastic characteristics in the covariance matrix Q_y. This approach requires a-priori knowledge about stochastic properties of the missing factor. Note that adding additional parameters into Q_y leads to lower precision of the final estimated parameters.

3. **Removing or filtering the missing factor from the observations before parameter estimation:** This approach considers the missing factor as an error in the observations. The filtering can either be deterministic or stochastic. The deterministic approach requires detailed mathematical formulation of the missing factor in order to estimate it and subtract it from the observation vector y. The missing factor can also be filtered based on its temporal or spatial stochastic properties. The examples are different high/low pass filters in space or time domain. Note that unnecessarily filtering can introduce new errors in the model.

The adopted mathematical model is called the model under *the alternative hypothesis*. Note that unnecessary adaptation of the mathematical model with the approaches above can cause a decreased rank of the model and increase of the number of type-II errors, lower precision of the final estimated parameters, or inserting of new errors in the model. So each of these adaptations should only be applied when it is necessary. That is, we should have reasonable argument about the validity of the alternative hypothesis and invalidity of the null hypothesis in order to decide to use the adopted model.

In this research we investigate three possible sources of type-I errors as alternative hypothesis: atmospheric phase screen (APS) and orbital errors, non-linear deformation mechanism, and subpixel position of the scatterer. For each of them, a different methodology is applied based on one of the discussed adaptations. The details of these adaptations and results of improvements are presented in the next three chapters (Chapters 4, 5, and 6).

Item	Whole crop	Deforming crop	S1 area	S2 area	S3 area	S4 area	S5 area
Number of PS	43786	2380	521	9	688	62	26
Improvement (wrt initial results)	0 %	0 %	0 %	0 %	0 %	0 %	0
Number of type-II error	785	88	-	-	-	-	-
Mean of def. rate (mm/y)	-	-	-4.4	-5.7	-1.9	-5.1	-1.6
Max def. rate (mm/y)	-	-	-9.6	-7.7	-2.1	-7.7	-2.8

Table 3.3: Quantitative results of the Initial PSI results

3.4   Validation methodology

During the initiation of this project, we expected that we could get access to the numeric leveling data of the area in order to validation of our final results. However, the leveling data were not made accessible by the BRGM authorities or the associated parties. As a result, our validation strategy moved to a more qualitative (visual) approaches rather than quantitative. In general, three different approaches are applied in this study for validation of results and obtained improvements:

- **Validation based on the qualitative and visual information obtained from PSIC4 report:** The general approach is to produce descriptive data (e.g., diagrams, profiles, maps) and quantitative data (e.g., average deformation rate) which are comparable with the reference information presented in the PSIC4 report. For each processing run, the visual comparison of these produced validation data with reference data in the PSIC4 report can give us an impression of the final results quality.

- **Validation based on PSI results properties:** Besides validation data obtained from the PSIC4 report, the properties of each PSI result itself can be used for validation. Examples are the number of detected PS in different deforming areas, ensemble coherence of PS, number of type-II errors, and evaluation of deformation time series and unwrapping errors.

- **Validation based on other auxiliary data:** For some of the processing runs, we can obtained some auxiliary data from radar data by some independent processing. An example is *tandem pair interferograms* for validation of the applied approach for APS estimation (see Chapter 4).

As an example, the validation of the initial results is presented here.

Validation of the initial results In order to produce comparable results with leveling data, we digitized the location of the leveling network and tried to produce, for each processing run, a comparable velocity map (Fig. 3.3b) and similar spatio-temporal profiles (Figs. 3.5 and 3.4). Note that we did not have the exact position of the leveling benchmarks. We digitized the network using the amplitude radar image based on the assumption that the leveling network consists of lines along a railway line, canals, and roads. Fig. 3.10 shows the digitized network.

For producing the velocity map, a search radius of 250 m around each leveling point is used to identify nearby PS. The deformation rates of all nearby PS are used for interpolation of the deformation rate of the corresponding leveling point by kriging. An exponential covariance function with range of 1 km and variance factor of 4 mm/year is used. Fig. 3.11a shows the obtained velocity map for the initial results. The same colorbar as Fig. 3.3b is used in order to an able comparison. The first visual comparison shows that subsidence areas S1, S3 and, S4 are detected but underestimated (up to 10 mm/y), and the subsidence areas S2 and S5 are not detected at all. We also made an interpolated velocity map interpolated of the whole grid in the area for assessment and comparison of the whole deformation field. Fig. 3.11b shows this interpolated velocity map.

Fig. 3.12 shows the obtained AXE and SNCF spatio-temporal profiles on the digitized leveling network. Comparison of these profiles with Figs. 3.5 and 3.4 reveals that some parts of the S1 deformation is captured but

underestimated. The starting time of the deformation is also comparable. In the SNCF profile, S3 and S4 deformation areas are also captured. The general pattern of detected deformation is the same as for the leveling data but the magnitude of deformation is underestimated. Note the differences between colorbar of these profiles and leveling profiles.

Table 3.3 summarizes the quantitative results of the initial results. Comparison of deformation rates in this table with the Table 3.2 can also give us information about the validity of the results. For each processing run of this study this table is produced and compared with the initial results to evaluate the performance of each proposed algorithm.

Note that presenting all above information for all processing runs of this study results in tremendous amount of data with redundant information. This large amount of data can lead to a complicated and inefficient interpretation of the results. Therefore, in the next chapters for each processing run, only a limited part of this information is presented based on the requirements for validation and interpretation.
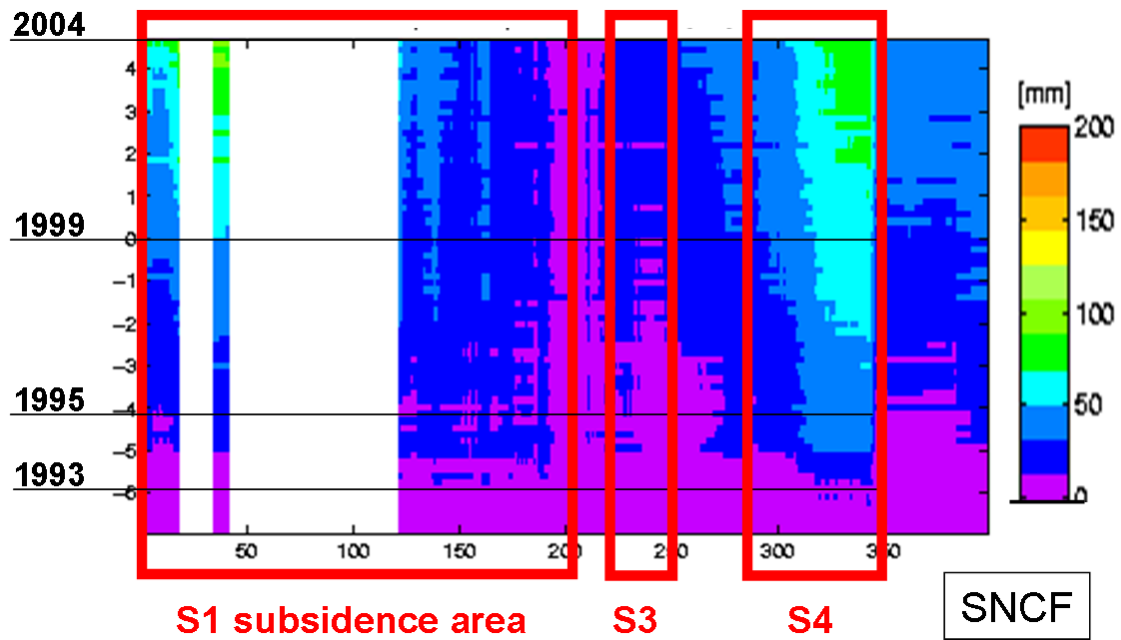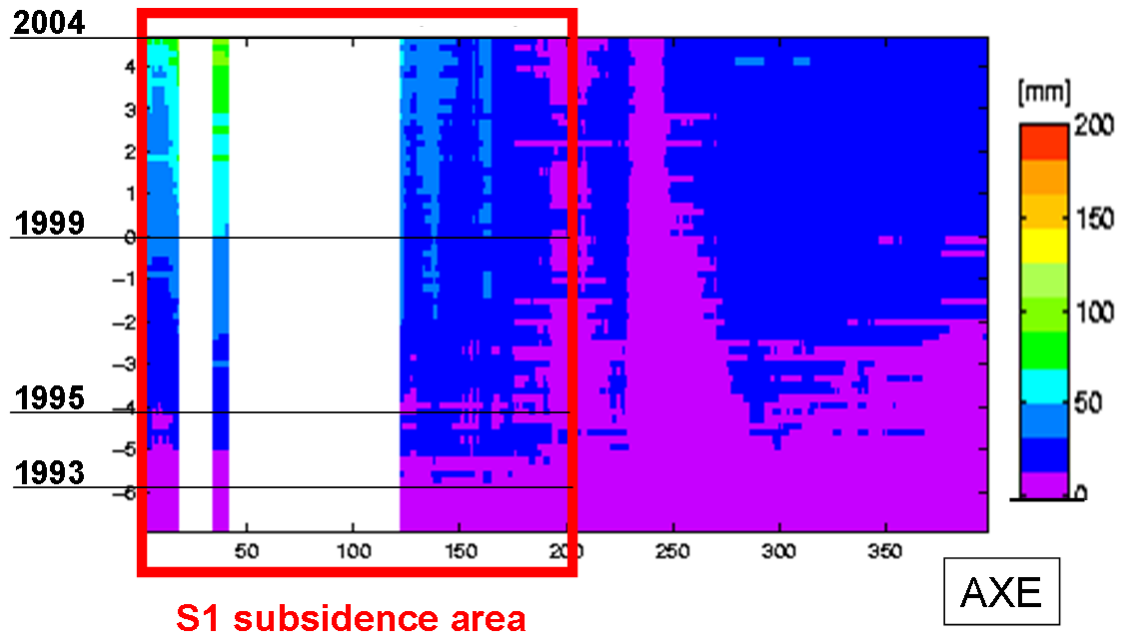
Figure 3.12: AXE and SNCF spatio-temporal profiles on the digitized leveling profile location.

Chapter 4

Atmospheric phase screen estimation

This chapter presents improvements in the estimation of the atmospheric phase screen (APS). The theory of different atmosphere contributions in the interferometric phase measurements is discussed. New methodologies for APS interpolation are presented, following by validation of each approach against tandem pair interferograms. The PSI results using these new approaches are presented, as well as the validation of the results.

4.1 Background

One of the main advantages of the PSI technique is its capability in mitigation of the atmosphere effect. In this way, the technique can achieve high precision (millimeter level) deformation measurements. So, the APS estimation is the key step in the PSI algorithm. In the standard PSI methodology, the atmospheric effect is isolated using spatial and temporal filtering on a coarse grid of 1st order PS per acquisition. This filtering is based on the correlation of the atmosphere in space and its decorrelation in time. The Kriging method is used for interpolation of the APS (see Section 2.2.2) using the covariance function which describes the APS spatial behavior. The idea of the study presented in this chapter is based on the hypothesis that this standard APS interpolation can not remove the APS sufficiently, so some part of the APS remains in the interferometric phase observations and is not accounted for in the mathematical model. This imperfection can cause PS to be falsely rejected, especially in areas with low signal to noise ratio [1] (e.g. non-urban areas with high non-linear deformation mechanism). So, the question is how we can improve PSI results, especially PS density, by better estimation of the APS. In the following section, we review the generic theory which describes different APS components. Based on this theoretical part, some shortcomings of the standard APS estimation approach are discussed, leading to our new APS estimation algorithm. The proposed approach is validated against tandem interferograms. Finally, the PSI results with the new approach are presented followed by a discussion of the results.

4.2 APS components

Errors due to the atmosphere signal in the interferometric phase is introduced by the two uncorrelated states of the atmosphere during the two SAR acquisitions. This signal may be divided into two contributions (Hanssen, 2001):

---

[1]Here the term signal to noise ratio implies the relation between the parameters of interest (e.g., deformation rate and height residual) and all other disturbing factors.

35
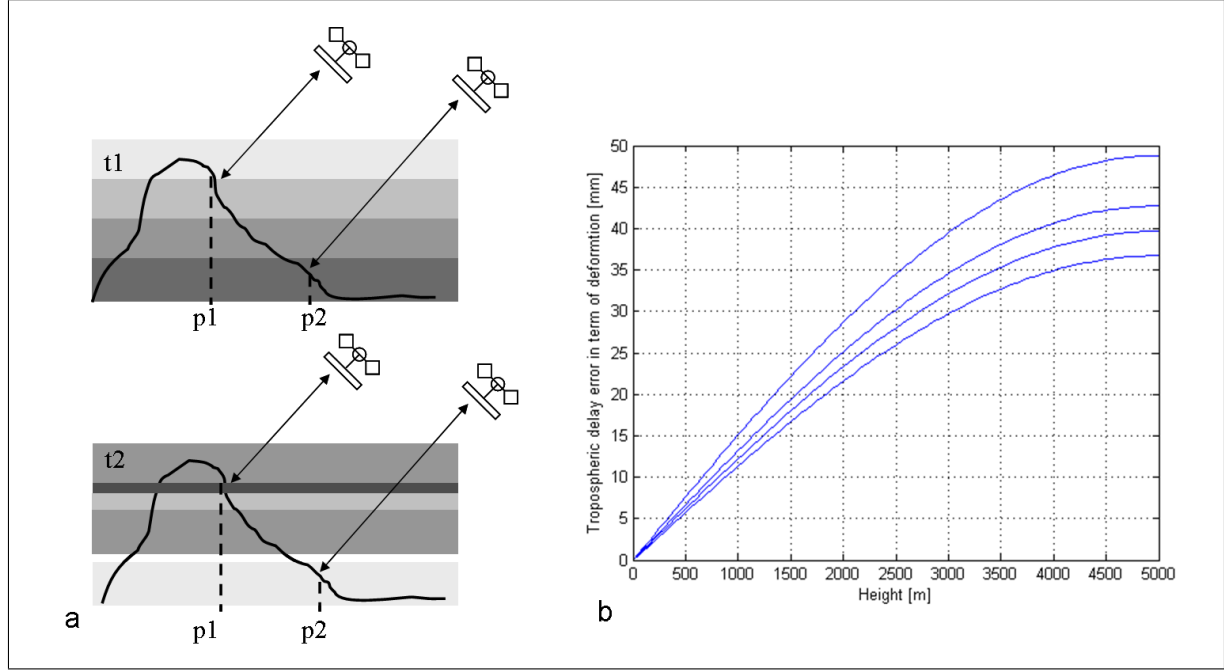
Figure 4.1: *Vertical stratification effect: a) Differential stratification delay between point p1 and p2 with different topographic height during the two SAR acquisitions at t1 and t2. Changes in gray values show the changes in vertical refractivity. b) The stratification delay error as a function of height for different time intervals (1, 35, 70, 140 days from bottom to up) converted to the corresponding amount of deformation.*

1. **Turbulent mixing:** This signal is caused by turbulent processes in the troposphere. Drivers of turbulent processes are solar heating of the earth's surface, difference in wind direction or velocity in different atmospheric layers. These processes are strongly nonlinear and behave on a wide range of scales. Based on Kolmogorove turbulence theory, Hanssen (2001) describes the behavior of the turbulence signal in radar interferograms using the power spectrum:

$$P_\varphi(f) = P_0(f/f_0)^{-\beta}, \qquad -8/3 \leq \beta \leq -2/3, \qquad (4.1)$$

where f is the spatial frequency, P_0 and f_0 are normalizing constants and β is the spectral index. Assuming second-order stationary and isotropy, the power spectra can be transformed to the covariance function $C(r)$ using the inverse DFT of the power spectra. Using $C(r)$, the covariance between two observations is a function of only distance between the observations. This covariance function can be used for simulation or interpolation of the turbulence signal. A typical range for fully developed (3D) turbulence between 2 to 5 km can be used. However, the variance factor (P_0) differs based on the weather condition, and needs to be estimated based on auxiliary data or from the observations.

2. **Vertical stratification :** This signal is the result of different vertical refractivity profiles during the two SAR acquisitions. For better understanding, assume that the full atmospheric column consists of infinite number of thin atmosphere layers, each with constant refractivity. For two different resolution cells with different elevation, the difference in the vertical refractivity profiles between two acquisitions introduces a new phase component in the interferometric phase, see Fig. 4.1a. Note that this effect will only affect pixels which have a different topographic height. For flat terrains, this effect can be neglected.

   Hanssen (2001) modeled the standard deviation of the interferometric phase due to the stratification effect with an empirical model as:

$$\sigma_\varphi = \frac{4\pi}{\lambda \cos \theta_{inc}} (33.7 + 0.08\Delta t) 10^{-3} \sin \frac{h\pi}{2h_s}, \qquad 1 \leq \Delta t \leq 182, \qquad 0 \leq h \leq h_s \qquad (4.2)$$
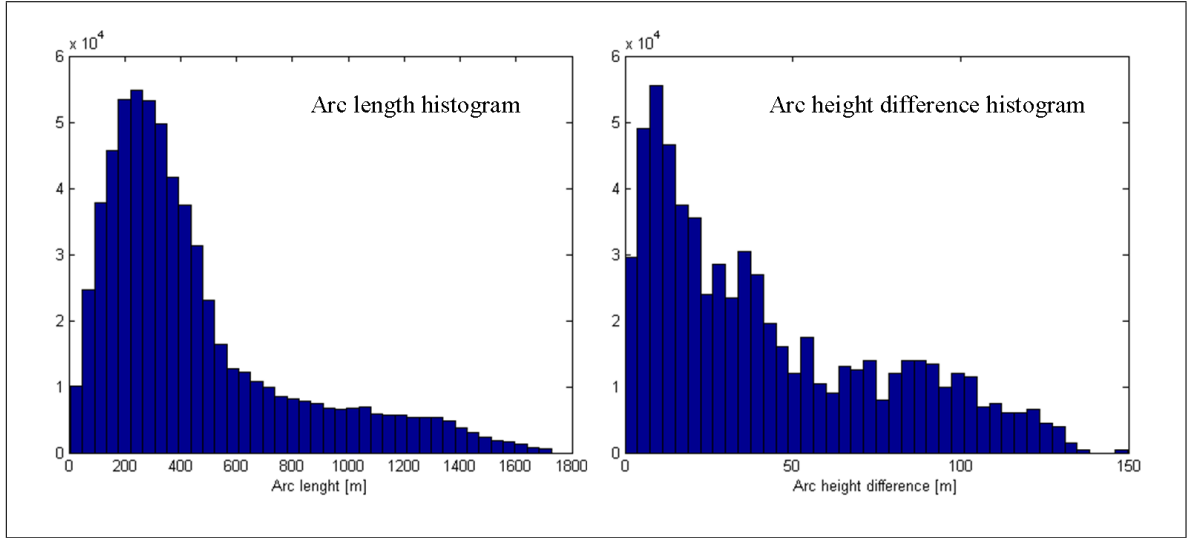
Figure 4.2: *Histogram of of the lengths and the height differences of all arcs used in the densification step in our case study on the Gardanne dataset. We can see that there are arcs with lengths of around* 1200 *m and a height difference of* 100 *m which can introduce a stratification error of* 3 *mm.*

where Δt is the time interval in days, h is height in meters, and $h_s = 5000m$ is a scale height. Above 5000 m the stratification signal can be neglected. Using this empirical model, we can derive the standard deviation of the stratification delay as a function of height for different time intervals (1, 35, 70, 140 days) converted to the corresponding amount of deformation (using C band radar $\lambda = 5.6cm$). Fig. 4.1b shows the relation of the stratification error as a function of the height difference. Note that the stratification signal is a function of a height difference which is dependent on the distance between two points.

Note on orbital error

It is important to consider that orbital errors cause a nearly linear trend over the interferogram. Due to potential similar spatial trends of the atmosphere signal, it is hard to distinguish the orbital errors from an atmosphere effect. Moreover, the residual phases, which are used in PSI processing as observation in order to estimate the APS, are also contains orbital errors. Therefore in the PSI processing, the APS signal may contain not only turbulence and stratification effects but also orbital errors.

4.3 APS interpolation

The standard approach for APS estimation using kriging, as described in Section 2.2.2, is based on following assumptions.

- The covariance function used for interpolation appropriately describes the spatial behavior of the APS components included in the filtered residual phases.

- The trend due to orbital errors can be also interpolated and estimated using the same covariance function (i.e. assuming the similar spatial behavior for the orbital trend and the atmosphere signal).

- Stratification signal is minimum because of using differential phases between neighboring pixels with short distance and so with likely small height differences.
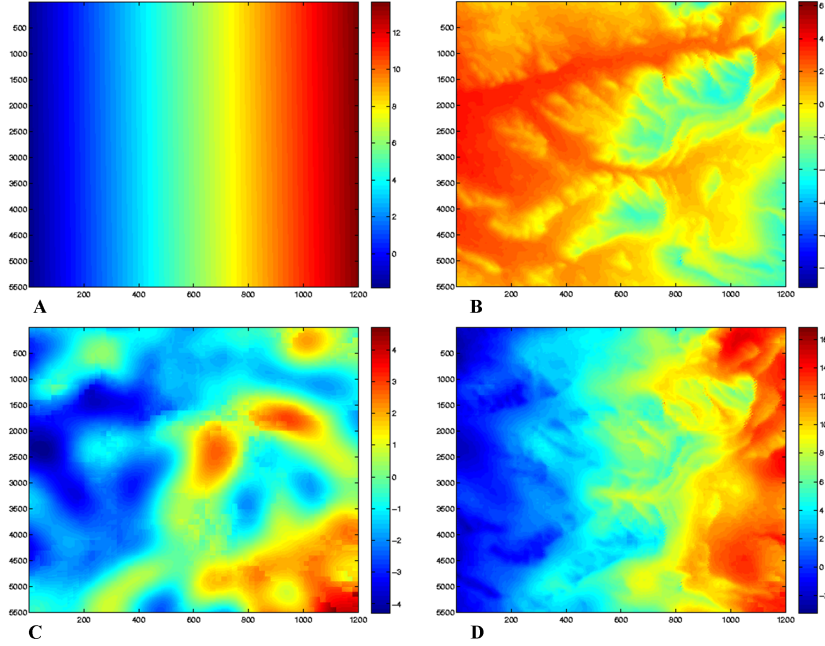
Figure 4.3: *Example of estimated APS by the proposed approach for an area of 12x11 km: A) estimated trend, B) Obtained stratification signal, C) Estimated turbulence by kriging, D)Final estimated APS. X and Y axis are range and azimuth in pixels(cover 12 and 11 km respectively). Colorbar shows the estimated phases in radians.*

The question is to what extend these assumptions are valid for APS interpolation. For example, the orbital trend may have a different spatial range than the turbulence signal. Does this difference affect the quality of the estimated APS and therefore the PS density? Moreover, the appearance of the trend in a data can invalidate the second-order stationarity condition for using the general covariance function in Kriging. Stratification also can affect the phase observations especially in the areas with a high topography variation. For example Fig. 4.2 shows the histogram of the lengths and the height differences of all arcs used in the densification step in the Gardanne test site based on the initial setting described in the Chapter 3. Note that there are arcs with lengths of around 1200 m and a height difference of 100 m which can introduce a stratification error of 3 mm. Could this error cause the false rejection of PS candidates? Can we improve the APS estimation by taking into account the effects of orbital errors and stratification and estimating these components independently? In order to answer these questions, we propose a new approach for the estimation of different parts of APS separately. Instead of only using a kriging interpolation on filtered residuals, we use three steps as follows (All these steps are applied after the preliminary estimation step in the PSI processing chain (described in Chapter 2)).

1. For each acquisition, we detrend the data by fitting a first order plane to the unwrapped phases of the 1st order PS and subtract the estimated trend from the original phase.

2. After estimation and subtraction of the trend, we estimate the vertical atmospheric stratification assuming a linear relation between topography (DEM) and stratification (Ferretti et al., 2005). For each 1st order PS (PS1) in the nth interferogram we can write:

$$\varphi_{unw}(i) = K_n H(i), \tag{4.3}$$

where $\varphi_{unw}(i)$ is a unwrapped and detrended filtered phase of ith PS1, $H(i)$ is the topographic height of the ith PS1 extracted from the DEM, and K_n is an unknown scaling factor for interferogram n. Note that the assumption of the linear relation between height and the stratification signal is valid for small height differences. We can see this linear behavior in the Fig. 4.1b for height differences smaller than $1500m$. Using
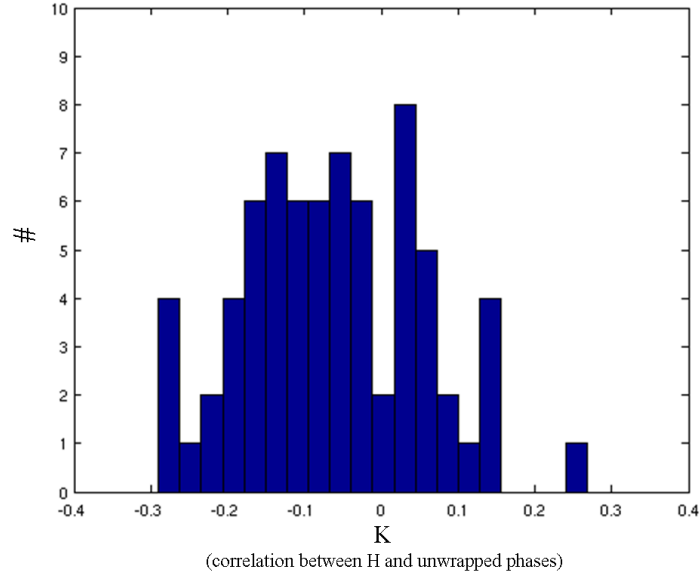
Figure 4.4: *Histogram of the estimated K values for the 72 interferograms of the Gardanne dataset. It shows that the estimated stratification effect is not significant.*

Eq. (4.3), the K factor for each interferogram is derived by least squares estimation using the detrended phase of the all 1st order PS (PS1) as observations. The topographic height $H(i)$ of each PS1 is extracted from the external DEM (e.g., SRTM DEM). Normalized values of φ_{unw} and H are used in the estimation. So the estimated K_n is the correlation coefficient between φ_{unw} and H. The total stratification effect is calculated by multiplying K_n with topographic height of each pixel. Then this signal is subtracted from the original detrended phase.

3. Finally we interpolate (using Kriging) the remaining phase residuals in order to derive the turbulence signal (as in the standard approach).

Consequently, the final estimated APS is a summation of a trend signal, stratification, and turbulence. As an example, Fig. 4.3 shows the obtained results for particular interferogram. In order to evaluate different APS estimation approaches, we performed three PSI processing runs with a varying APS estimation strategy: 1) Conventional approach (described in the chapter2), 2) APS estimation using detrending and turbulence estimation, and 3) APS estimation using detrending, turbulence estimation, and stratification estimation. We name these processing runs APS$_c$, APS$_{tt}$, and APS$_{tts}$ respectively. In the next section, we will verify the quality of these three approaches by comparison of the APS with tandem pair interferograms.

4.4 Validation against tandem pairs interferograms

Tandem pair interferograms are interferograms produced using ERS1/2 SAR images with a time interval of 24 hours from the same orbit. Due to the short temporal baseline, it is possible to assume that there is no deformation signal in the interferogram. The temporal decorrelation is also minimal for these interferograms due to the same reason. As the effect of topography is removed, the phase of differential tandem interferograms contains only the APS and can be used for validation of the estimated APS obtained from PSI processing.

For comparison of the results, we should consider that each estimated APS $\varphi_{n,0}^{APS}$ presents the difference between the atmospheric phase of the corresponding slave image ϕ_n^{APS} and the atmospheric phase of the master image
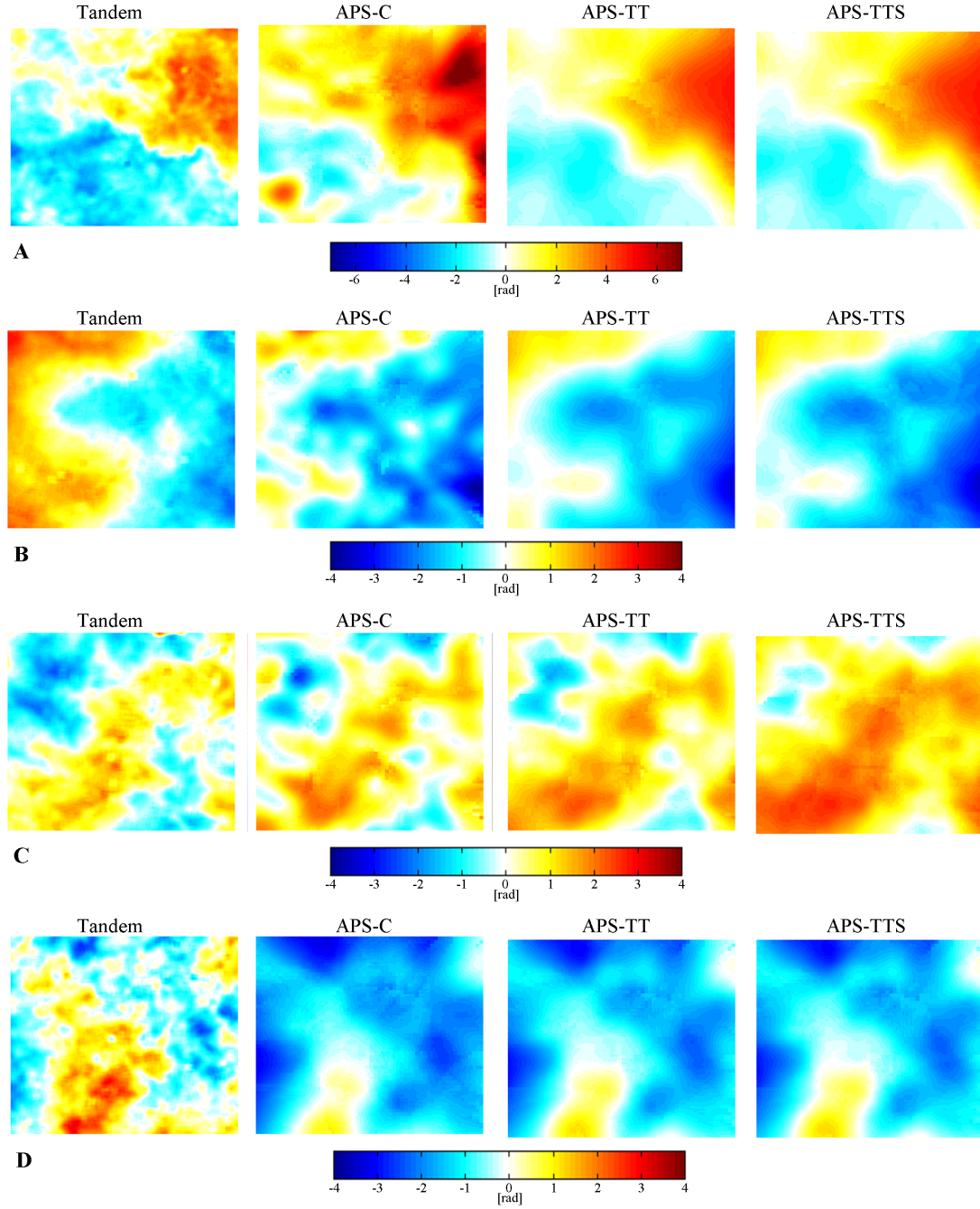
(a) First Part

Figure 4.5: *Six different tandem interferograms with corresponding estimated APS with different approach over the crop on the Gardanne test site (11000×12000 m). Note the different ranges in the color scales. (**A**) Jul 1999, (**B**) Mar 1999, (**C**) Mar 1996, (**D**) May 1996.*

(b) Second Part
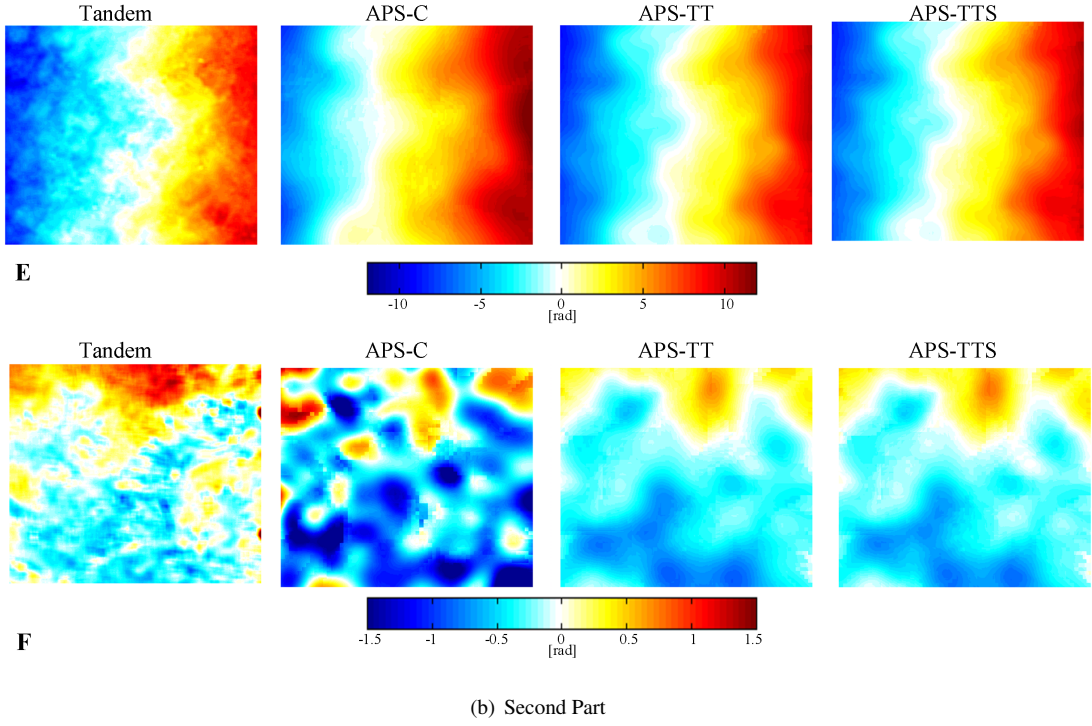
Figure 4.5: *–continued (**E**) May 1999, (**F**) Jan 2000.*

	A	B	C	D	E	F	Mean
rms of difference with APS$_C$[rad]	1.90	1.04	0.63	1.49	2.6	0.68	1.39
rms of difference with APS$_{TT}$[rad]	1.05	1.01	0.70	1.28	1.26	0.36	0.94
rms of difference with APS$_{TTS}$[rad]	1.04	1.05	0.90	1.20	1.31	0.32	0.97
Correlation with APS$_C$	0.86	0.88	0.81	0.84	0.98	0.54	0.82
Correlation with APS$_{TT}$	0.92	0.92	0.86	0.86	0.98	0.78	0.89
Correlation with APS$_{TTS}$	0.92	0.92	0.85	0.86	0.98	0.78	0.89
Estimated K	-0.08, -0.10	- (master) , -0.05	0.13, 0.14	0.31, 0.04	-0.15, 0.05	0.09, -0.03	-
Perpendicular Baseline [m]	65, -107	0, 40	-608, -713	660, 581	612, 548	-275, -126	-
Perpendicular Baseline of tandem [m]	-86.3	40.2	-105	-79.6	-63	152	-

Table 4.1: *Comparison of 6 tandem interferograms in Fig. 4.5 with APS$_C$, APS$_{TT}$, and APS$_{TTS}$ results. As the estimated APS signals are constructed from two estimated APS, there are two values of K and perpendicular baseline for each estimated APS.*

ϕ_0^{APS}. However, the tandem interferograms contains APS between two different slave images $\varphi_{m,n}^{\text{tandem}}$. In order to comparison, we should produce the estimated APS $\varphi_{m,n}^{\text{APS}}$ comparable with the tandem pair. We can write:

$$\varphi_{m,n}^{\text{APS}} = \phi_n^{\text{APS}} - \phi_m^{\text{APS}} = (\phi_n^{\text{APS}} - \phi_0^{\text{APS}}) - (\phi_m^{\text{APS}} - \phi_0^{\text{APS}}) = \varphi_{n,0}^{\text{APS}} - \varphi_{m,0}^{\text{APS}} \tag{4.4}$$

where index 0 corresponds to the master image. For evaluation, six tandem pairs in the Gardanne data stack are used. All tandem interferograms are resampled on the PSI master image grid and are relative to the same reference point. Fig. 4.5 shows an overview of these unwrapped tandem interferograms and the corresponding estimated

(a) APS$_C$
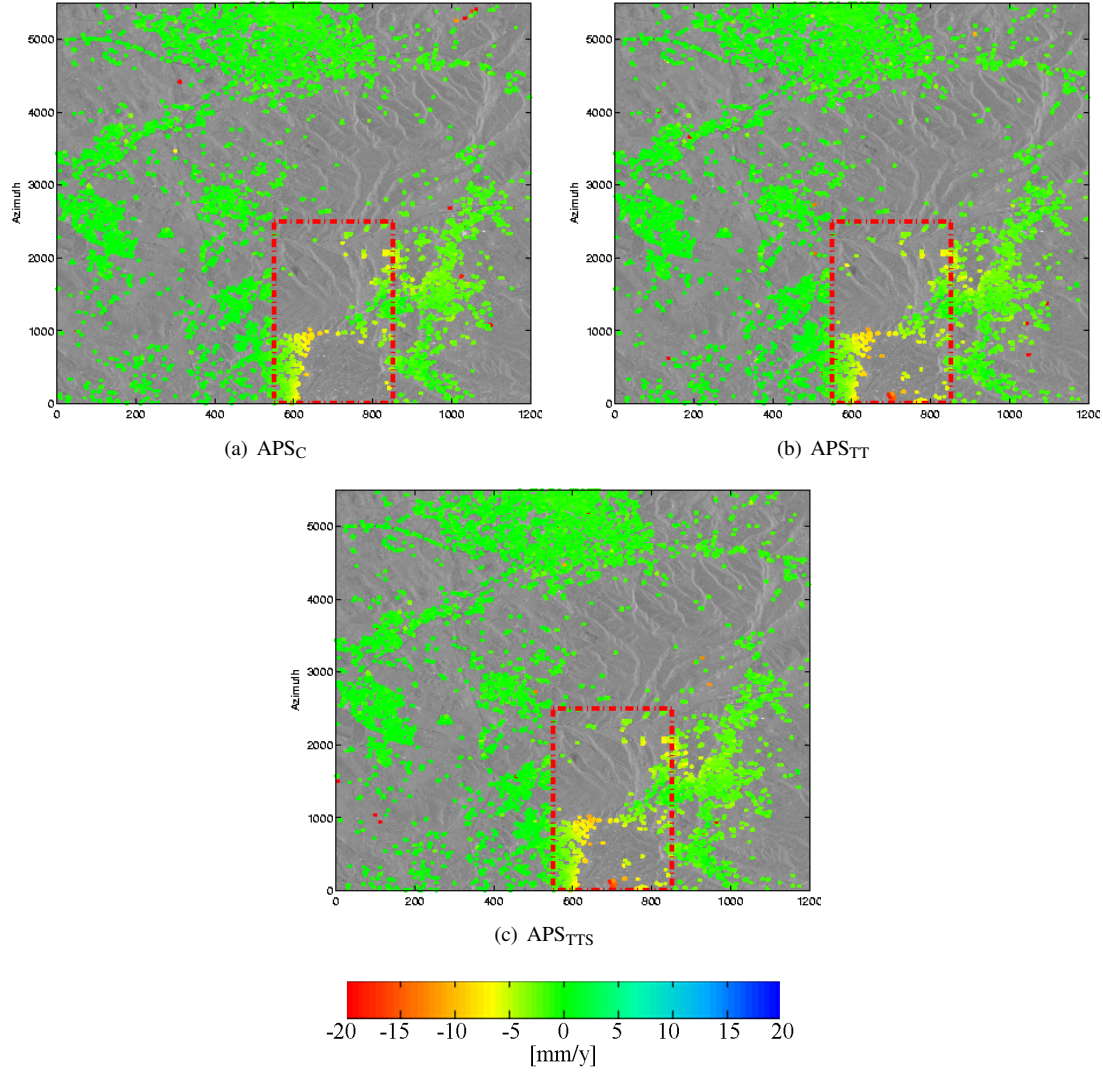
(b) APS$_{TT}$

(c) APS$_{TTS}$

Figure 4.6: *PSI results for different processing runs: (a) APS$_C$ ($\#PS = 2380$), (b) APS$_{TT}$ ($\#PS = 3205$), and (c) APS$_{TTS}$ ($\#PS = 3298$). Linear deformation rates estimated from the unwrapped time series are shown. Red dashed box is the deforming area.*

APS$_c$, APS$_{TT}$, and APS$_{TTS}$. Table 4.1 summarizes the results of the comparison.

A first visual assessment of the plots suggests that the results obtained from the new approaches (APS$_{TT}$ and APS$_{TTS}$) have better fit to the tandem interferograms than the conventional method (APS$_C$). Also we can see the difference between the APS$_{TT}$ and APS$_{TTS}$ results is very small, suggesting that the estimated stratification signal is not significant. We can see in the Table 4.1 that the APS$_{TT}$ and APS$_{TTS}$ results have approximately comparable quality in term of the rms value of the differences with tandem pairs. The new approach results in approximately 0.45 radians improvement in the rms values, comparable to the 2 mm deformation signal. Moreover, in terms of correlation with the tandem interferograms, the APS$_{TT}$ and APS$_{TTS}$ method show the comparable results and present the significant improvement with respect to the conventional approach.

The histogram of the estimated K values (Fig. 4.4) also confirms that the estimated stratification effect is not significant. Note that K values show the correlation between the unwrapped phases of the PS1 and their extracted height from the DEM. The potential reasons for this insignificant signal can be summarized as:
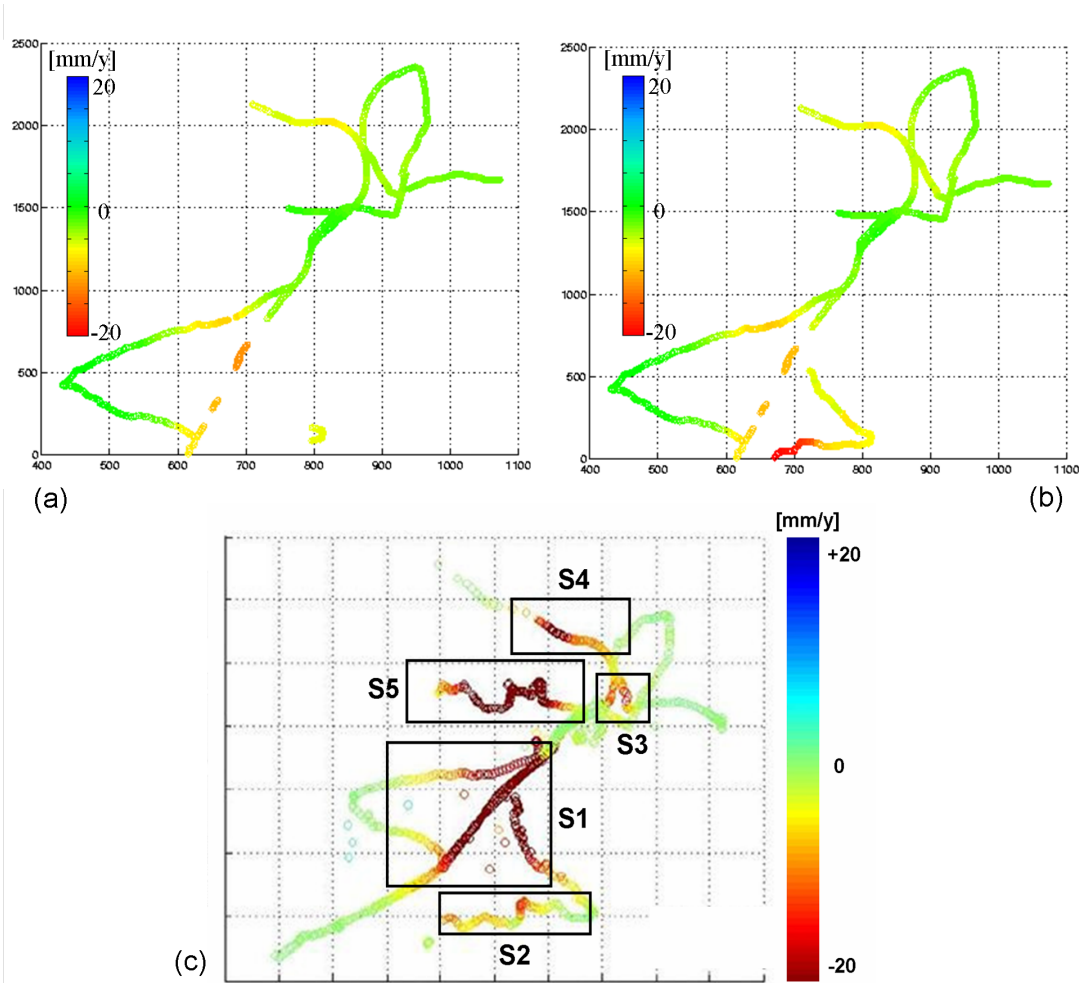
Figure 4.7: *Interpolated velocity map on the leveling profile location for PSI results obtained by: a)APS$_C$ method, and b)APS$_{TT}$ method. c) the annual cumulative deformation obtained from the leveling data((Racoules et al., 2006)), and the location of the five subsidence areas.*

1. The stratification signal may be not significant in the dataset. Note that also the double difference measurements between nearby PS candidates will reduce the stratification signal.

2. The level of details of the used DEM for stratification estimation is very low. We used the SRTM DEM which has 30 m horizontal resolution with about 5 m standard deviation in height. This DEM also is very smooth, so the nearby pixels have approximately the comparable heights. Using this DEM for the stratification estimation may not capture the small height variation between nearby PS1. So it can only estimate the large scale stratification signal.

3. The vertical stratification signal has a seasonal behavior (Hanssen, 2001) and so correlation in the time domain. As the APS estimation step is applied after the temporal filtering of the unwrapped phase measurements, some part of the stratification signal can leak to the temporally correlated signal (i.e., unmodeled deformation). Therefore, the filtered phases which are used as observation for estimation the stratification signal may not contains the full stratification effect.

4. The low signal to noise ratio of the stratification signal: the unwrapped phases which are used for the stratification estimation includes the APS effect and also the noise. If the amount of noise is very higher than the stratification effect, the proposed method may not capture this signal due to its low signal to noise ratio.

4.5 PSI results

We performed three PS processing runs with the same settings but different approaches for APS estimation. Fig. 4.6a, b, and c show the results using APS_C, APS_{TT}, APS_{TTS} methods. The number of detected PS in the whole crop is 2915, 31680, and 32262 respectively. These results also confirm that the improvement in the APS estimation, and show comparable results for APS_{TT}, APS_{TTS} methods. The number of PS in the deforming areas is improved from 2380 using the conventional approach to 3205 and 3298 for APS_{TT}, APS_{TTS} methods, that is 35% and 39% improvement in the PS density respectively. The newly detected PS by the proposed approach improve the captured deformation signal of the area. Fig. 4.7 shows the interpolated velocities on the leveling profile for the conventional approach and APS_{TTS} with comparison of the leveling data. The main improvement is for the S2 subsidence area and the east part of the S1 subsidence area. In the S3 area and in the center of the S1 area, also the improved results shows the better estimation of the deformation signal. In the S3 area, the number of PS increased from 688 to 788, leading to improvement of the maximum deformation rate from -2.1 mm/y to -5.8 mm/y.

4.6 Conclusions

The main conclusion of the study is that the new APS estimation approach including trend and turbulence estimation (APS_{TT}) performs better in terms of rms and correlation than the conventional approach. The tandem pair validation confirms this conclusion. We derived the rms of differences between estimated APS and the tandem interferograms. The average of these rms values was improved from 1.39 radians using the conventional approach to 0.94 radians by APS_{TT} method. This is comparable with 2 mm improvement in term of deformation. The mean rms value of 0.94 radians (4 mm deformation) can be interpreted as the precision of our APS estimation using the initial setting which was described in Chapter 3.

The results of the stratification estimation shows that the estimated signal is not significant. The main reasons for that may be the low signal to noise ratio of this signal in comparison with the noise level and the low resolution of the used DEM for the estimation.

Application of the proposed optimizations in the APS estimation shows 39% increase in the number of detected PS in the deforming area, leading to better estimation of the deformation field. This improvement also confirm the better APS estimation by the proposed approach.

Chapter 5

Subpixel position of persistent scatterers

This chapter focuses on the influence of the subpixel position of persistent scatterers on their detection. The mathematical formulation of this effect is presented. A new method for detection of pixels with a large subpixel position is given, followed by different methods to account for this effect in the PSI methodology. Finally, the improved PSI results using the new methodologies are presented, followed by validation of and discussion about the obtained results.

The subpixel position of PS can induce an additional phase component in the interferometric phase of the corresponding pixels. The hypothesis which initiated the study of this chapter is that neglecting this effect in the PSI estimation can results in an imperfection in the PSI mathematical model, leading to a false rejection of PS (i.e., type-I errors). Some studies (e.g., Kampes (2005)) proposed to estimate this effect as a new unknown in the PSI estimation and deal with it functionally, while some others (e.g., Hooper (2006)) suggest to treat this effect as a noise term and deal with it stochastically. In this chapter, we investigate this source of type-I errors and present different functional and stochastic approaches to cope with it. It is studied how we can detect pixels with a subpixel position and how the estimation approach can be optimized to deal with this effect in order to improve the PS density.

5.1   Theory

One of the steps in the interferogram formation is computing and correcting the interferometric phase due to the curvature of the earth surface, the so-called reference phase. This step involves correcting for the phase of each pixel as if the scattering surface were lying on a reference ellipsoid. The reference phase is operationally calculated at the leading edge of a pixel (i.e., the upper left corner of a pixel) and not at the exact location of the phase center of the scatterer, leading to an uncompensated reference phase for point scatterers. Fig. 5.1 shows the geometry for this term in the azimuth and range directions. Note that this term only exists for pixels with a dominant point scatterer, since for pixels with distributed scatterers the effective phase center is approximately at the center and equal for all pixels (Kampes, 2005). Fig. 5.1 shows also that the phase difference due to a scatterer subpixel position is originated from the difference between looking angles (θ_x^m and θ_x^k) or squint angles (ϑ^m and ϑ^k) between two acquisitions. In the case of equal looking angles or equal squint angles (i.e., zero baseline), the corresponding uncompensated reference phase for both acquisition are the same and cancel out. In the following paragraphs, we explain the mathematical derivation of the phase component caused by a subpixel position of the scatterer in the azimuth and range directions.

Subpixel position in the azimuth direction: From Fig. 5.1(**A**), the additional range to the actual phase center
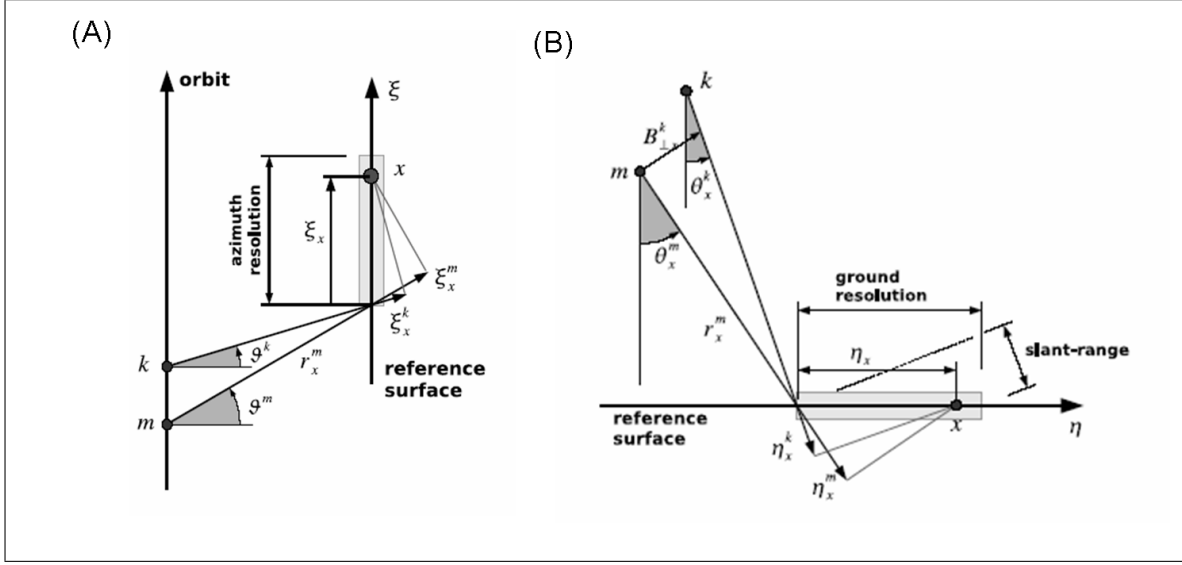
Figure 5.1: *Geometry for a point scatterer located at the subpixel position in (**A**) Azimuth and (**B**) Range directions (Marinkovic et al., 2008).*

with respect to its leading edge in the azimuth direction can be written as:

$$\xi_x^k = \xi_x \sin \vartheta^k. \tag{5.1}$$

The squint angle ϑ can be related to the Doppler centroid frequency f_{DC}^k by (Bamler and Just, 1993):

$$f_{x,DC}^k \approx \frac{-2v}{\lambda} \sin \vartheta^k, \tag{5.2}$$

where v is the local satellite velocity and λ is the radar wavelength. From Eqs. (5.1) and (5.2), we can write the additional range as:

$$\xi_x^k = \frac{\lambda}{-2v} f_{x,DC}^k \cdot \xi_x. \tag{5.3}$$

The additional range ξ_x^k in Eq. (5.3) is equivalent of the additional phase of:

$$\phi_{\xi_x}^k = \frac{2\pi}{v} f_{x,DC}^k \cdot \xi_x. \tag{5.4}$$

Note that this additional phase is independent of the wavelength assuming the same sensor for both acquisitions. Finally, assuming equal sensor velocity v, the interferometric phase due to the azimuth subpixel position of the point scatterer can be derived as:
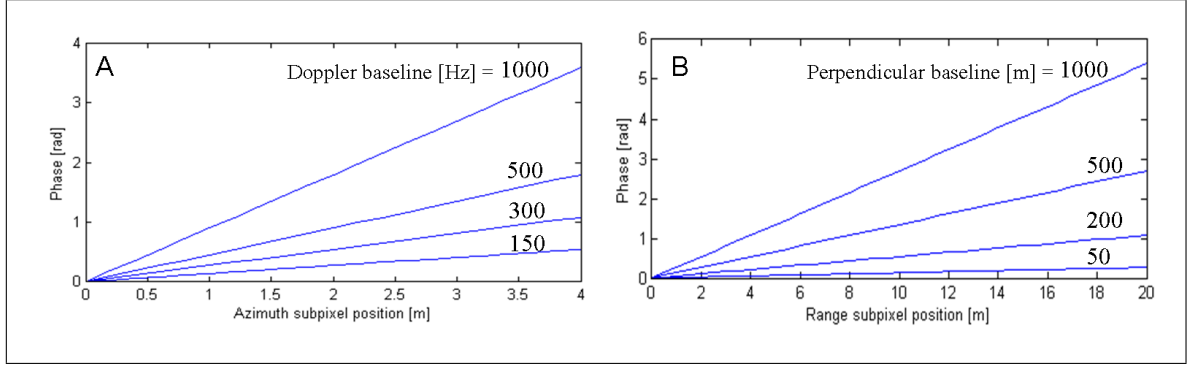
Figure 5.2: *Sensitivity of the differential interferometric phase to* **(A)** *azimuthal and* **(B)** *range subpixel position for different values of the Doppler baseline and perpendicular baseline, assuming equal wavelength and satellite velocity for master and slave. Typical ERS parameters were used: 750 km satellite altitude, 21 degree look angle, 5.6 cm wavelength, 4 m azimuth resolution, and 20 m ground-range resolution.*

$$\phi_{\xi_x}^{k,m} = \frac{2\pi}{v}(f_{x,DC}^m - f_{x,DC}^k) \cdot \xi_x. \tag{5.5}$$

Fig. 5.2(**A**) shows the sensitivity of the interferometric phase to a azimuthal subpixel position for different Doppler baselines.

Subpixel position in the range direction: From the geometry for a point scatterer with subpixel position in range (Fig. 5.1(**B**)), the additional range to the actual phase center with respect to its leading edge in the range direction can be written as:

$$\eta_x^k = \eta_x \sin \theta_x^k, \tag{5.6}$$

where η_x^k is the ground range position of the scatterer. The equivalent phase of η_x^k is:

$$\phi_{\eta_x}^k = \frac{-4\pi}{\lambda} \eta_x \sin \theta_x^k. \tag{5.7}$$

Therefore, assuming the same wavelength for both acquisitions, the interferometric phase for a point scatterer with subpixel position in the range direction can be written as:

$$\phi_{\eta_x}^{k,m} = \frac{-4\pi}{\lambda}(\sin \theta_x^m - \sin \theta_x^k) \cdot \eta_x. \tag{5.8}$$

Substituting the approximation of $\theta_x^m - \theta_x^k \approx B_\perp/r_x^m$ in Eq. (5.8) results in:

$$\phi_{\eta_x}^{k,m} = \frac{-4\pi}{\lambda}(\sin \theta_x^m - \sin(\theta_x^m + \frac{B_\perp}{r_x^m})) \cdot \eta_x. \tag{5.9}$$

Using the rule for *Sine* of sum of two angles, it follows that:
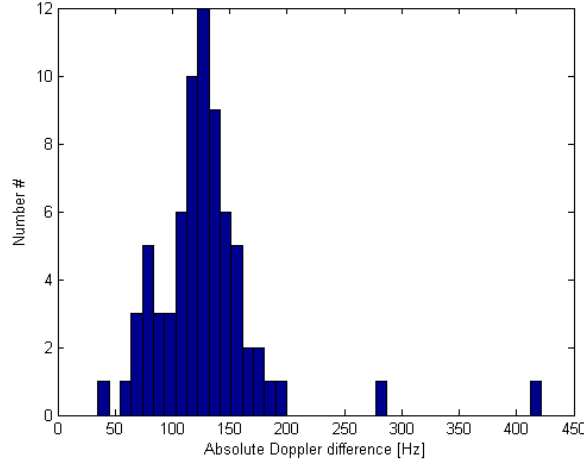
Figure 5.3: *Histogram of Doppler baselines on the Gardanne dataset. Note the small variability of Doppler baselines in this dataset.*

$$\phi_{\eta_x}^{k,m} = \frac{-4\pi}{\lambda}\left(\sin\theta_x^m - \left(\sin\theta_x^m\cos\left(\frac{B_\perp}{r_x^m}\right) - \cos\theta_x^m\sin\left(\frac{B_\perp}{r_x^m}\right)\right)\right) \cdot \eta_x. \tag{5.10}$$

Typically $B_\perp^k << r_x^m$ so this can be simplified to:

$$\phi_{\eta_x}^{k,m} = \frac{4\pi}{\lambda}\frac{B_\perp}{r_x^m}\cos\theta_x^m \cdot \eta_x. \tag{5.11}$$

Using Eq. (5.11), we computed the sensitivity of interferometric phases to a range subpixel position for different perpendicular baselines. Fig. 5.2(**B**) shows this sensitivity. The phase induced by a range subpixel position $\phi_{\eta_x}^{k,m}$ and the phase due to a residual height (see Eq. (2.2)) are both linear functions of the perpendicular baseline $B_\perp$, so they are indistinguishable from each other and cannot be estimated separately. Therefore, the range subpixel position is estimated together with a residual height ΔH. Consequently, a range subpixel shift of the scatterer will introduce an error in the estimated scatterer height and therefore in its geolocalization. Note that in the case that sensors with different frequencies are used (i.e., cross interferometry), the range subpixel position should be accounted for and it could be estimated separately from a residual height (see Kampes (2005); Adam et al. (2004)). So, in this study, we focus only on the influence of azimuthal subpixel position.

5.2   Methodology

The azimuthal subpixel position of PS induces an additional phase component in the PSI observations (Eq. (5.5)), especially when there is a large difference between the Doppler centroid frequency of the master and slave images. Fig. 5.3 shows the histogram of Doppler baselines in our dataset. We can see that the variation of Doppler differences is small in our dataset. Doppler baselines are generally small (around 100-150 Hz) which can induce the phase error around 0.5 radian (for subpixel position larger than 3 m). There are only two images with a Doppler baseline larger than 250 Hz which can induce a phase error of 1.0-1.5 radian, equivalent to 4-6 mm deformation. The hypothesis is that neglecting this additional phase in the mathematical model causes an imperfection in the model and so can produce type-I errors. In this section, we present three methods to deal with this term based on the general methodology described in Section 3.3.
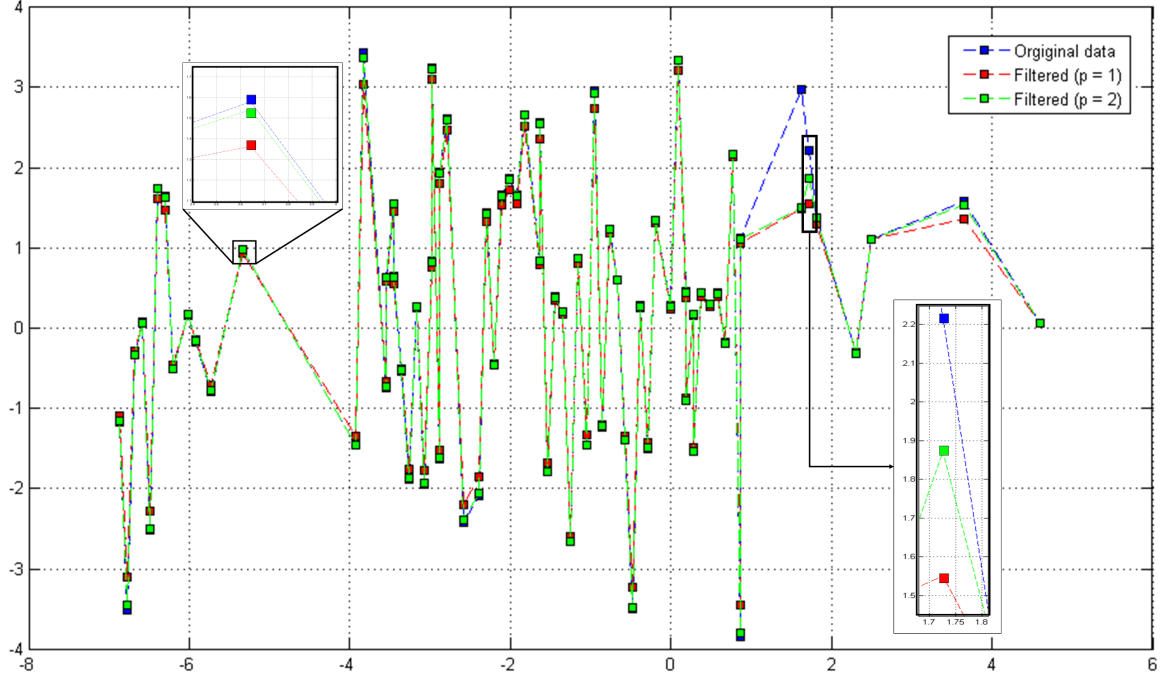
Figure 5.4: *Example of azimuthal subpixel position filtering on a particular PS. Horizontal axis shows time in year and vertical axis shows phase values in Radians.*
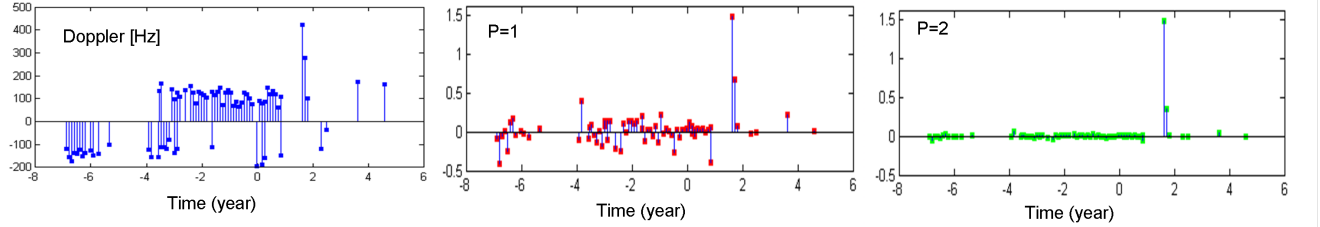
Figure 5.5: *Dependency of filtered phases to Doppler baselines: Left) Time series of Doppler baselines, Middle) Time series of the filtered phase with $p = 1$, and Right) Time series of the filtered phase with $p = 2$.*

Method1 : Estimation of a azimuthal subpixel position as an additional unknown parameter

The azimuthal sub-pixel position can be estimated as an additional parameter in the functional model based on the linear relationship with the Doppler difference between the master and slave image, Eq. (5.5). In the case of high Doppler variability among interferograms, it is feasible to estimate the azimuthal subpixel position with appropriate precision. However, in the case of small variation of the Doppler frequencies (e.g., in our dataset), azimuthal sub-pixel position cannot be estimated with high precision. Note that adding this additional unknown parameter to the functional model leads to a decreased rank of the estimation problem and so increase in the number of type-II errors.

Method2 : Adding the effect of azimuthal subpixel position to the stochastic model

In this method we treat the azimuthal subpixel position stochastically rather than functionally. That is instead of estimating this parameter as a new unknown, we introduce it in the stochastic model. Assuming certain standard deviation for a azimuthal subpixel position (e.g., $\sigma_\xi = 2$m), we computed the corresponding phase standard deviation $\sigma_{\phi,\xi}^n$ in each interferogram using Eq. (5.5). These standard deviations are added to the already constructed covariance matrix Q_ψ (see Eq. (2.13)). So the adopted covariance matrix is:
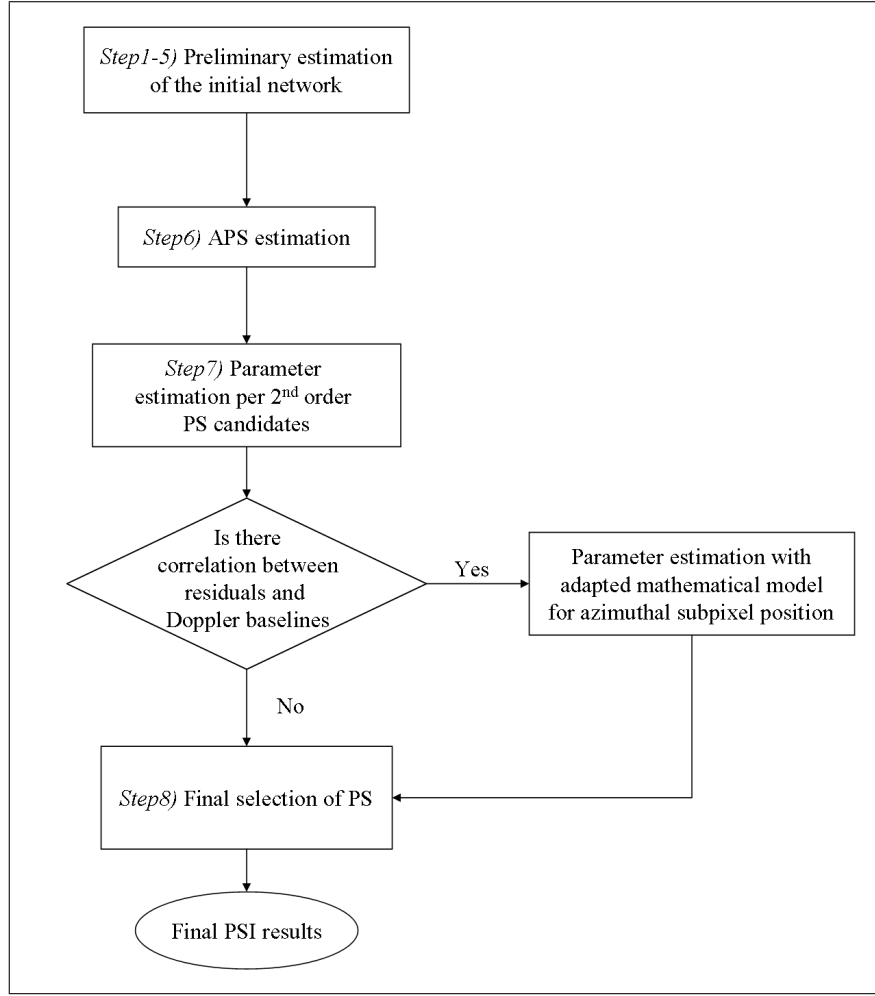
Figure 5.6: *Flow diagram of the proposed method for detection of PS with azimuthal subpixel position and adaptation of the mathematical model.*

$$Q_\psi^{adopted} = Q_\psi + (\frac{2\pi}{v}.\sigma_\xi)^2. \begin{bmatrix} (\Delta f_{dc}^{01})^2 & & & \\ & (\Delta f_{dc}^{02})^2 & & \\ & & \ddots & \\ & & & (\Delta f_{dc}^{0n})^2 \end{bmatrix} \qquad (5.12)$$

where f_{dc}^{0n} is the Doppler baseline of the nth interferogram. Using this adopted covariance matrix, observations with higher Doppler difference have higher variance and so lower weight in the estimation, leading to smaller a-posteriori variance factor $\hat{\sigma}^2$ and so acceptance of the PS. Note that this adopted covariance matrix should only be used for dominant point scatterers with large subpixel position. Adding this term to the stochastic model for all pixels results in underestimation of $\hat{\sigma}^2$, leading to the false detection of PS (i.e., type-II errors).

Method3 : Filtering the effect of azimuthal subpixel position from observations
In this approach, we tried to remove the influence of the azimuthal subpixel position from the observation vector y. This filtering is performed after estimation of fixed ambiguities $\breve{a}$ (see Section 2.3.3), based on the assumption that the ambiguities are estimated correctly. That is, we assume that ignoring the azimuthal subpixel position has not a severe impact on the estimation of ambiguities using wrapped data, as the phase induced by this term is relatively small. The filtering is applied on the vector of residuals between the unwrapped phases and the assumed

deformation model (i.e., residuals of the fixed solution). The filtering is based on the correlation of the azimuthal subpixel position effect and the Doppler baseline. Let e_x be the residual vector of point x, and $e_{x,k}$ the kth element of e_x corresponding to the residual of the kth interferogram. For each $e_{x,k}$, we write:

$$\widehat{e_{x,k}} = (1 + (\Delta f_{dc}^{0k}/\Delta f_{dc}^{M})^p)^{-1}.e_{x,k}, \tag{5.13}$$

where $\widehat{e_{x,k}}$ is the filtered residual, and Δf_{dc}^{M} is is the maximum Doppler baseline which can be set to the maximum Doppler baseline of the dataset. The order factor p allows us to tune the sensitivity of the filter to the Doppler baseline. For example, with $p = 2$, observations with small Doppler baseline are filtered less than in case of $p = 1$ and only observations with very high Doppler baseline are affected. Fig. 5.4 gives an example for a particular PS, and Fig. 5.5 shows the dependency of the filtered phase to the Doppler baselines for different p values. After filtering, the filtered residuals are added to the estimated deformation model and the fixed solution is derived again. The new a-posteriori variance factor has a smaller value due to the smaller residuals, possibly leading to acceptance of the PS. Note that this filtering approach does not estimate and remove the full subpixel position effect (i.e., it is a deterministic approach), and it only reduces this effect in order to reduce the false rejection of PS with a large subpixel position effect.

All three mentioned approaches can be applied based on alternative hypothesis testing during the PSI processing. That is, first the null hypothesis is used (i.e., neglecting the subpixel position effect), and then in the case the candidate is rejected, one of the above adaptations is applied and the PS candidate is tested again with the adapted model (i.e., the alternative hypothesis). However, all of these adaptations should be applied only when it is necessary. Unnecessarily adaptation of the model for all rejected candidates increases the chance of unwrapping errors and also the chance of falsely detected PS (type-II errors). So, these adaptations should only be used for dominant point scatterers with large azimuthal sub-pixel position. Here, we propose a new method for detection of these pixels and apply the proposed adaptations only for detected pixels.

5.2.1   Detection of PS candidates with subpixel position

In order to detect point scatterers with large azimuthal subpixel position, we look at the correlation between residuals (i.e., deviation of the double difference phase observations from the assumed deformation model) and Doppler differences. The idea is that if we neglect the effect of scatterer subpixel position in the mathematical model, this effect should be contained in the residuals, and because of the dependency of this effect to Doppler baselines, the vector of corresponding residuals should have correlation with the vector of Doppler baselines. So thresholding on these correlation coefficients, we can detect pixels with large azimuthal subpixel position. Note that this idea is based on the assumption of a correct ambiguity estimation. In order to evaluate this hypothesis, we simulated time series of residuals for a large number of arcs (10000 arcs), for different kind of pixels (point and distributed scatterers) and compute the correlation of these simulated residuals with Doppler baselines. The residuals are assumed to have normal distribution with zero mean and standard deviation of 2 mm for point scatterers and 6 mm for distributed scatterers. The subpixel position effect is computed using Eq. (5.5) and added to the residuals of point scatterers. The simulation was performed four times with different azimuthal subpixel position (2, 3, and 4 m). In the fourth simulation, azimuthal subpixel positions are uniformly distributed between 0 and 4 meter. The percentage of point scatterers also differs (between 5% and 50%) in order to see the performance of the detection method in different areas(e.g., urban and rural areas). Fig. 5.7 shows the results of the simulation. Red and green curves correspond to distributed and point like scatterers respectively. The results shows that with increasing the subpixel position, it is easier to separate the point like scatterers from other pixels. It is also clear that in areas with more point scatterers (e.g., in urban areas), this separation is more feasible. Table 5.1 presents the statistics about the correct detection rates using the threshold of 0.25. We can conclude that this detection method can effectively detect point scatterers with large azimuthal subpixel position assuming realistic standard deviations used in the simulation. Fig. 5.6 shows the flow diagram of the proposed method for the detection of PS with azimuthal subpixel position and adaptation of the mathematical model.
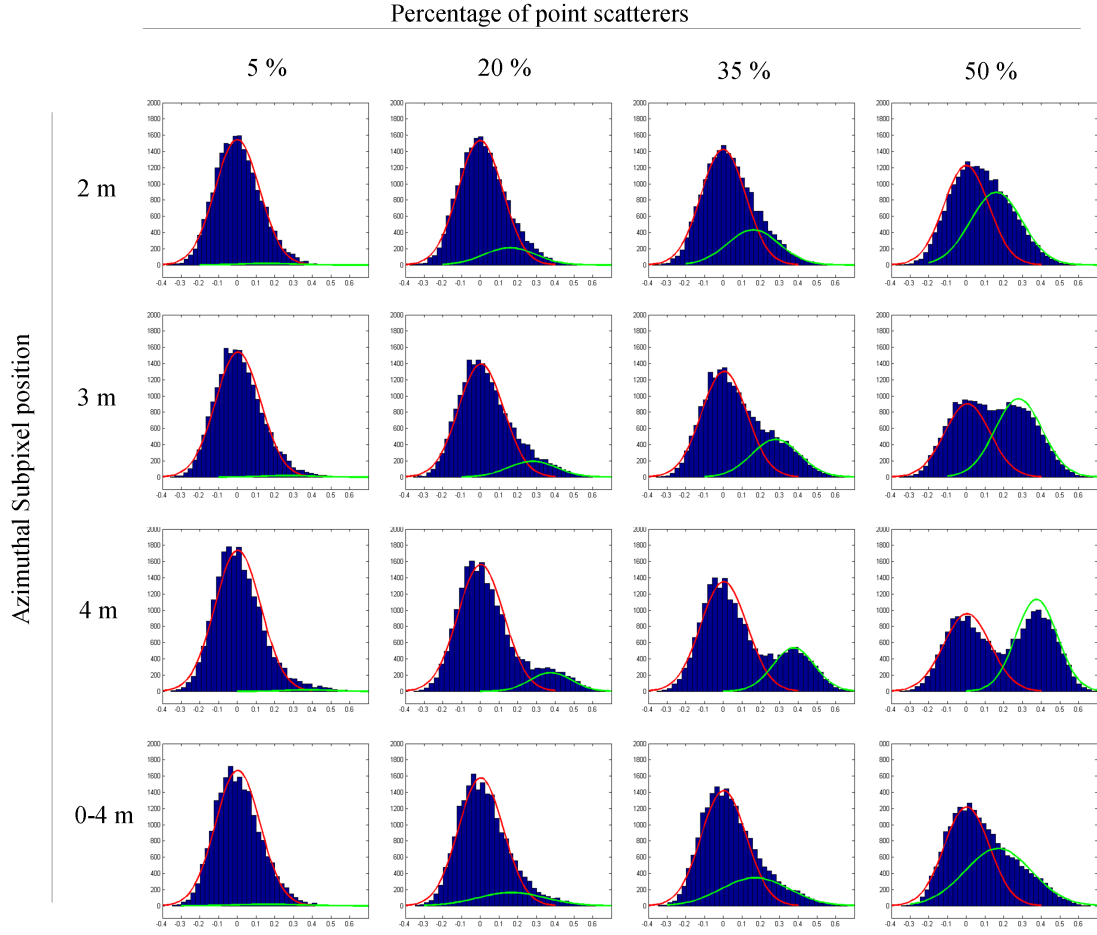
Figure 5.7: *Results of simulation of correlation between residuals and Doppler baseline. The residuals are assumed to have a normal distribution with zero mean and standard deviation of 2 mm for point scatterers and 6 mm for distributed scatterers. The simulation was performed four times with different azimuthal subpixel position (2, 3, and 4 m). In the fourth simulation, azimuthal subpixel positions are uniformly distributed between 0 and 4 meter. Red curve: distributed scatterers. Green curve: point like scatterers. Horizontal axis shows the correlation coefficient between -0.4 and 0.7. It shows that with increasing the subpixel position, it is easier to separate the point like scatterers from other pixels. It is also clear that in areas with more point scatterers (e.g., in urban areas), this separation is more feasible.*

Fig. 5.8 shows the histogram of correlation between residuals and Doppler differences for the real case in the Gardanne dataset. As the subpixel position effect is only important for point scatterers, these histograms contain only pixels with amplitude dispersion smaller than 0.45. The left histogram is based on 1000 pixels in the urban area in Gardanne and the right figure shows the histogram for a larger crop containing 20000 pixels in both urban and rural areas. The red curves are normal distribution curves fitted to the data with a mean of zero. The general shape of both histograms are similar to the results of the simulation. The subpixel position signal is clearer in the urban area as expected. Our interpretation for the cluster of points on the right part of both histograms (outside the red curve) is that these are dominant point scatterers with large azimuthal subpixel position. In the next section we present PSI results obtained by the three proposed adaptations for azimuthal subpixel position on pixels which are detected by the method explained above.

Azimuthal subpixel	Percentage of point scatterers			
position	**5%**	**20%**	**35%**	**50%**
2 m	38%	38%	39%	39%
3 m	69%	73%	74%	74%
4 m	94%	95%	95%	95%
0-4 m	40%	45%	45%	46%

Table 5.1: *Correct detection rate of point like scatterers against distributed scatterers using the threshold of 0.25 on the correlation between residuals and Doppler baselines.*
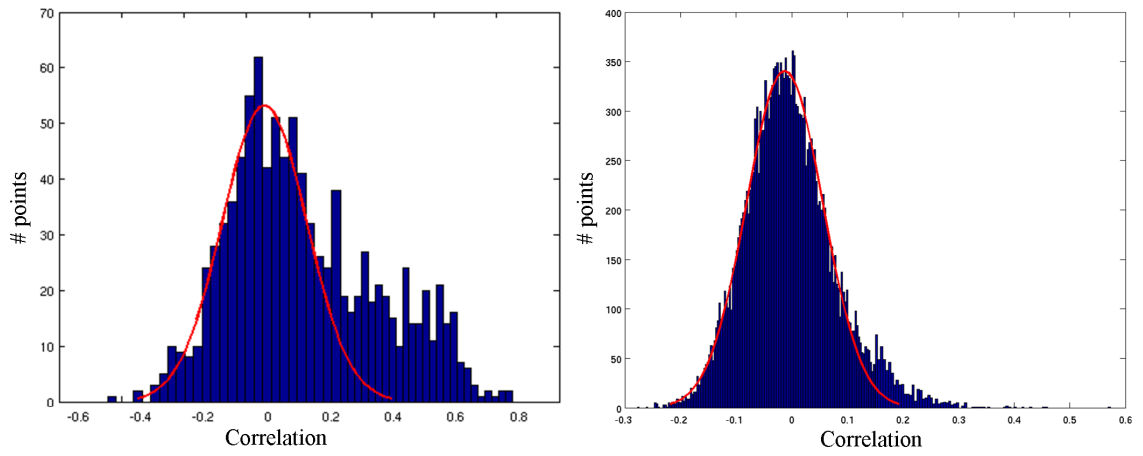
Figure 5.8: *Histogram of correlation between residuals and Doppler differences in the Gardanne dataset.* **Left)** *1000 pixels in the Gardanne city,* **Right)** *20000 pixels in both urban and rural areas.*
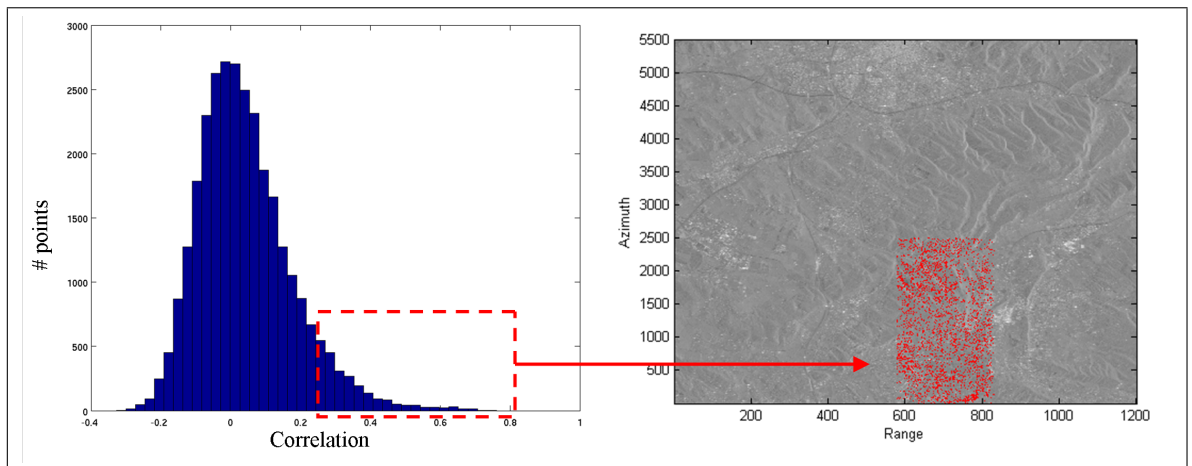
Figure 5.9: **Left)** *Histogram of correlation between residuals and Doppler differences in the deforming area. Points in the red box are detected (by threshold of 0.25 on correlation between Dopplers and residuals) for adaptation of the mathematical model for azimuthal subpixel position effect.* **Right)** *Location of detected pixels.*
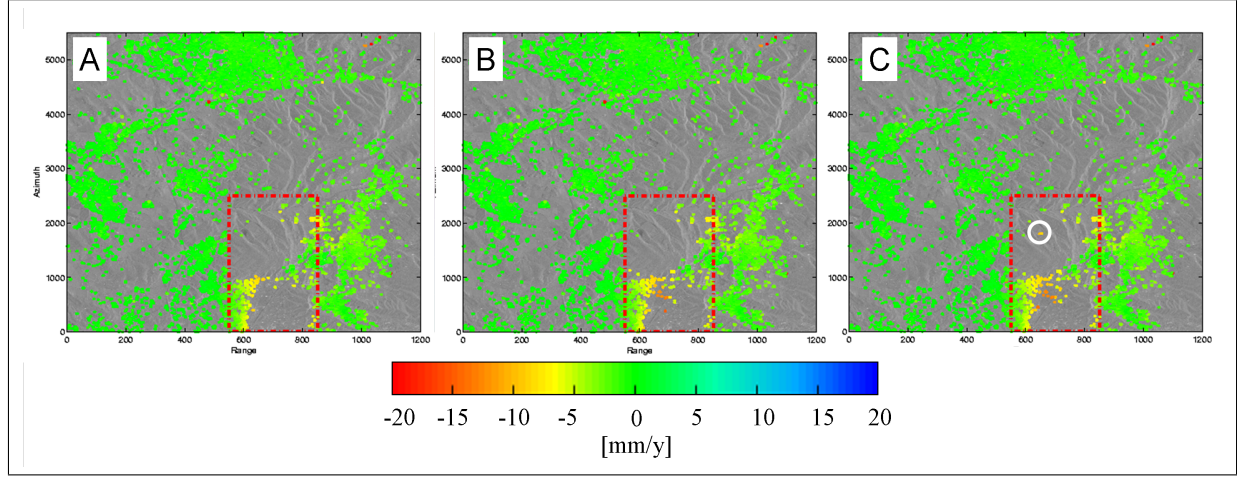
Figure 5.10: *PSI results for different processing runs: (**A**) Method1: PSI processing using adapted functional model with azimuthal subpixel position, (**B**) Method2: PSI results obtained by applying an adopted stochastic model for azimuthal subpixel position, and (**C**) Method3: PSI results obtained by filtering the azimuthal subpixel position effect from observations. Linear deformation rates estimated from the unwrapped time series are shown. Red dashed box is the deforming area. White circle shows the location of the newly detected PS in the S5 area.*

5.3   PSI results

We performed three PS processing runs with the three proposed method for dealing with azimuthal subpixel position effect. Adaptations are applied only on pixels which are detected using the threshold of 0.25 for correlation between residuals and Doppler differences in the deforming area. Totally, 3462 pixels are detected in the initial results and the PS estimation iterated for these pixels with adopted mathematical model. Fig. 5.9 shows the histogram and location of detected pixels. Fig. 5.10A shows the result after iteration of the PS processing using the adopted functional model with azimuthal sub-pixel position (method1). The density of PS did in this case not improve significantly (number of PS increased from 2380 to 2416 (2% improvement)). However, adding the sub-pixel position term in the stochastic model (method2) results in an increased number of PS from 2380 to 2596 in the deforming areas (Fig. 5.10B), that is 9% improvement in PS density in the area of interest. The results of the filtering method (method3) (Fig. 5.10C) also shows an increase in PS density from 2380 to 2600 (9% improvement). Method3 is also capable to detect some new PS with -9 mm/y deformation rate in the center of the subsidence area S5 (white circle) where other methods cannot detect any PS and miss the deformation signal. It is interesting that 95% of the new PS which are detected with method 2 and 3 are the same. Fig. 5.11 shows the histogram of correlation between residuals and Doppler baselines before and after filtering by method3. We can see that the applied filter effectively removed the correlation of residuals with Doppler differences. Table 5.2 summarizes the quantitative results obtained by method3 (filtering). Comparison with Table 3.3 shows the main improvement in the S1 area with 17% improvement in PS density and also increase in the mean and maximum of the deformation rate which are closer to the leveling results (Table 3.2). A spatio-temporal profile of results (Fig. 5.13) also confirms the improvement in deformation pattern of the S1 area. The maximum detected deformation in the S5 area also shows significant improvement from -3 to -10.5 mm/year (converted to LOS deformation). We can see the improvement by capturing the deformation of the S5 area on the interpolated velocity map (Fig. 5.12).

5.4   Discussion

Comparison of the PSI results obtained by three proposed methods reveals that it is better to deal with azimuthal sub-pixel position stochastically rather than functionally in this dataset. The reason that functional estimation of
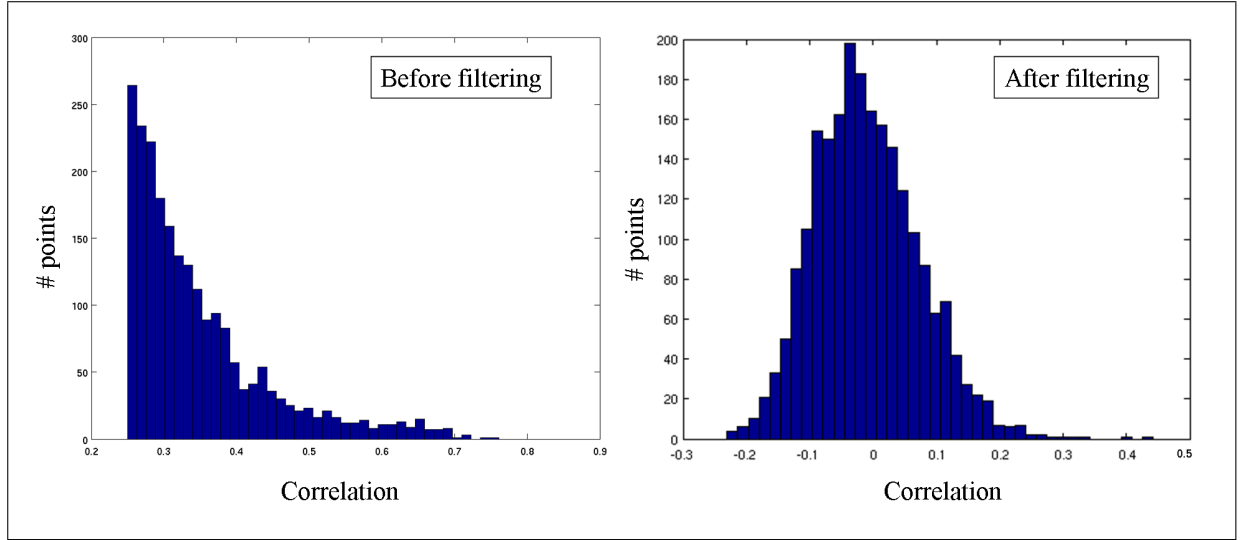
Figure 5.11: *Histogram of correlation between residuals and Doppler baselines for selected PS before and after filtering by method3.*

subpixel position does not work properly can be due to the low variability of Doppler baselines in our dataset. In the case of higher variability of Dopplers, the sensitivity of the functional model to the azimuthal subpixel position effect is higher and this effect can be estimated with better precision. In this study we excluded the 34 interferograms with Doppler baseline higher than 500Hz. It is recommended to apply all three proposed methods on the full dataset in order to evaluate their performance in the case of high Doppler variation.

In Section 5.2.1, it was shown that pixels with large azimuthal subpixel position can be detected by evaluating the correlation between their residuals and Doppler baselines. The results of simulation shows that thresholding on this correlation can effectively detect point scatterers with large subpixel position. In the areas with low number of point scatterers, this detection method may mistakenly detect also a lot of distributed scatterers or pixels with a small subpixel position. This can lead to an increase in the number of type-II errors in the final PSI results. In Table 5.2, we can see that the number of type-II errors increased from 88 in the initial results to 286 in the results of the filtering method (method3). Note that the proposed detection method assumes correct estimation of ambiguities. Therefore, in the areas where the assumed deformation model is not valid (e.g., areas with high non-linear deformation mechanism), and so the chance of unwrapping errors is higher, the performance of the detection method can be worse. The validation of the proposed detection approach needs further research. It is recommended to perform point target analysis for detected pixels in the amplitude domain to estimate their actual azimuthal subpixel position and evaluate the performance of the method.

Item	Whole crop	Deforming crop	S1 area	S2 area	S3 area	S4 area	S5 area
Number of PS	44026	2600	631	9	693	64	28
Improvement (wrt initial results)	0.5 %	9.2 %	17 %	0 %	0.7 %	3 %	8 %
Number of type-II error	1741	286	-	-	-	-	-
Mean of def. rate (mm/y)	-	-	-5.5	-6.1	-2.05	-5.5	-2.3
Max def. rate (mm/y)	-	-	-14.9	-8.3	-28.3	-8.3	-10.5

Table 5.2: *Quantitative results obtained by filtering the azimuthal subpixel position effect from observations (method3).*
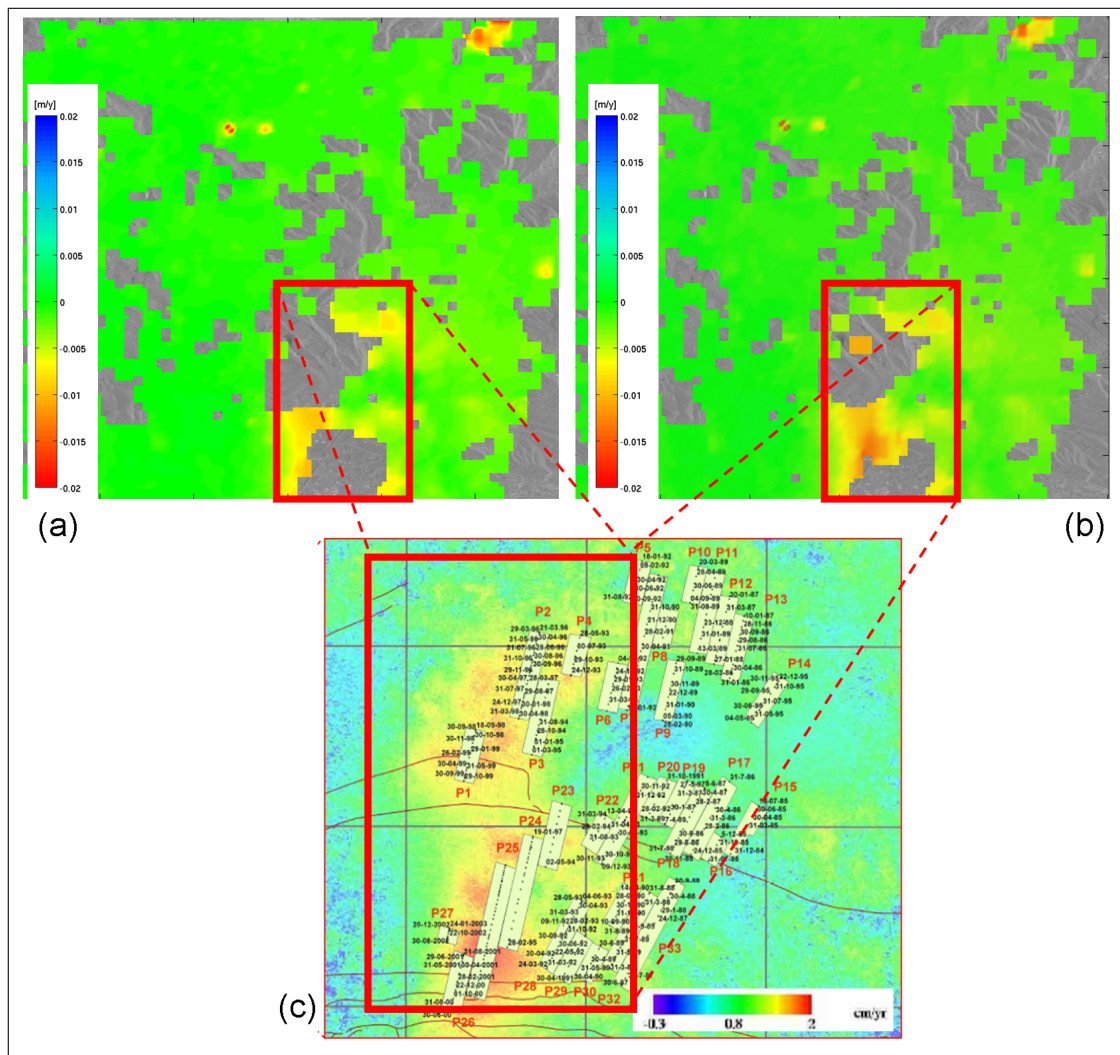
Figure 5.12: *Interpolated velocity map using Kriging: a) the initial results (before adaptation for a subpixel position effect) , , b) the improved PSI results by filtering the subpixel position effect (method3), c)The overlaid mining panels on the differential interferometric data which is obtained by a stacking method using coherent interferograms between 1995 and 2000 (Racoules et al. (2006)). The red box is the deforming area.*
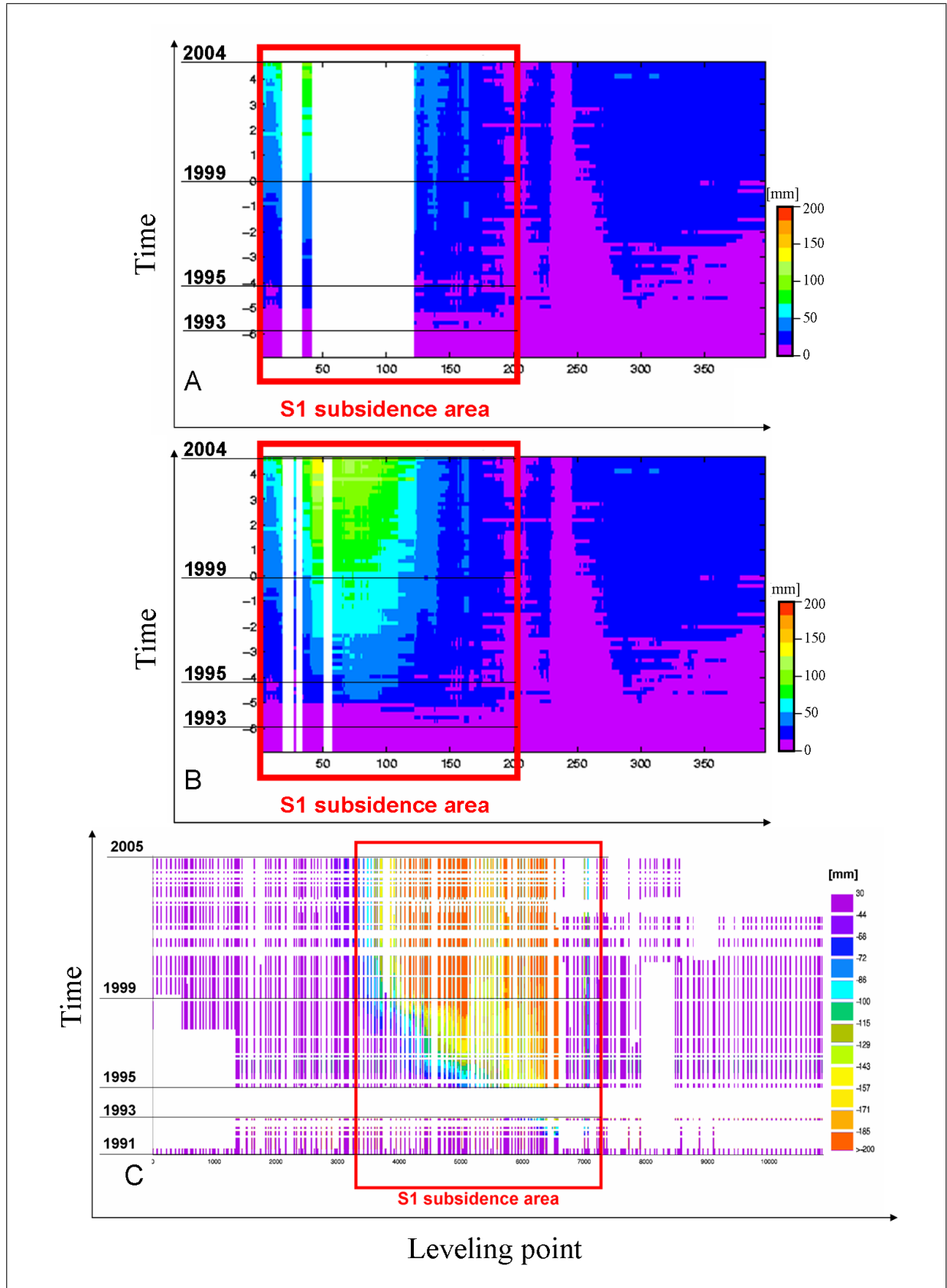
Figure 5.13: *A) AXE spatio-temporal profile on the digitized leveling profile location for the initial result, B) AXE spatio-temporal profile on the digitized leveling profile location for the improved PSI results by filtering the subpixel position effect(method3), C) Leveling results ((Racoules et al., 2006)).*

Chapter 6

Non-linear deformation models

This chapter presents the improvements in PSI results by assuming non-linear deformation models. The new methodology is presented based on adaptive deformation models using alternative hypothesis testing. This methodology is applied on the Gardanne dataset, leading to the improvement in the PS density. The improved PSI result is presented, followed by the discussion about the validity and the performance of the method.

6.1   Background

In Chapter 2, it was described that the parameter estimation (including ambiguity resolution) from interferometric phase measurements in the PSI processing requires an a-priori deformation model. Also two quality assessment criteria were introduced for selection of persistent scatterers: 1) the temporal ensemble coherence, and 2) the a-posteriori variance factor. Both criteria are dependent on the residuals, that is, the deviations between the observations and the assumed deformation model. Therefore, using an imperfect deformation model causes large deviations between the observations and the model, possibly leading to the false rejection of the PS (type-I error). In other words, persistent scatterers with more complex displacement histories than the assumed model may not be detected. The functional model of the PSI processing (Eq. (2.7)) shows that a different number of deformation parameters can be used in the PS estimation. However, with extended deformation models, the redundancy of the mathematical model decreases, resulting in a lower stability of the estimation process. So, it is generally recommended to use as few deformation parameters as possible. The linear deformation model is usually used as it maximizes the rank of the mathematical model. Although in practice, the deformation history during a particular time interval is never completely linear, small deviations from the linear model still allow the correct estimation of ambiguities and the unknown parameters. However, in the case of larger deviations, more advanced deformation models should be applied. On the other hand, using more complex deformation models causes an over-parametrization of deformation in stable areas, increasing the chance of unwrapping errors. Therefore, deformation models adaptive to local deformation mechanisms are required. In this chapter, the general strategy for adaptive deformation modeling is presented. This method is based on sequential hypothesis testing of alternative deformation models (van Leijen and Hanssen, 2007). The new method is applied on the Gardanne dataset in order to increase the number of detected persistent scatterers. The following section will explain the general algorithm of the proposed method, followed by the presentation of the improved results.
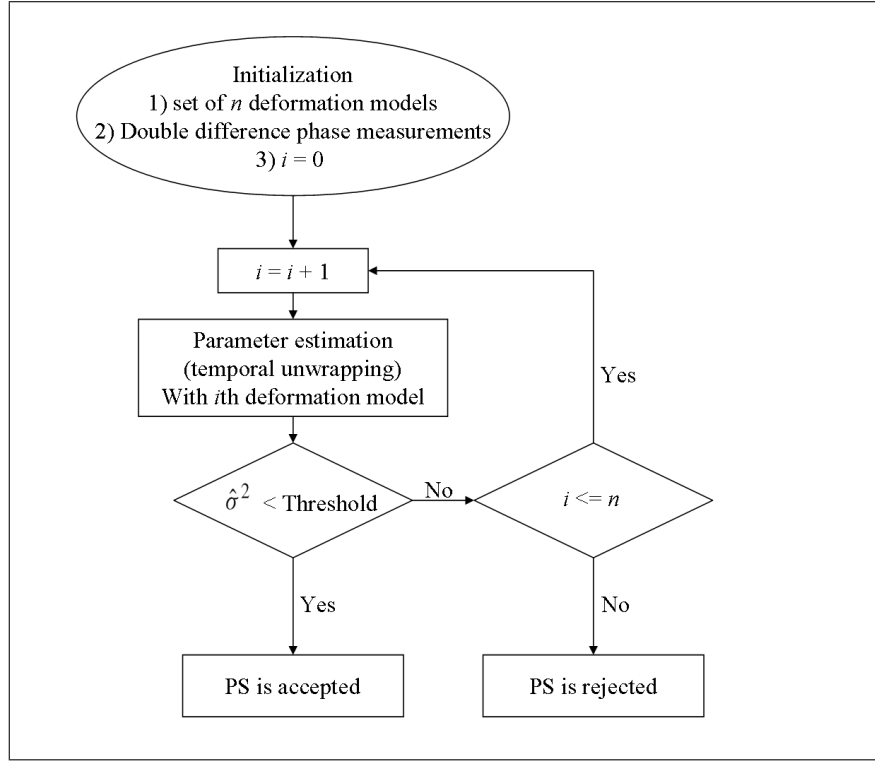
Figure 6.1: *Sequential hypothesis testing flow diagram for a particular arc.*

6.2   Sequential hypothesis testing

This method is applied during the parameter estimation step per 2nd order PS candidates, i.e., Step7 of the PSI processing chain (see Section 2.2.2). It uses adaptive deformation models based on sequential hypothesis testing. Input of the algorithm is the selection of a set of deformation models. Then, each double difference phase observation between two PS candidates is unwrapped in time using the sequential scheme of alternative hypothesis testing until a deformation model fits to the observations well enough. The algorithm starts with the first deformation model (the null hypothesis). A linear model is a good null hypothesis as it maximizes the redundancy of the mathematical model. After temporal unwrapping of the phase observations, the assumed model is accepted when the a-posteriori variance factor $\hat{\sigma}^2$ (see Eq. (2.5)) is smaller than a certain threshold (e.g. 3.0). Otherwise, the next model is tested until the entire set of models is evaluated. Fig. 6.1 shows the flow diagram of the algorithm for each arc.

Different deformation models can be designed and tested, possibly based on a-priori knowledge about the deformation mechanism in the area of interest. As an example, we mentioned some common deformation models here.

- **Linear model:** This is the simplest model which uses only one parameter to describe linear deformation rate:

$$\alpha_1(t) = \frac{-4\pi}{\lambda} t. \tag{6.1}$$

  where $\alpha_1(t)$ describes a deformation model as function of temporal baseline t (to be inserted into Eq. (2.7)).

- **Breakpoint model:** This model is used when the deformation profile can be characterized by two subsequent deformation regimes, separated by an event (see Fig. 6.2**(B)**). Examples of such an event are the start of oil or gas subtraction, or an earthquake. Assuming linear (steady state) displacement before and after the event,

indicated by breakpoint t_b, results, in case $t_b \geq 0$, in

$$\alpha_1 = \frac{-4\pi}{\lambda}[t_1 \ldots t_b \quad t_b \ldots t_b]^T,$$

$$\alpha_2 = \frac{-4\pi}{\lambda}[0 \ldots 0 \quad (t_{b+1} - t_b) \ldots (t_N - t_b)]^T. \tag{6.2}$$

If $t_b < 0$, the model changes to

$$\alpha_1 = \frac{-4\pi}{\lambda}[(t_1 - t_b) \ldots (t_{b-1} - t_b) \quad 0 \ldots 0]^T,$$

$$\alpha_2 = \frac{-4\pi}{\lambda}[t_b \ldots t_b \quad t_b \ldots t_N]^T, \tag{6.3}$$

where N is the number of interferograms. These models are continuous but non-differentiable at the breakpoint. The time of the breakpoint can be defined based on a-priori knowledge of the deformation history or can be estimated from the data. The latter demands a large computational effort, because the phase needs to be unwrapped sequentially applying $t_b = t_2 \ldots t_{N-1}$ to find the best fit.

- **Multiple Breakpoint model:** The breakpoint model can be extended to a multiple breakpoints model (see Fig. 6.2(**C**)). For example, the double breakpoint model can be used when the deformation profile can be characterized by three subsequent deformation regimes, separated by two breakpoints. An example of two breakpoint events is the starting and ending of a mining activity or oil and gas extraction in a particular area. Assuming three subsequent linear displacement regimes, with two breakpoints t_{b_1} and t_{b_2}, in case both t_{b_1} and $t_{b_2} \geq 0$ results in:

$$\alpha_1 = \frac{-4\pi}{\lambda}[t_1 \ldots t_{b_1} \quad t_{b1} \ldots t_{b_1} \quad t_{b_1} \ldots t_{b_1}]^T,$$

$$\alpha_2 = \frac{-4\pi}{\lambda}[0 \ldots 0 \quad (t_{b_1+1} - t_{b_1}) \ldots (t_{b_2} - t_{b_1}) \quad (t_{b_2} - t_{b_1}) \ldots (t_{b_2} - t_{b_1})]^T,$$

$$\alpha_3 = \frac{-4\pi}{\lambda}[0 \ldots 0 \quad 0 \ldots 0 \quad (t_{b_2+1} - t_{b_2}) \ldots (t_N - t_{b_2})]^T. \tag{6.4}$$

If $t_{b_1} < 0$ and $t_{b_2} \geq 0$, the model changes to

$$\alpha_1 = \frac{-4\pi}{\lambda}[(t_1 - t_{b_1}) \ldots (t_{b_1} - t_{b_1}) \quad 0 \ldots 0 \quad 0 \ldots 0]^T,$$

$$\alpha_2 = \frac{-4\pi}{\lambda}[t_{b_1} \ldots t_{b_1} \quad t_{b_1+1} \ldots t_{b_2} \quad t_{b_2} \ldots t_{b_2}]^T,$$

$$\alpha_3 = \frac{-4\pi}{\lambda}[0 \ldots 0 \quad 0 \ldots 0 \quad (t_{b_2+1} - t_{b_2}) \ldots (t_N - t_{b_2})]^T, \tag{6.5}$$

and in case both t_{b_1} and $t_{b_2} < 0$, the model is:

$$\alpha_1 = \frac{-4\pi}{\lambda}[(t_1 - t_{b_1}) \ldots (t_{b_1} - t_{b_1}) \quad 0 \ldots 0 \quad 0 \ldots 0]^T,$$

$$\alpha_2 = \frac{-4\pi}{\lambda}[(t_{b_1} - t_{b_2}) \ldots (t_{b_1} - t_{b_2}) \quad (t_{b_1+1} - t_{b_2}) \ldots (t_{b_2} - t_{b_2}) \quad 0 \ldots 0]^T,$$

$$\alpha_3 = \frac{-4\pi}{\lambda}[t_{b_2} \ldots t_{b_2} \quad t_{b_2} \ldots t_{b_2} \quad t_{b_2+1} \ldots t_N]^T. \tag{6.6}$$

- **Higher order polynomial model:** This model is very flexible, but still requires a certain smoothness of the deformation profile, dependent on the degree of the polynomial used (see Fig. 6.2(**D**) and (**E**)). It can be a good alternative for the breakpoint model, because the time of the event is not required. The model can be formulated as:
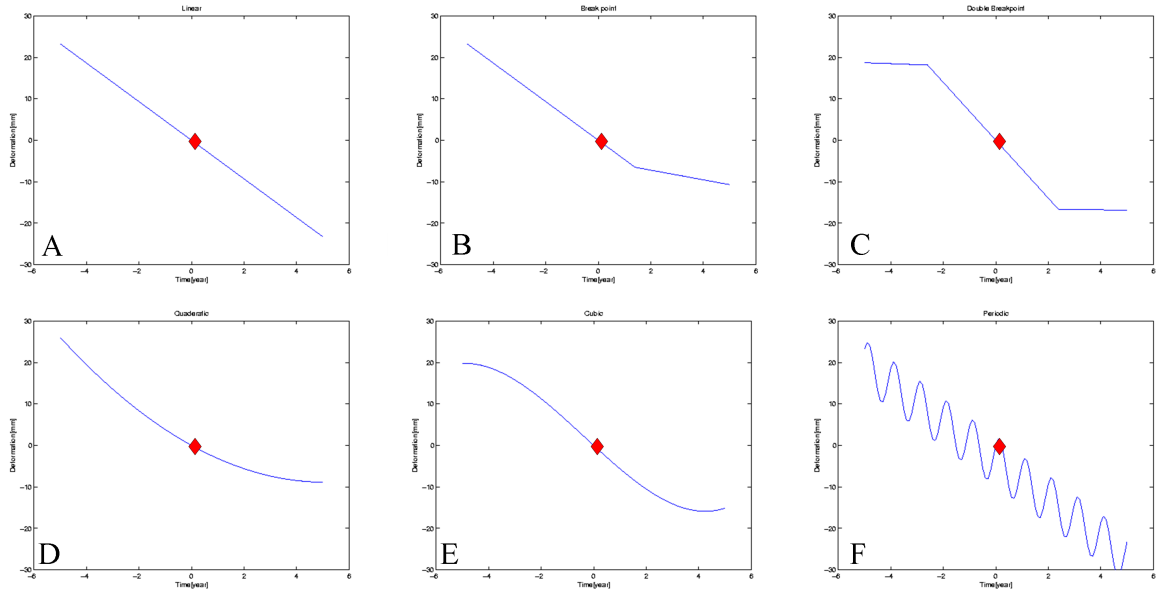
Figure 6.2: *Different deformation models: (A) Linear model, (B) Breakpoint model, (C) Double breakpoint model, (D) Polynomial model with $p = 2$, (E) Polynomial model with $p = 3$, (F) Linear + periodic model. The red dot shows zero deformation at $t = 0$.*

$$\alpha_p(t) = \frac{-4\pi}{\lambda} t^p, \quad \text{for } p = 1, 2, \ldots \tag{6.7}$$

where p is the degree of the polynomial.

- **periodic model:** This model is appropriate for deformation phenomena containing a seasonal effect, e.g., ground water fluctuations and thermal dilatation of buildings (see Fig. 6.2(**F**)). The periodic model can also be used in combination with other deformation models described previously. The model is formulated as (Kampes, 2005):

$$\begin{aligned} \alpha_1(t) &= \frac{-4\pi}{\lambda} \sin(2\pi t), \\ \alpha_2(t) &= \frac{-4\pi}{\lambda} (\cos(2\pi t) - 1). \end{aligned} \tag{6.8}$$

Note that all the assumed deformation models should meet the constraint that the deformation is zero when $t = 0$, because all interferometric measurements are relative to the common master image at $t = 0$.

6.3   Results and Discussions

The sequential hypothesis testing procedure is applied to the Gardanne dataset. The results are visualized in Fig. 6.3. To enable comparison, the figures show the linear deformation rates estimated through the unwrapped time series, even when a non-linear model was used for the unwrapping. Fig. 6.3(a) shows the detected PS and their displacement rate obtained from standard processing (maximum redundancy) using a linear deformation model. Fig. 6.3(b) shows the result after applying the sequential testing scheme using a linear and a polynomial model with $p = 2$. The number of detected PS in the deforming area (the red dashed box) increased in this case from 2380 using the linear model to 3096 (30% improvement). Fig. 6.3(c) shows the results of the sequential
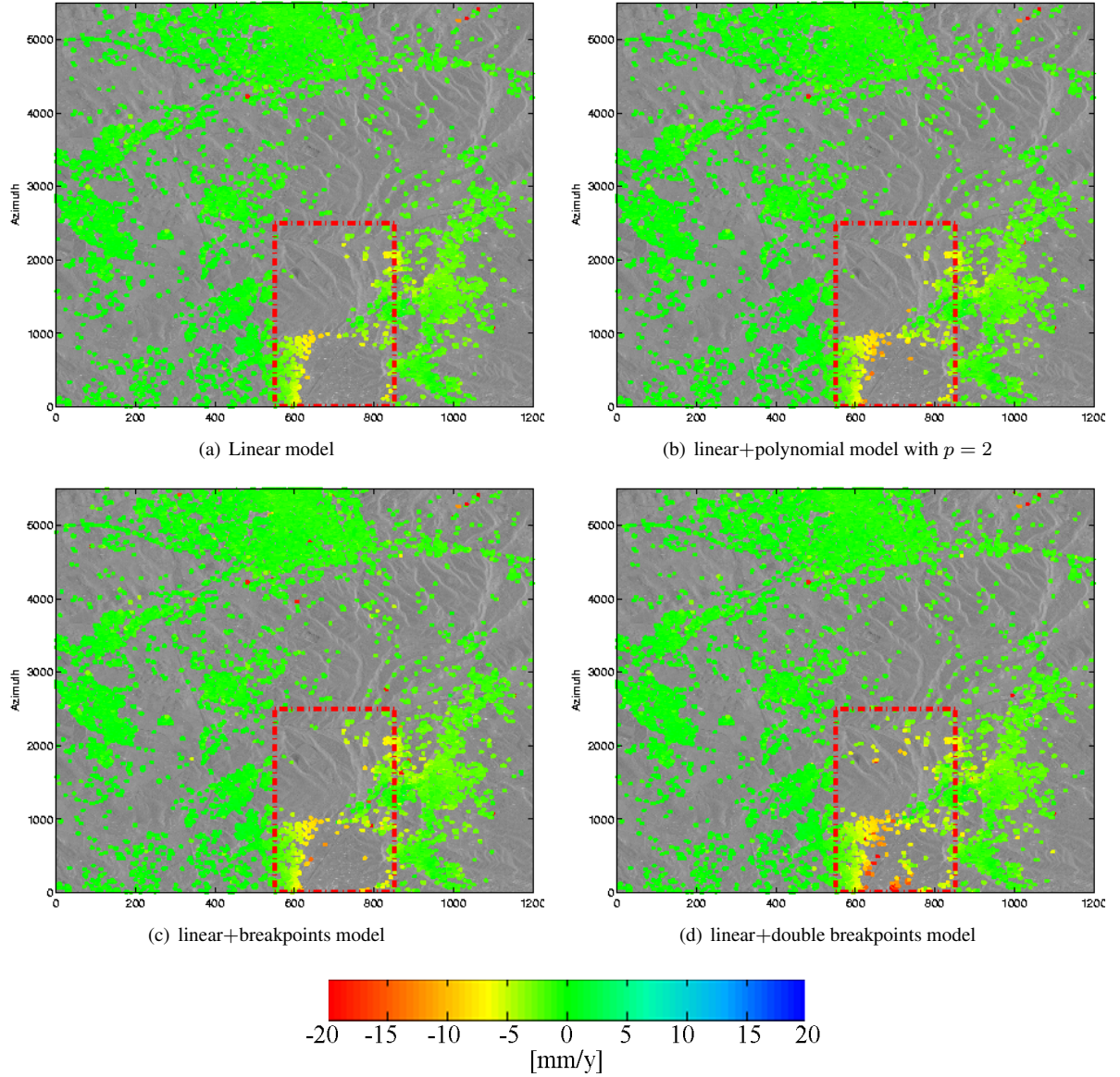
Figure 6.3: *PSI results using the alternative hypothesis testing method: a) The results using a linear deformation model, b) The results using a linear and a polynomial model with p = 2, c)The results using a linear and a breakpoint model. The breakpoint was set a-priori at 19 May 1995, d)The results using a linear and a double breakpoint model. The breakpoints were set a-priori at 19 May 1995 and 24 Jan 1998. Linear deformation rates estimated from the unwrapped time series are shown.*

hypothesis testing using a linear and a breakpoint model. The breakpoint is defined a-priori on 19 May 1995, based on the start of the mining activities in some areas (e.g., the S1 area), and the end of the mining activities in some other areas (e.g., the S3 area, see Table 3.2 and Fig. 6.4). In this case, the number of detected PS in the area of interest increased from 2380 to 2688 (13% improvement). Fig. 6.3(d) visualizes the results after applying alternative hypothesis testing using a linear and a double breakpoints model. The breakpoints were set a-priori at 19 May 1995 and 24 Jan 1998, based on the start and the end of the mining activities (see Fig. 6.4). The number of detected PS increased from 2380 to 4010, that is 68% improvement in the PS density. Table 6.1 summerizes the results for the different subsidence areas.

The results in Table 6.1 shows that the influence of using different deformation models on the PS density varies
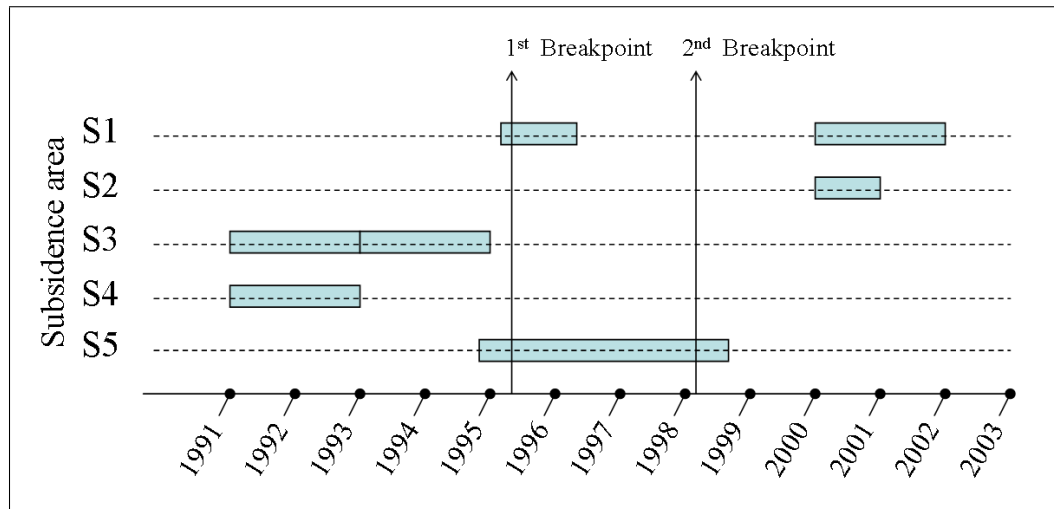
Figure 6.4: *The start and the end time of the mining activities in the subsidence areas. The arrows shows the time of the used breakpoints.*

Model	Item	Whole crop	Deforming crop	S1	S2	S3	S4	S5
	Number of PS	43786	2380	521	9	688	62	26
	Improvement	0%	0%	0%	0%	0%	0%	0%
Linear	**Number of type-II errors**	785	88	-	-	-	-	-
	Mean of def. rate (mm/y)	-	-	-4.4	-5.7	-1.9	-5.1	-1.6
	Max def. rate (mm/y)	-	-	-9.6	-7.7	-28.3	-7.7	-2.8
	Number of PS	47078	3086	782	11	888	73	37
	Improvement	7%	30%	50%	22%	29%	17%	42%
Linear+polynomial($p = 2$)	**Number of type-II errors**	915	109	-	-	-	-	-
	Mean of def. rate (mm/y)	-	-	-5.0	-5.8	-1.9	-5.2	-3.1
	Max def. rate (mm/y)	-	-	-13.8	-7.7	-28.3	-7.7	-10.6
	Number of PS	50346	2688	656	25	1113	95	34
	Improvement	14%	13%	20%	70%	61%	53%	30%
Linear+ 1 breakpoint	**Number of type-II errors**	1319	101	-	-	-	-	-
	Mean of def. rate (mm/y)	-	-	-4.5	-5.3	-2.2	-5.2	-3.1
	Max def. rate (mm/y)	-	-	-14.24	-8.0	-28.3	-7.7	-8.6
	Number of PS	48654	4010	1046	137	995	93	40
	Improvement	12%	68%	100%	1422%	44%	50%	53%
Linear+ 2 breakpoints	**Number of type-II errors**	1160	170	-	-	-	-	-
	Mean of def. rate (mm/y)	-	-	-5.5	-12	-2.2	-5.9	-5.1
	Max def. rate (mm/y)	-	-	-28.2	-24.7	-28.3	-10.5	-28.7

Table 6.1: *The summarized results of the sequential hypothesis testing method for the whole crop, the deforming area, and the different subsidence areas. Improvements are with respect to the initial results.*
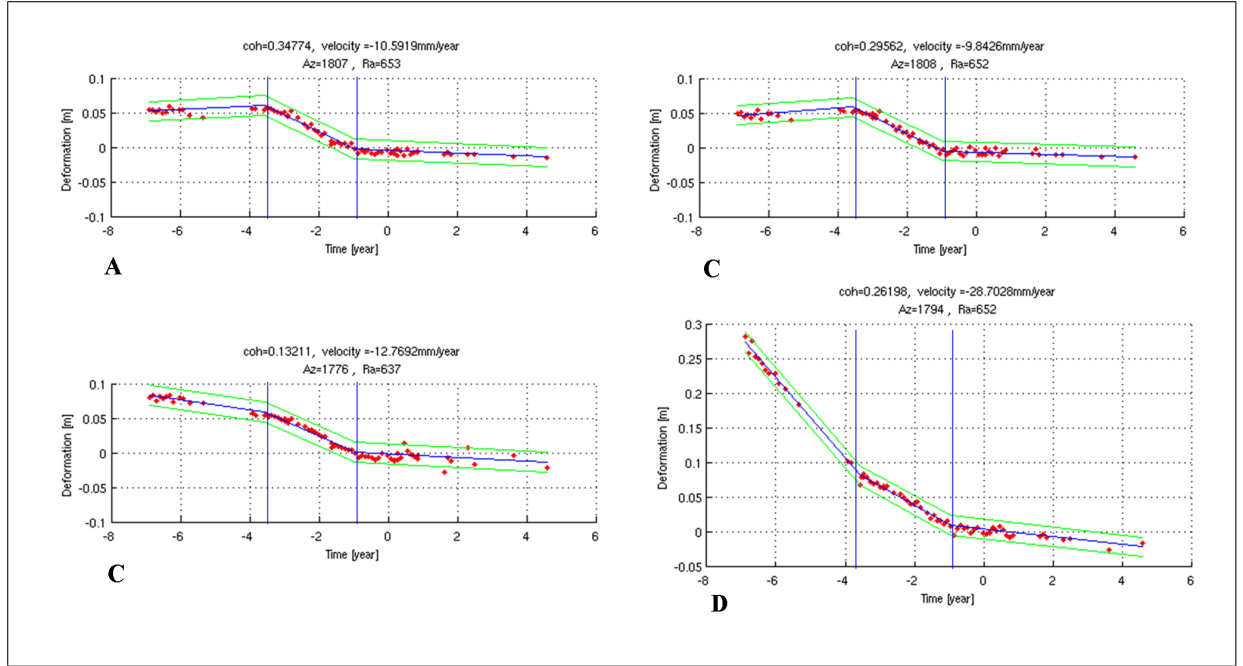
Figure 6.5: *Four time series of some neighboring detected PS in the S5 area, estimated by the sequential hypothesis testing method with the linear and the double breakpoints model. The blue vertical lines shows the time of the breakpoints.*

in the different deforming areas. This effect can be interpreted by considering that the temporal behavior of the deformation also differs in the different subsidence areas. For example, the best result in the S3 area is obtained by the single breakpoint model (i.e., 61%). The time interval of the mining activity in this area (Fig. 6.4) confirms that the single breakpoint model should be the best model for this area among the four applied models. The double breakpoint model also resulted in 44% improvement in the S3 area, which shows that this model is unnecessarily complex for this area, considering the 17% decrease in the PS density with respect to the single breakpoint model. On the other hands, using the double breakpoint model gave a significant improvement in the S1 (100%) and S2 (1422%) areas. The double breakpoint model also detected PS in the center of the S5 subsidence area which other models could not detect any point. Looking at the time interval of the mining activities in the S1 and S5 areas (Fig. 6.4) also confirms that the double breakpoint model is more feasible than the other models. Note the difference between the improvements in the whole crop and the deforming area in Table 6.1. All applied models resulted in comparable improvements in the whole crop (between 7 to 12%), including the stable areas. However, in the deforming areas the improvements are more significant which confirms the feasibility of the alternative deformation models for the deforming areas.

Another type of information in Table 6.1 is the number of type-II errors. The number of type-II errors increased in the sequential hypothesis testing runs (from 785 to 915, 1319, and 1160). However, relative the number of detected PS, the numbers of type-II errors does not vary and its maximum increase is 0.5 percent. (i.e., 1.7 to 2.5% and 3.5 to 4.0% in the whole crop and in the deforming area respectively). These results show that using more complicated deformation models does not increase the number of type-II errors significantly. Note that type-II errors are different from points with unwrapping errors. Type-II errors are incoherent radar targets that show, by coincidence, a low variance and are detected as PS (e.g., PS that are detected at a sea). But points with unwrapping errors are actual PS whose ambiguities are estimated incorrectly (e.g., due to the high displacement rate of the deformation field). In the next paragraph, we will discuss that using higher order deformation models, the number of unwrapping errors is increased.

We have already described that using extended deformation models reduces the redundancy of the PSI mathematical model, resulting in a lower stability of the estimation process, and so increasing the chance of unwrapping
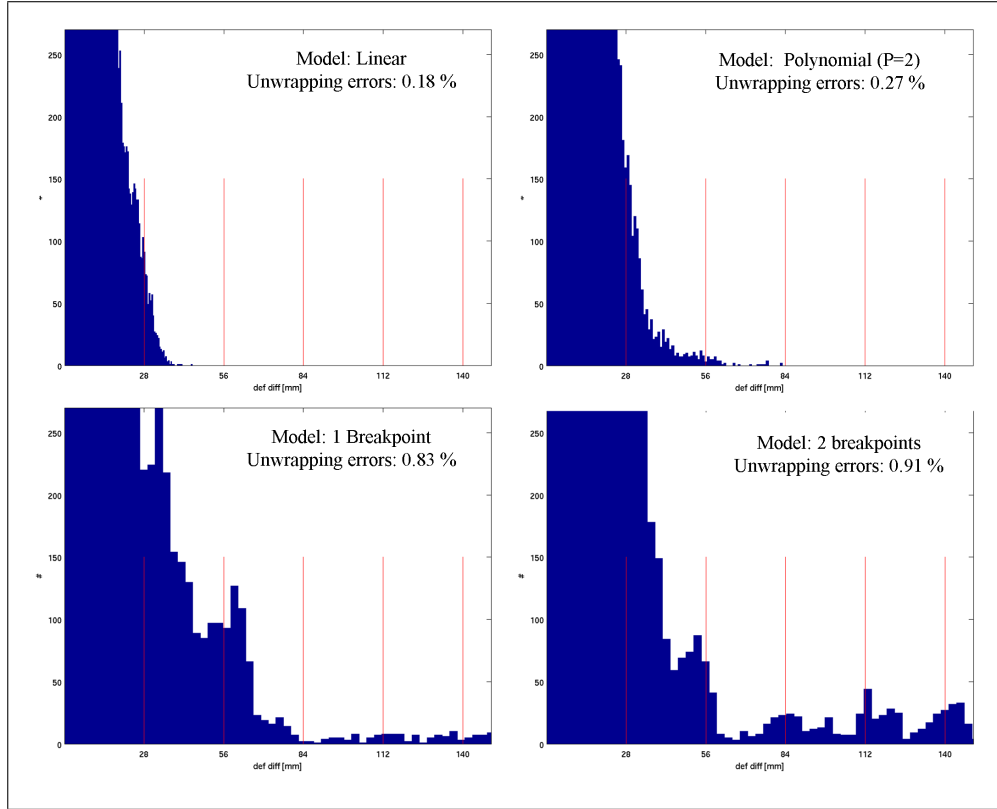
Figure 6.6: *Histogram of differences between time series of neighboring PS for different deformation models in the deforming areas. Red lines show the deformation corresponding to one radar cycle. Unwrapping error percentages shows the percentage of differences which are larger than one cycle (28mm). In order to see the effects of unwrapping errors, only the lower part of the histograms are visualized. Note the peaks of the histograms on the red lines, which confirms the occurring of unwrapping errors. Expectedly, the highest percentage of the unwrapping errors corresponds to the double breakpoint model.*

errors. Also, using more complex deformation models causes the over-parametrization of deformation in stable areas, again increasing the chance of unwrapping errors. Spatial and temporal inconsistency in the deformation time series of some neighboring pixels in our obtained results confirms the increase in the number of unwrapping errors in the case of more complex deformation models. For example, Fig. 6.5 shows four time series of some neighboring detected PS in the S5 area, estimated by the sequential hypothesis testing method with the linear and the double breakpoint model. Assuming spatial correlation in the deformation field, we expect consistent time series for these PS. However, we can see the inconsistency in these time series especially in first time interval (before the first breakpoint). The main reason is the small number of interferograms in this time interval, resulting in lower redundancy and so lower stability of the estimation. For better assessment of the amount of the unwrapping errors, we performed an analysis on the discrepancies of neighboring PS time series in the deforming areas. For each detected point, we subtracted the time series of the neighboring PS from its time series. Assuming the spatial correlation of the deformation, we expect these differences to be close to zero. These differences are computed for all PS in the deforming areas. Fig. 6.6 shows the histograms of these differences for different deformation models. The red lines show the deformation corresponding to one radar cycle. Unwrapping error percentages show the percentage of the differences which are larger than a cycle (28 mm). Note the peaks of the histograms on the red lines, which confirms the occurring of unwrapping errors. Expectedly, the highest percentage of the unwrapping errors corresponds to the double breakpoint model. We can see also very large differences in some time series (up to 6 cycles). These large differences can also be due to the remaining type-II errors which were not filtered in our type-II errors removal strategy (described in Section 3.2.1). We removed type-II errors using their large height residuals, their high deformation rates, and their low coherence. However, the coherence is dependent on the least
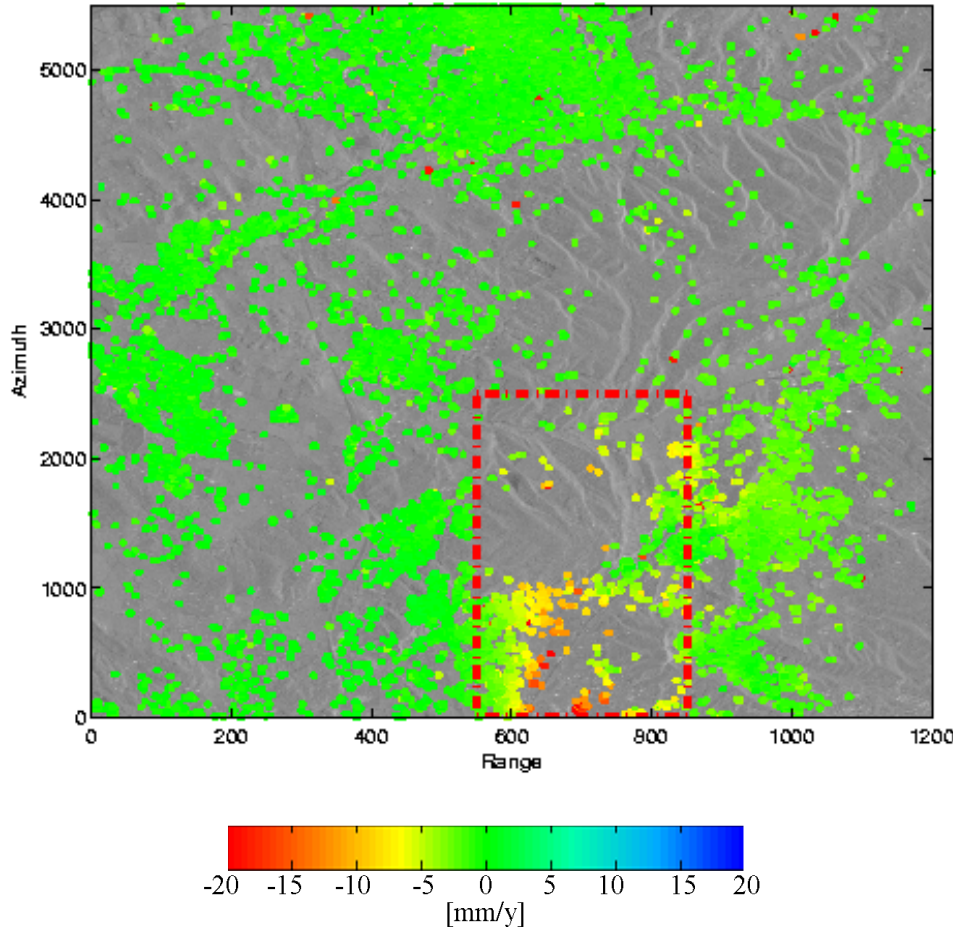
Figure 6.7: *PSI results obtained by the alternative hypothesis testing method using a linear, polynomial $p = 2$, breakpoint, and double breakpoints model. Linear deformation rates estimated from the unwrapped time series are shown.*

squares phase residuals. These residuals do not necessarily have to be large if a point is incoherent. This is particularly true when the mathematical model has low redundancy. Therefore, some type-II errors can pass the filtering and they are included in the results. So the histograms in Fig. 6.6 show the discrepancies due to the unwrapping errors and the remaining type-II errors. These errors suggests that only thresholding on the a-posteriori variance factor is not enough for final selection of PS, and it is necessary to detect and remove the type-II errors, and to detect and possibly correct the unwrapping errors, e.g. by the integrity check of the spatial network (suggested by Kampes (2005)). Note that these errors are not removed in this step. In the next chapter, we will discuss in details the effects of the unwrapping errors, and evaluate different methodologies for removing them.

The different capabilities of the applied deformation models in the different subsidence areas suggests to integrate all of them in the sequential hypothesis testing processing. Fig. 6.7 shows the results. A priori four deformation models were selected: 1) linear, 2) polynomial with $p = 2$, 3) single breakpoint, and 4) double breakpoint model. Linear deformation rates estimated through the unwrapped time series are visualized. The number of PS increased in this case from from 2380 using the linear model to 4352 (83% improvement). This improvement results in better estimation of the final velocity map of the area. Figs. 6.8a and b show interpolated velocity maps using kriging interpolation for the initial results and the results of sequential hypothesis testing method. The velocities are converted from LOS direction to vertical velocities assuming no horizontal deformation. For better comparison of the deformation field shape, Fig. 6.8c shows the overlaid mining panels on the differential interferometric data which is obtained by a stacking method using coherent interferograms between 1995 and 2000 (Racoules et al.
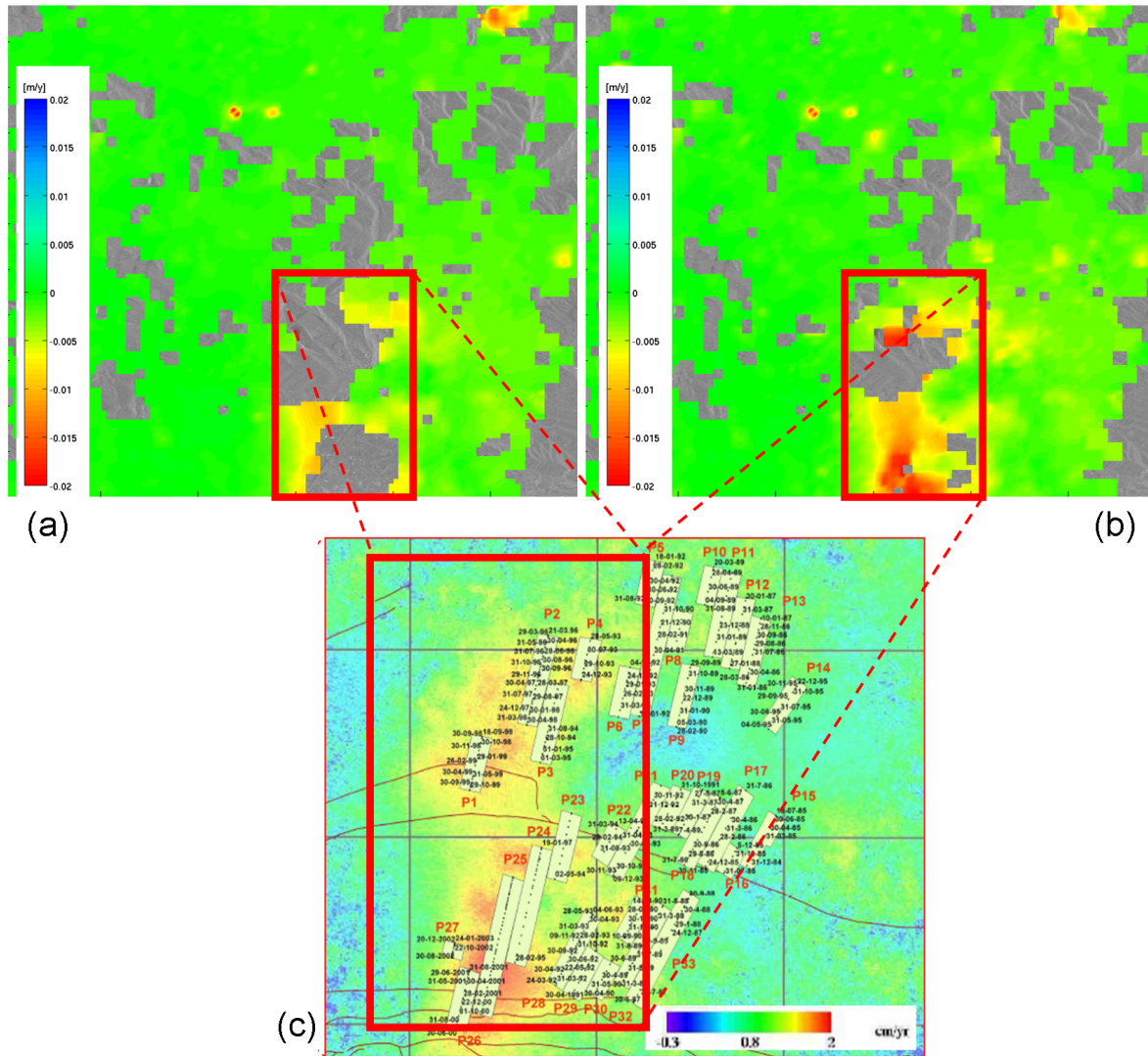
Figure 6.8: *a)Interpolated velocity map using kriging for the initial results (standard PSI with a linear deformation), b) Interpolated velocity map using kriging for the results of the sequential hypothesis testing method with a linear, polynomial $p = 2$, breakpoint, and double breakpoints model, c) The overlaid mining panels on the differential interferometric data which obtained by stacking method using coherent interferograms between 1995 and 2000 ((Racoules et al., 2006)). The red box is the deforming area. Note the difference in the colorscales.*

(2006)). These results show that the adapted algorithm with adaptive deformation models can better catch the deformation signal in this mininig area. In the initial results only the S1, S3, and S4 subsidence areas are captured partially and also underestimated. However, in the improved results all the subsidence areas are detected. Note that in Fig. 6.8a and b, the color scales are different, and the DInSAR results show LOS velocities, while the interpolated maps show vertical velocities. The better estimation of the deformation field can be also seen in the interpolated velocity maps on the leveling profile. Fig. 6.9a and b show the interpolated velocities on the leveling profile by kriging for the initial results and the improved results, and Fig. 6.9c shows the annual cumulative deformation obtained from the leveling data. Clearly, we can see the better estimation of the deformation fields in different subsidence areas especially in the S1, S2, and S3 areas. Note that the colorbars show the same range but their color distributions are slightly different. We can see however, even in the improved results, the estimated deformation rates are underestimated in comparison with the leveling data. The main reasons for this underestimation can be: 1) the unwrapping errors are not removed yet, 2) generally two different deformation regimes are measured by
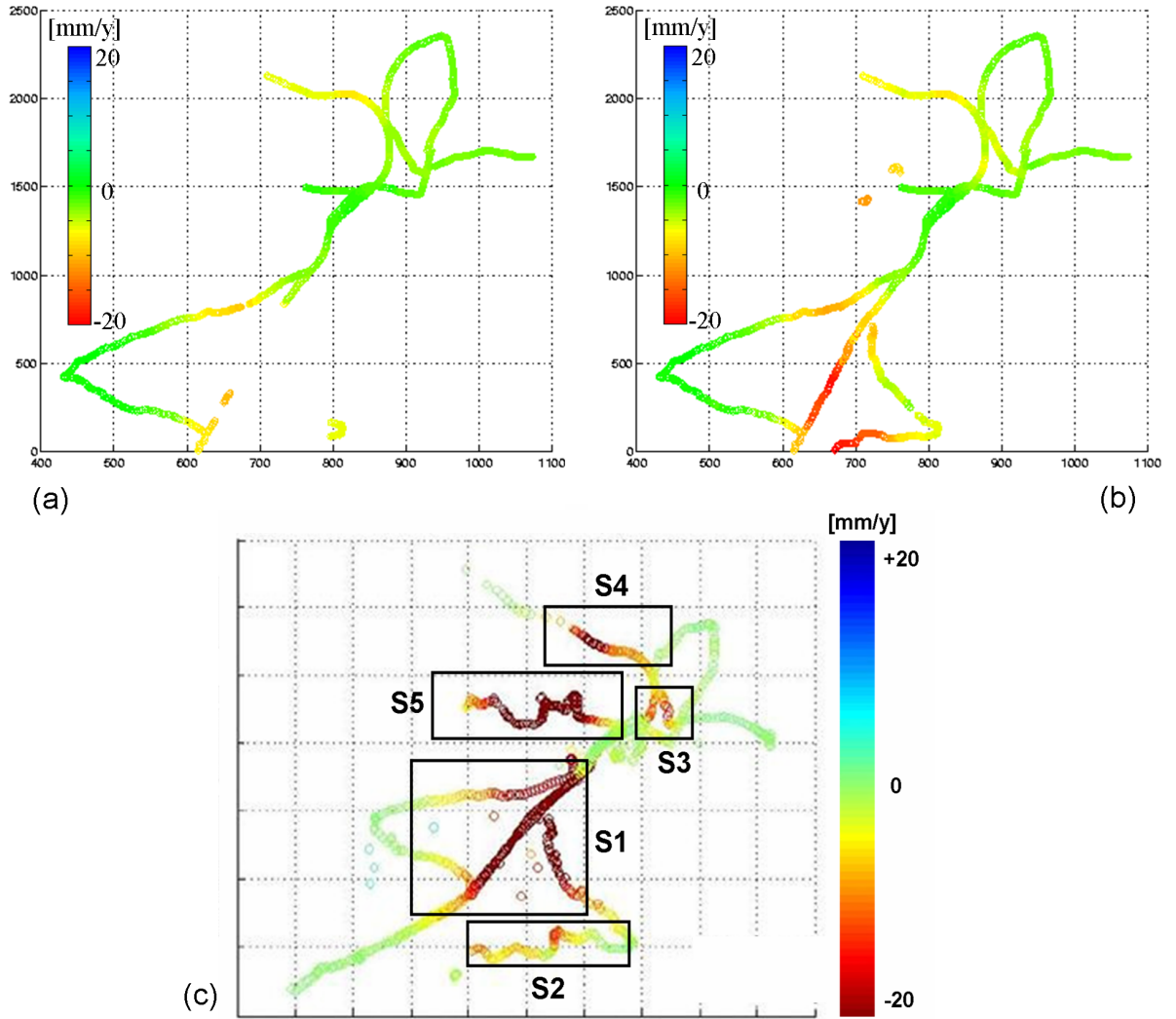
Figure 6.9: *a)Interpolated velocity map on the leveling profile for the initial results (standard PSI with a linear deformation), b) Interpolated velocity map on the leveling for the results of the sequential hypothesis testing method with a linear, polynomial $p = 2$, breakpoint, and double breakpoints model, c) the annual cumulative deformation obtained from the leveling data(Racoules et al. (2006)), and the location of the five subsidence areas.*

leveling and PSI (i.e., objects with leveling benchmarks might subside faster than the ground, for example double bounce PS), and 3) the interpolated results are based on the estimated linear deformation rates of PS, while the leveling data shows the total amount of deformation divided by time. However, detailed analysis of the causes of the underestimation requires access to the numerical validation data which have not been made available.

6.4 Conclusions

The sequential hypothesis testing methodology is introduced and applied on the Gardanne dataset. The proposed method showes to be effective and resulted in an increase in the number of detected PS from 2380 to 4352, that is 83% improvement in the PS density. This improvement significantly improved our results in capturing the

deformation signal in all subsidence areas. However, the results using adaptive deformation models contain more unwrapping errors, showing the requirement for detection and possibly adaptation of these errors.

Chapter 7

Final results and Discussions

This chapter presents the final results and improvements, followed by a discussion about the different improvements and the quality of the final results. First, the effect of the initial network density on the final PSI results is discussed. The PSI results improved by optimization of the initial network are presented. Then, we present the PSI results obtained by integration of the all previous improvements. The performance of the final criterion for the PS selection is evaluated, and some methods are proposed to increase the quality of the final PS selection. Finally, the final results obtained by integration of all improvements and the new selection criterion selection is presented. These results are compared with the initial results. The contribution of different factors in the final improvement is discussed.

7.1   Initial network optimization

At the start of this study, we limited the main research question to focus only on the PSI densification step. So, for all the results presented up to now, the preliminary estimation (i.e., estimation of the initial network of 1st order PS) is the same and is based on the initial settings which were described in Chapter 3. However, in the last stages of the study, we observed that the density of the initial network is very low in the area of interest (Fig. 7.1**A**). Analyzing the sources of this lack of 1st order PS in the deforming area revealed that there was a limited number of 1st order PS *candidates*(PS1c) in this area. That is, in the initial selection of these candidates based on the amplitude dispersion (with the threshold of 0.25), we do not select any candidate in this area. In order to get a denser network, we changed our strategy for PS1c selection. Instead of only selecting the pixels with amplitude dispersion lower than 0.25 in each grid cell, we restrict the algorithm to have at least one PS1c per cell even with higher amplitude dispersion (i.e., select a pixel with the minimum amplitude dispersion in each grid). Note that all the candidates are later evaluated based on their phase behavior. This new strategy results in a density improvement of the 1st order PS (PS1) in the deforming area (Fig. 7.1**B**). Especially, the algorithm is capable to detect some PS1 in the center of the area. For validation, we compare the derived APS by the adapted network against tandem interferograms (same as the APS validation in Chapter 4), and evaluate the final PSI results using the adapted network. Note that for the PSI processing, all settings are the same as the settings which were used for the initial results.

7.1.1   APS Comparison

Fig. 7.2 shows the comparison of the APS derived by the two initial networks (before and after network optimization) against tandem pair interferograms. The improved APS estimation method with detrending and stratification estimation (APS_{tts}) is used in the PSI processing. Table 7.1 summarizes the numerical results of the comparison.
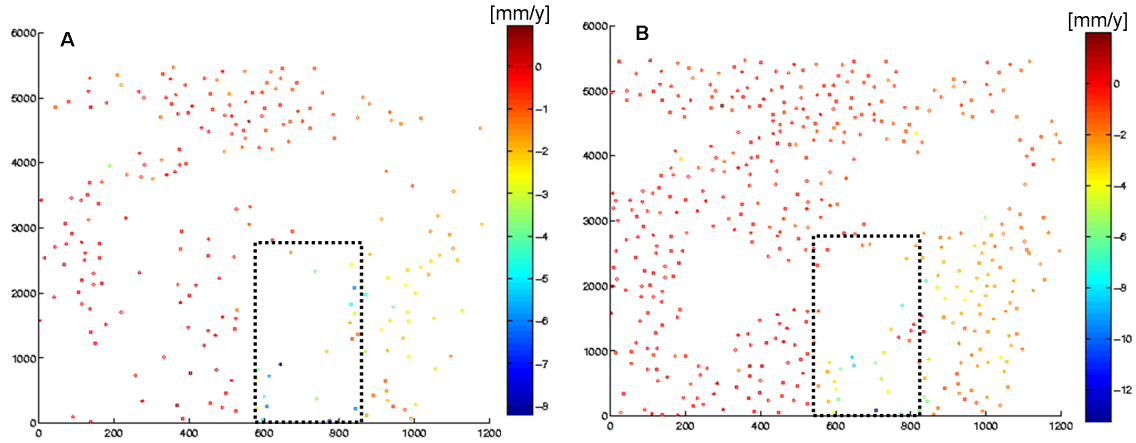
Figure 7.1: *The accepted 1st order PS (PS1) in the Gardanne dataset: (**A**) using the amplitude threshold of 0.25 for selection of PS1c, (**B**) using the new strategy to have at least one PS1c per each grid cell (see Section 2.2.2 to see the difference between PS1 and PS1c). The color shows the estimated linear deformation rate after temporal and spatial unwrapping of the networks. The dashed black box is the deforming area.*

	A	B	C	D	E	F	Mean
rms of difference of tandems with APS$_{tts}$(rad) (before optimization of the network)	1.04	1.14	1.18	1.24	1.47	0.32	1.06
rms of difference of tandems with APS$_{tts}$(rad) (after optimization of the network)	1.04	0.46	0.43	1.05	1.52	0.23	0.89
Correlation between tandems and APS$_{tts}$(rad) (before optimization of the network)	0.92	0.92	0.85	0.86	0.98	0.78	0.88
Correlation between tandems and APS$_{tts}$(rad) (after optimization of the network)	0.95	0.94	0.97	0.89	0.98	0.80	0.91

Table 7.1: *Comparison of 6 tandem interferograms in Fig. 7.2 with APS$_{tts}$ results for the two initial network (with and without optimization)*

The visual assessment of plots shows generally better agreement for the APS derived by optimized network against the tandem interferograms. Also the rms of differences implies that the optimized initial network with better PS1 density can significantly improve the quality of the derived APS. The average of rms values decreased from 1.06 to 0.89 radians (equivalent to a decrease from 4.77 to 4.0 mm). Also in terms of correlation, the results show an improvement.

7.1.2 PSI results

Fig. 7.3 shows the PSI results obtained by using the optimized initial network. The number of detected PS in the deforming area increased from 2380 to 6255, that is 163% improvement in the PS density. The main improvements are for the areas in which we had new 1st order PS in the initial network. These results show the importance of the 1st order PS especially in deforming areas.

7.2 Integration of different improvements

In the last three chapters, we proposed new methodologies for PS density improvement based on the optimization of the APS estimation approach, PS azimuthal subpixel position analysis, and modeling the non-linear deformation mechanisms. In the last section, we also showed that the optimization of the initial network (denser network)
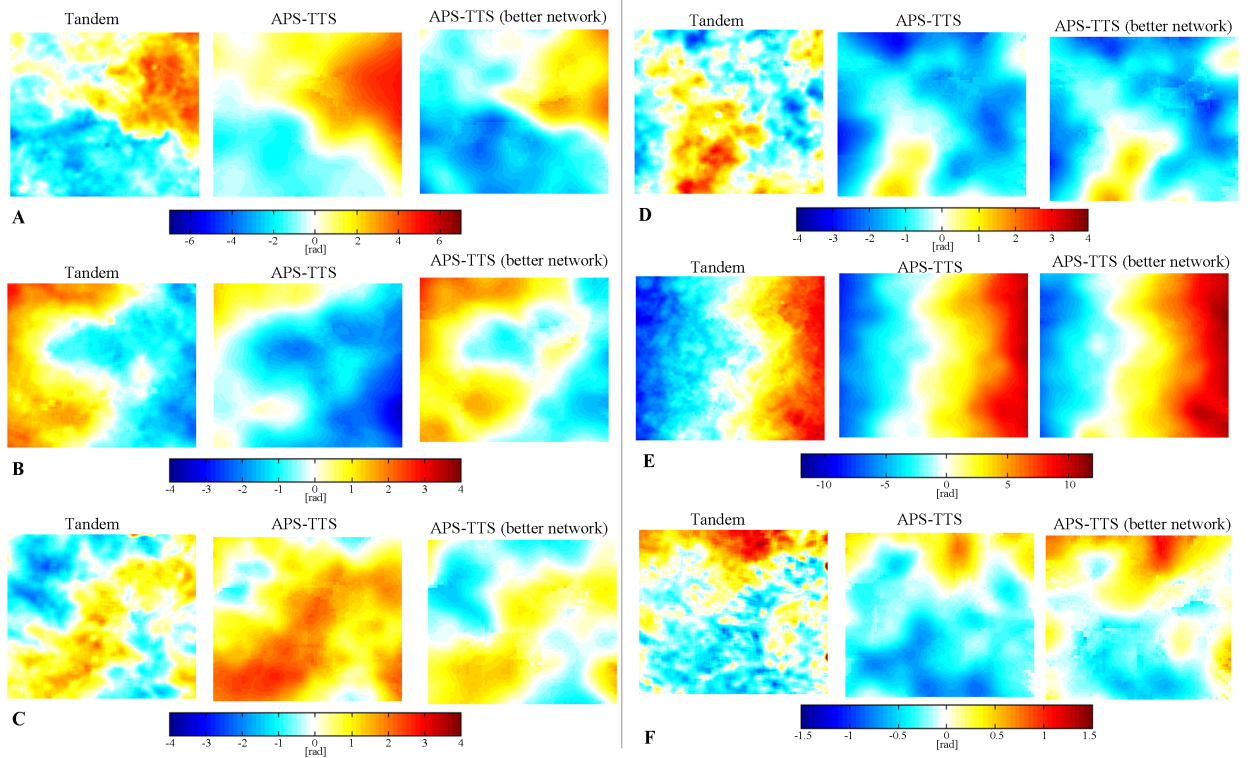
Figure 7.2: *Comparison of six tandem pairs (left column) with corresponding estimated APS with detrending and stratification estimation (APS$_{tts}$ method). Second column shows the estimated APS by the initial network using an amplitude threshold of 0.25 for the selection of PS1c. The right column shows the estimated APS by the initial network using the new strategy to have at least one PS1c per each grid cell. (**A**) Jul 1999, (**B**) Mar 1999, (**C**) Mar 1996, (**D**) May 1996, **E**) May 1999, (**F**) Jan 2000.*

results in denser final PS results. In this section, we present the results obtained by combination of all above proposed approaches on the Gardanne dataset. That is, we applied the following adaptation to the conventional PSI algorithm.

1. Optimized initial network construction using the new strategy to have at least one PS1c per each grid cell for the initial network.

2. Adapted APS interpolation with trend and stratification effects (APS$_{tts}$ method).

3. Sequential hypothesis testing scheme using linear and double breakpoint models. (Only in densification step).

4. Adapted stochastic model for 2nd order PS candidates with azimuthal subpixel position. (The second method proposed in Chapter 5).

Fig. 7.4 shows the results. The density of PS in the deforming area increased significantly from 2380 to 8407, that is 253% improvement in the PS detection capability. Note, however that the result using the adapted algorithm contains more outliers, which could be autonomous moving of some scatterers, undetected type-II errors, or unwrapping errors. This suggests the requirement of better final quality assessment and selection of PS. In order to validate the final results and assess the contribution of each optimization, it is necessary to remove type-II errors and unwrapping errors sufficiently. In the next section, we will analyze different methodologies for removing and correcting of these outliers. After defining the admissible method for identification and removing the type-II and unwrapping errors, we will validate the final results and analyze the contribution of the different optimizations.

(a) the initial results   (b) PSI results with optimized network
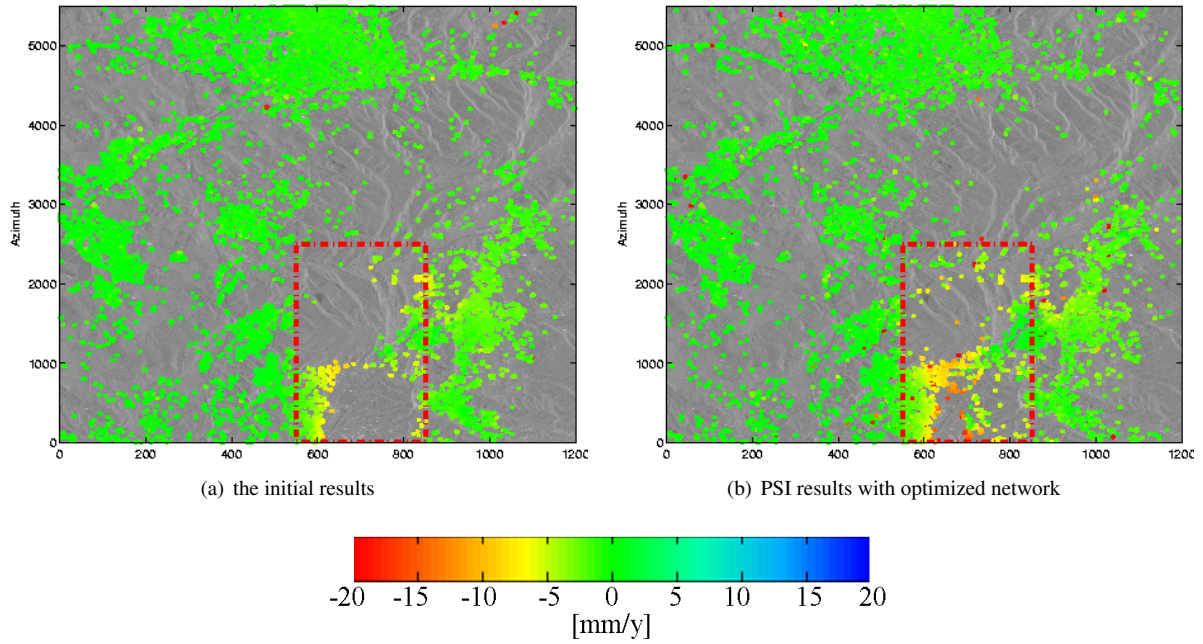
Figure 7.3: *PSI results: a) using the initial network with the amplitude threshold of 0.25 for selection of PS1c, b) using the new strategy to have at least one PS1c per each grid cell for the initial network. Linear deformation rates estimated from the unwrapped time series are shown.*

7.3   Final selection of PS

In Chapter 2, it was described that the final selection of PS is based on the a-posteriori variance factor that is dependent on the deviations between the observations and the assumed deformation model (residuals), and is also dependent on the covariance matrix which describes the variance of and correlation among the observations in the time domain. The drawbacks of using the a-posteriori variance factor for quality assessment of PS can be summarized as follows:

1. the quality criterion for accepting PS should give an indication of the observations precision. However, an a-posteriori variance factor is dependent to deviation of the observations from the pre-assumed deformation model, and hence it is sensitive to model imperfections. So, an a-posteriori variance factor is not necessarily large for incoherent points. Some pixels can show, by chance, consistent phase behavior with the assumed deformation model, leading to falsely detection of PS (type-II errors). On the other hand, coherent points with different deformation mechanisms than the assumed model show larger deviation from the model and are rejected due to the model imperfection, leading to falsely rejected PS or type-I errors.

2. this quality assessment approach is based on the assumption of correct estimation of the ambiguities (i.e., success rate of 1), and it does not include any information about the quality of the estimated ambiguities. Therefore, the final accepted PS can also contain PS with unwrapping errors.

The two shortcomings above are also valid for the quality assessment based on the ensemble coherence. We have already proposed to remove type-II errors by thresholding on their estimated deformation rate and their estimated residual height. So type-II errors with small deformation rates and residual height can still be in the final results. In order to remove the remaining type-II errors and also unwrapping errors, we propose the strategy for ambiguity correctness checking here and apply it on our results to evaluate its performance.

(a) The initial results

(b) PSI results with optimized PSI algorithm
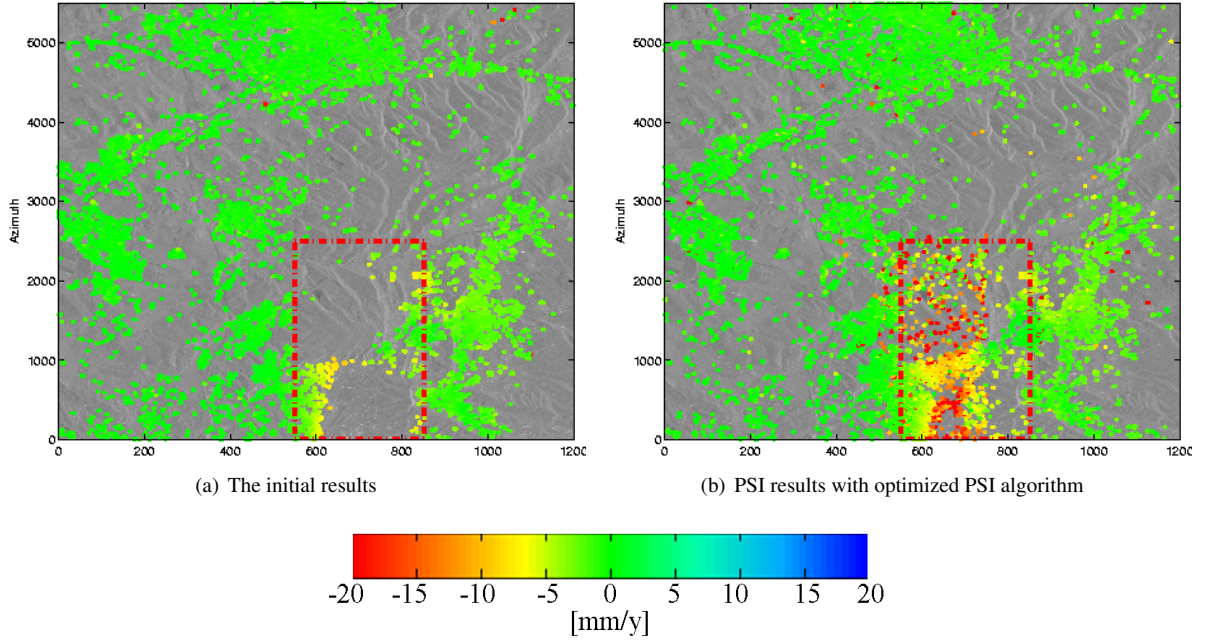
Figure 7.4: *PSI results: a) The initial results, b) The PSI results obtained by integration of the following adaptations: initial network optimization, improved APS estimation, adapted stochastic model for azimuthal subpixel position, and adaptive deformation models with the linear and double breakpoint models. Linear deformation rates estimated from the unwrapped time series are shown.*

7.3.1 Ambiguity correctness checking

In the PSI densification step, each PS2c is unwrapped in time relative to the closest PS1. If each PS2c is unwrapped relative to the three closest PS1c, it is possible to check the correctness of the estimated ambiguities. Each PS2c is unwrapped independently with respect to these PS1c, and all ambiguities converted with respect to the same reference point using the estimated ambiguities in the initial network. Assuming no unwrapping error (success-rate = 1), all three independent estimates of the ambiguity vector should be equal. In this case the PS2c is accepted as PS. It is also possible to relax this condition and accept PS when at least two of the three estimates are equal. Fig. 7.5 shows the initial results and the improved results with three settings: 1) no ambiguity correctness checking applied, 2) PS are accepted only when all three estimates are exactly equal, and 3) PS are accepted when two out of three ambiguity estimates are exactly equal. We can see that the proposed methods reject all PS in the deforming area. It means that all already detected PS in the deforming area have at least one unwrapping error. That is at least one of the ambiguities (not ambiguity vector) is estimated incorrectly at least for one cycle. However, we already saw that most of the detected PS in the deforming area showed a consistent deformation pattern with our expectation (based on the leveling data). So it seems that our evaluation by ambiguity correctness checking is too strict. This raises the question how we can relax this condition.

As obtained ambiguities are results of an estimation procedure, like any other estimates, they have a quality in terms of precision and accuracy denoted by a variance and covariances. We described in the Chapter 2 that the variance of the fixed ambiguities is not only dependent on the variance of the float solution (and hence variance of the observations), but also on the chance of success in the ambiguity resolution denoted by the *success rate*. In our proposed method for checking the correctness of the ambiguities, we assume the success rate equal to one. In this way, even if only one point in one of the estimated time series shows inconsistency for only one cycle with another time series, we reject the arc, while the general temporal pattern of deformation is correct. We should consider that in practice, we never have this condition and the success rate is smaller than one (especially with the bootstrapping method the success rate is lower than for the integer least-squares method). So some unwrapping errors in the results are expected especially in the areas with a weaker mathematical model (e.g., non-urban areas with a high

(a) Initial results, no checking   (b) Initial results, 3 arcs checked   (c) Initial results, 2/3 arcs checked

(d) Improved results, no checking   (e) Improved results, 3 arcs checked   (f) Improved results, 2/3 arcs checked
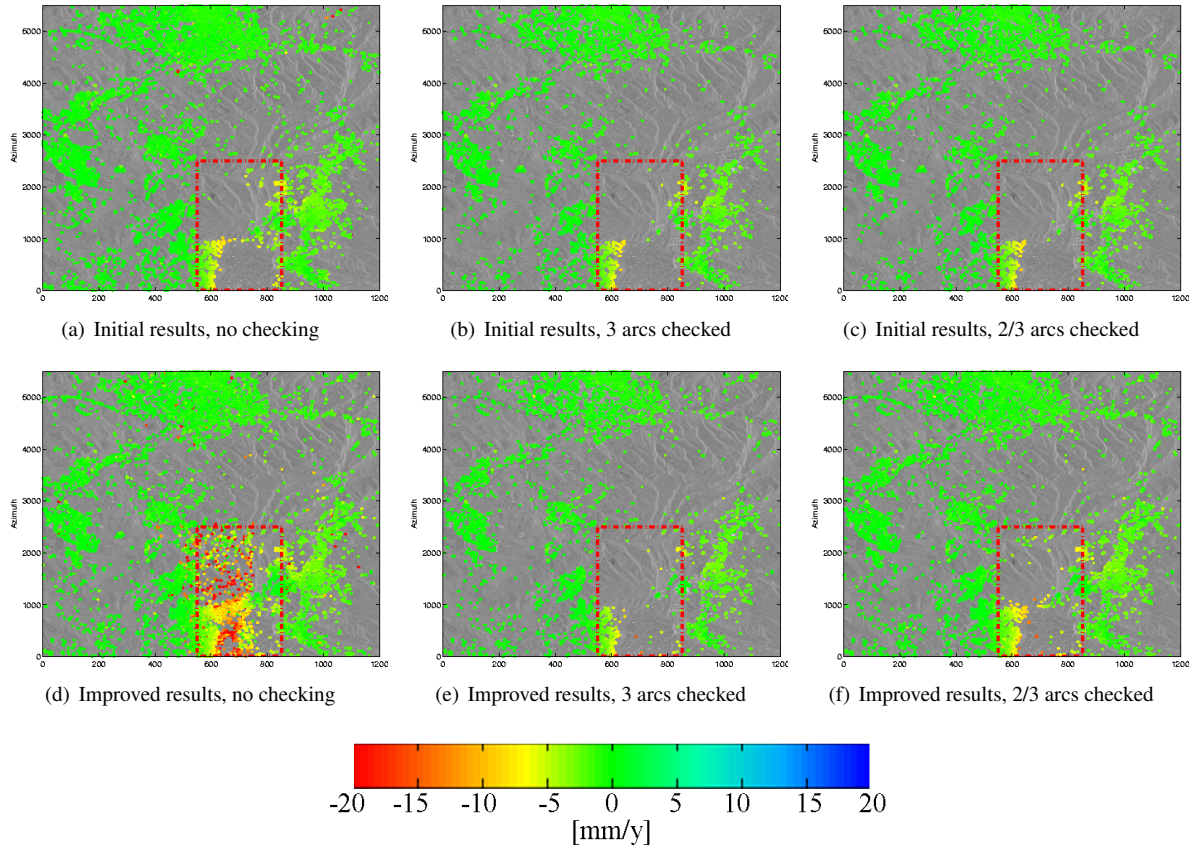
Figure 7.5: *PSI results with ambiguity correctness checking.*

non-linear deformation mechanism). So it makes sense to consider the success rate in our final quality evaluation of PS. Here, we propose to check the correctness of estimated ambiguities based on the comparison of the three independent estimates, however allowing some number of cycles unwrapping errors in the results. With one cycle error, we mean in the three estimates of the ambiguity vector, it is allowed that only one of the ambiguities (not ambiguity vector) differs only for one cycle. Fig. 7.6 shows the results by allowing 1, 2, and 3 cycles errors in the estimated ambiguities. Note that the results are obtained by the bootstrapping method with success rate of 0.91. That is, the probability that we have a wrong estimate for a particular ambiguity vector is 9%. We can see with only allowing 2 cycle unwrapping error in the whole time series the number of detected PS increased significantly especially in the deforming area. We can also conclude that in the deforming area, the number of unwrapping errors are higher due to the nonlinearity and also the fast evolution of the deformation mechanism. With allowing 3 cycle unwrapping errors, the number of PS increased, however we can see more outliers in the this result. In the next section, we present an alternative approach to deal with unwrapping errors and type-II errors based on the spatial and temporal consistency of PS time series.

7.3.2 Spatio-temporal consistency

We discussed already that final PSI results can contain pixels which show good coherence (or low variance) by chance. These pixels are type-II errors. We removed type-II errors in our results based on their large deformation rate, large residual height, and low coherence. However, still some type-II errors can be in the results (in the case that they show small deformation rate with small residual height). However, because these pixels show coherent phase behavior based on chance, they are usually isolated points which do not have consistent phase behavior in comparison with their neighboring PS. Here, we introduce the spatio-temporal consistency (STC) (Hanssen et al.,

(a) Improved results, no checking

(b) Improved results, 3 arcs checked, 1 cycle error allowed

(c) Improved results, 3 arcs checked, 2 cycle error allowed

(d) Improved results, 3 arcs checked, 3 cycle error allowed
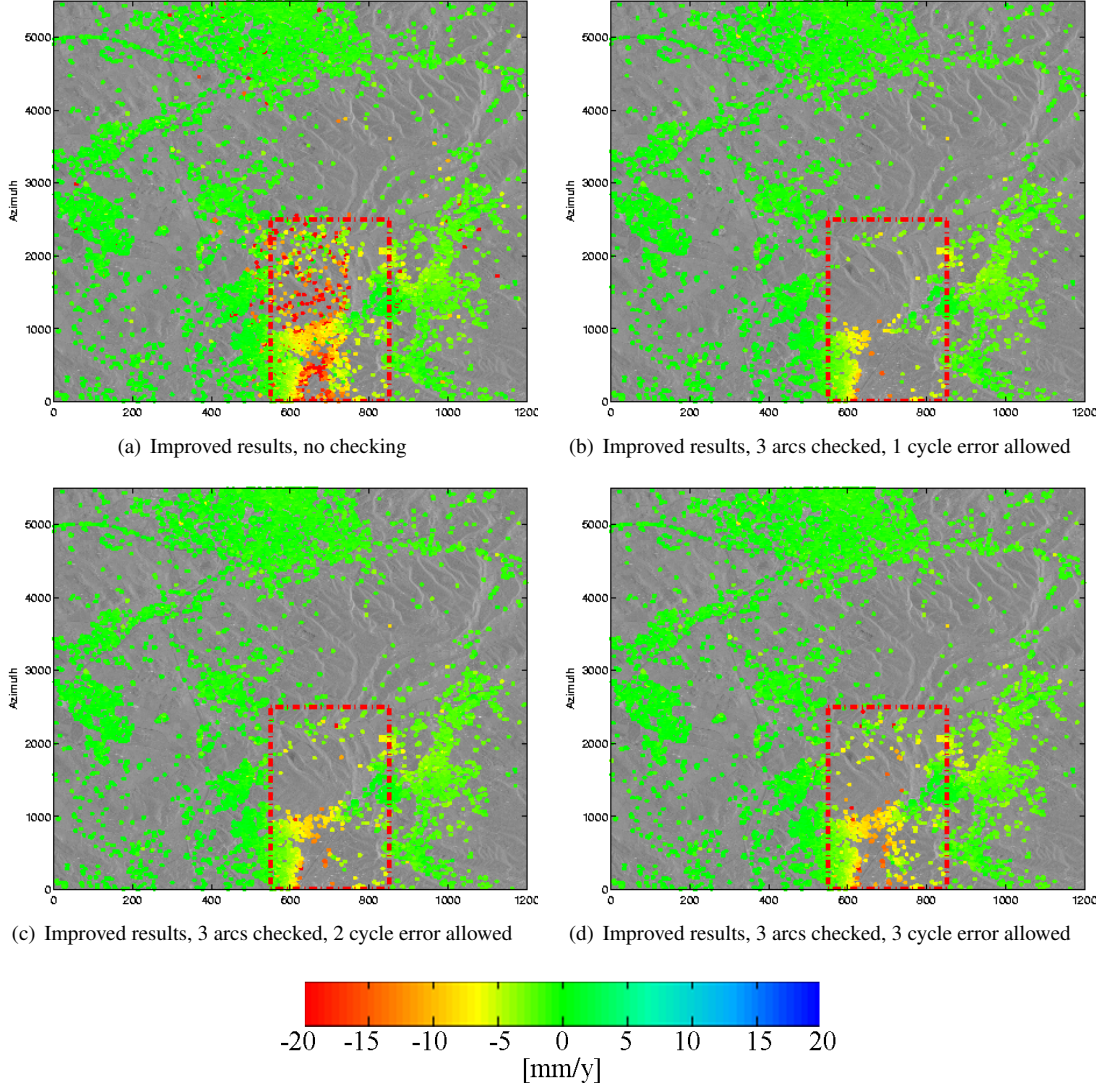
Figure 7.6: *Improved PSI results with ambiguity correctness checking: 3 independent estimates are compared. a) no checking applied (#PS = 41288), b) 1 cycle error allowed (#PS = 31909), c) 2 cycles error allowed (#PS = 34281), d) 3 cycles error allowed (#PS = 36377).*

2008) in order to evaluate the consistency of each PS time series with the time series of its neighboring PS in the space and time domain. The advantage of this quality measurement is that it is not dependent on the assumed deformation model and can better imply the measurements quality. It is also capable to detect type-II errors, as they should not have spatial consistency.

The spatio-temporal consistency of a PS is obtained by comparing its behavior in time and space with nearby PS. The nearby PS are selected between a minimum and a maximum distance. The minimum distance should avoid the selection of sidelobes, as sidelobes of each PS always show a consistent behavior. In our dataset, a minimum range of 50 meters and a maximum range of 500 m is used. After selecting the nearby PS for a particular PS, the double differences (in space and time) between the time series of the PS and the nearby PS are calculated. After calculation of the RMS error [mm] of these double differences, the minimum RMS error is assigned as the STC of the PS. Hence, the spatio-temporal consistency is defined as:

$$\rho = \min_{\forall p} \frac{\lambda}{4\pi} \sqrt{\frac{1}{N-1}((\phi_R^n - \phi_P^n) - (\phi_R^{n+1} - \phi_P^{n+1}))^2}, \tag{7.1}$$
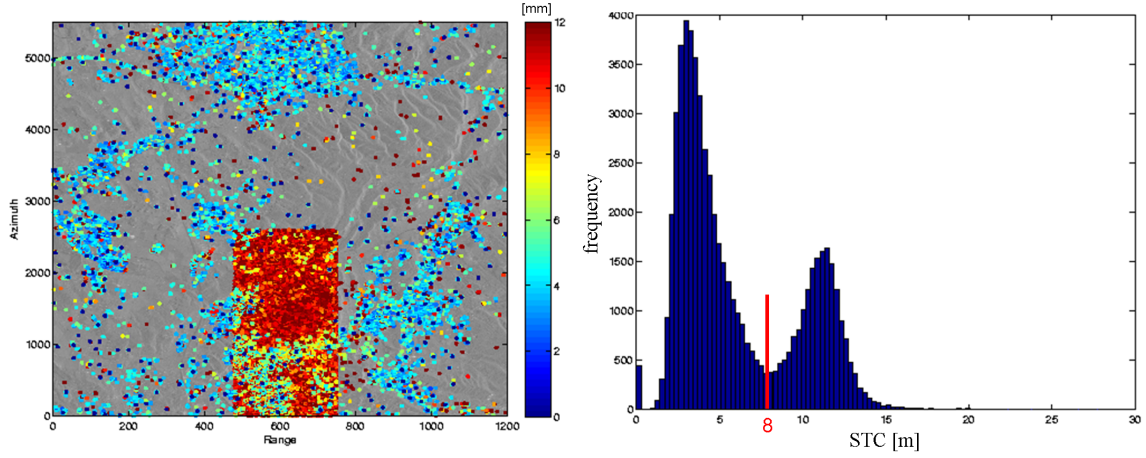
Figure 7.7: *Left: Spatio-temporal consistency (STC) for all 2nd order PS candidates with the a-posteriori variance factor smaller than 3. Right: Histogram of STC values.*

where P is the neighboring PS, R the PS under consideration, N the number interferograms, λ the radar wavelength, and ϕ is the unwrapped phase in the time series. Taking the minimum RMS error, the influence of the spatial deformation pattern is assumed to be minimized, thereby best representing the measurement noise. For both type-II errors and also large unwrapping errors we expect large value of ρ. We computed the spatio-temporal consistency for our improved results. Fig. 7.7 shows the values and the histogram of ρ for all pixels which have an a-posteriori variance factor smaller than 3 (i.e., we did not remove any outliers or type-II error). The area of interest in which we tested all pixels is clearly outlined. Based on the histogram we used the threshold of 8 mm to remove type-II errors, and select the final PS. Note that the STC for the 1st order PS (PS in the initial network) are assigned to zero, as they are already checked and evaluated in the network construction step. Also, When no nearby PS are present within the minimum maximum range, no STC is assigned to the PS. So isolated points (type-II errors or autonomous moving PS) will get a high STC value. Therefore, this quality measure is especially suitable for spatially correlated deformation phenomena. Fig. 7.8a shows the results using an STC threshold of 8 mm for selection of the final set of PS. We can see that this approach can remove effectively the outliers and the type-II errors. However we should consider that the PS with unwrapping errors but with good consistency in time and space are included in the results.

Based on the experiments for final selection of PS presented in this section, we decided to use STC thresholding for the final selection of PS and removing of the type-II errors. We decided to keep PS with unwrapping errors but with acceptable STC in our results and not to remove them. In the next section we compare our final results with the initial results and try to validate the results against the available reference information.

7.4   Final results

In this section, the final results integrating all topics which are studied in this project are presented. The following adaptations are applied to the conventional PSI algorithm.

1. Optimized initial network construction using the strategy to have at least one PS1c per each grid cell for the initial network.

2. Adapted APS interpolation with trend and stratification effects (APS_{tts} method).

3. Sequential hypothesis testing scheme using linear, and double breakpoint models. (Only in densification step).
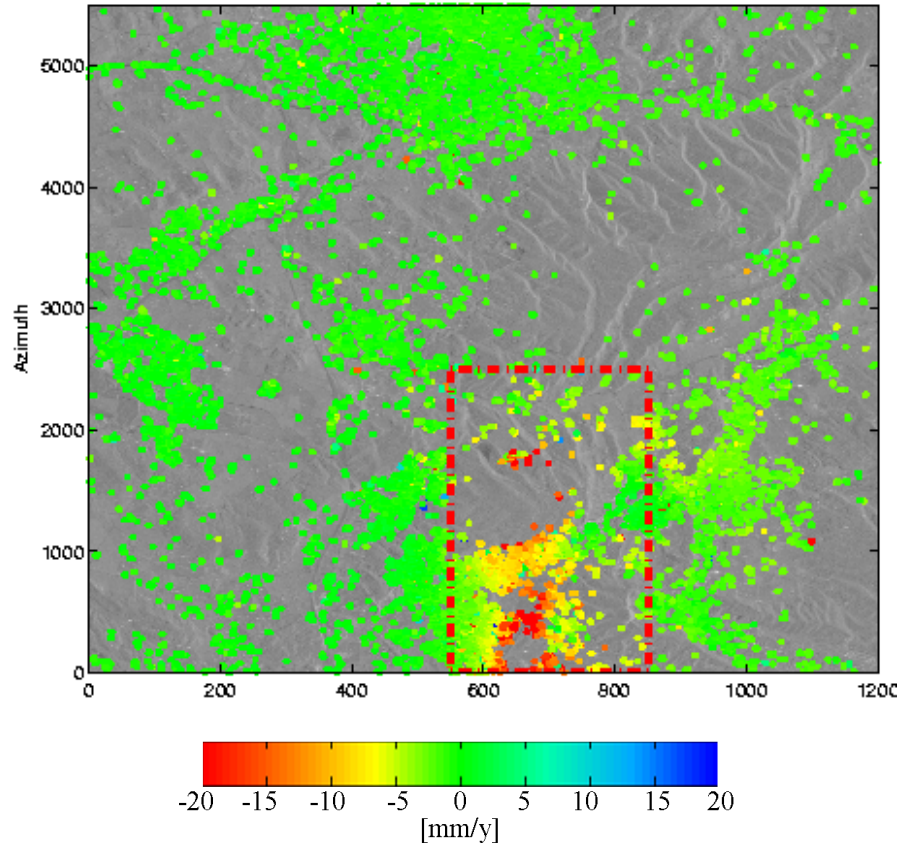
Figure 7.8: *Improved PSI results STC smaller than $8mm$ ($\#PS = 42067$).*

4. Adapted stochastic model for 2nd order PS candidates with azimuthal subpixel position. (The second method proposed in the chapter 5).

5. Final PS selection based on a-posteriori variance factor smaller than 3 and STC value smaller than 8 mm.

For better comparison against the initial results (the results before applying the adaptations), these results are computed again with the mentioned methodology for final selection of PS. Fig. 7.9 shows the initial and the final results. The number of PS in the deforming area increased significantly from 2382 to 8020, that is 236% improvement in the PS detection capability. Table 7.2 summarizes the quantitative results about the PS density and the number of removed type-II errors in both results. We can see that the number of type-II errors in the whole crop also increased from 1197 (4%) to 5547 (13%) as is expected especially due to the decreased rank of the mathematical model using the double breakpoint model. Table 7.3 shows the improvements in the PS density and the deformation rate in the different subsidence areas (see Fig. 3.8). Generally, the number of PS increased in the all subsidence areas. The maximum and the mean of the deformation rates in the different areas also shows the improvements in capturing the deformation signal in these areas. The most significant improvements in the PS density are in the S1, S2, and S3 areas with urbanized landscape. Still the number of PS in the north part of the deforming area (S4 and S5) is low mainly due to temporal decorrelation because of the non-urban landscape (see also Fig. 3.6). The main improvement is in the areas in which we detect new 1st order PS in the initial network. Again in the north part of the deforming area, we do not have any 1st order PS. In addition to the landscape of this area (mainly forest and agricultural), the highly nonlinear deformation can cause low PS density.

The improvement in the captured deformation signal can also be seen in the interpolated velocity map of the area (Fig. 7.10) and in the interpolated velocity map on the leveling profile Fig. 7.11. We can see that the deformation signal of all subsidence areas is captured better in the improved results than the initial results. However, comparison

(a) The initial results   (b) The final results
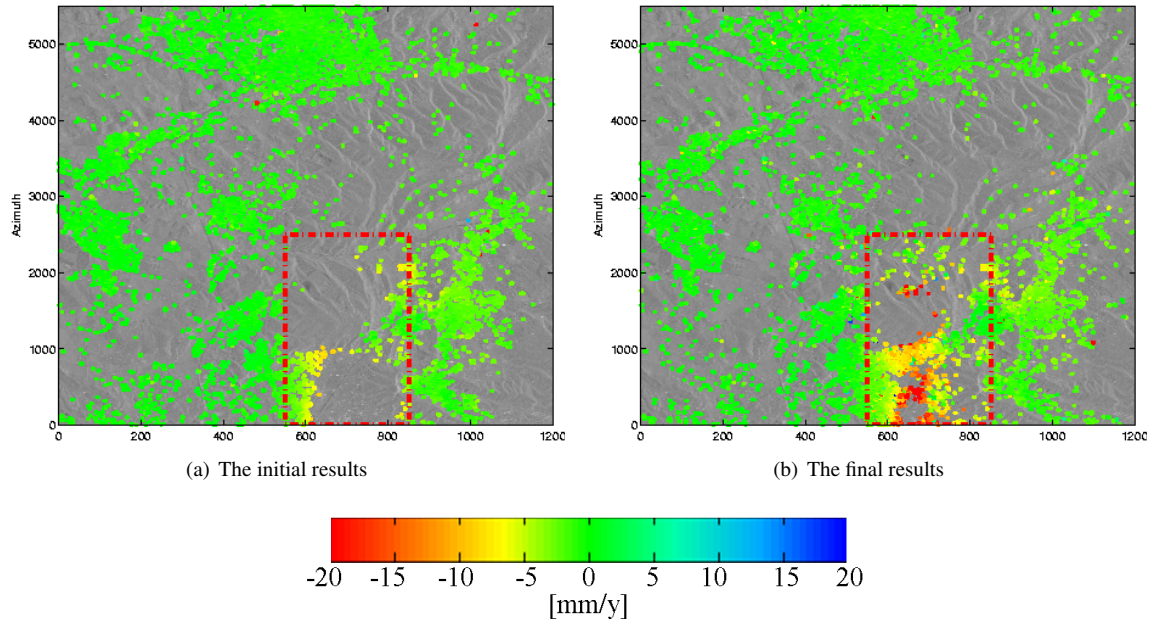
Figure 7.9: *The initial (before improvement) and the final PSI results (after improvement). Linear deformation rates estimated from the unwrapped time series are shown.*

	Initial results	Final results
# **PS in the whole crop**	29115	41171
# **Improvement in the whole crop**	0 %	41 %
# **PS in the deforming area**	2382	8020
# **Improvement in the deforming area**	0 %	236 %
# **detected type-II errors**	1197 (4%)	5547 (13%)

Table 7.2: *Comparison of the PS density and number of type-II errors between the initial and the final results.*

of spatio-temporal profiles of both results with leveling (Fig. 7.12) reveals that despite the better capturing of the deformation signal, there are the discrepancies between the deformation time series which were obtained from the final PSI results and the ones obtained from leveling. The main reason for this inconsistency is unwrapping errors.

7.5   Discussions

7.5.1   On the selection of 1st order PS candidates

In the conventional PSI approach the 1st order PS candidates (PS1c) are selected based on their amplitude dispersion (Eq. (2.3)) assuming that pixels with smaller amplitude dispersion index are expected to have a smaller phase standard deviation. A common value for the amplitude dispersion threshold is within the range $0.2 - 0.25$ for PS1c. However in our case study, we showed that using a value of 0.25 causes to have no PS1 in the deforming areas. With optimizing the PS1c selection algorithm to have at least one candidate per each grid cell, we saw that the density of the 1st order PS (PS1) is increased significantly, leading to better estimation of the APS signal and also higher density of the 2nd order PS. Fig. 7.13 shows the histogram and empirical cumulative distribution function (CDF) of the amplitude dispersion of the PS1 (final 1st order PS which are accepted based on their phase

	S1 area	S2 area	S3 area	S4 area	S5 area
Landscape	Urban/Agriculture	Urban/forest	Urban	Forest/agriculture	Forest
# PS in the initial results	509	2	543	48	17
# PS in the Final results	2466	369	951	117	124
Improvement percentage	384%	18350%	75%	143%	629%
Mean of def. rate (mm/y) - the initial results	-4.5	-6.1	-1.8	-4.6	-2.1
Mean of def. rate (mm/y) - the final results	-6.9	-10.7	-1.7	-4.8	-8
Expected mean of def. rate (mm/y) based on leveling	≈ 10	≈ 10	≈ 6	≈ 10	≥ 10
Maximum def. rate (mm/y) - the initial results	-9.6	-6.1	-5.4	-7.3	-2.8
Maximum def. rate (mm/y) - the final results	-28.7	-27	-19.5	-12.2	-28.8
Expected Maximum def. rate (mm/y) based on leveling	≥ 20	≈ 20	≈ 10	≈ 20	≥ 10

Table 7.3: *Comparison of the PS density and estimated deformation rate between the initial and the final results in different subsidence areas.*

evaluation). We can see that 50% of the accepted PS1 have amplitude dispersion higher than 0.25, and the maximum amplitude dispersion for PS1 is 0.4. The conclusion is that using a low threshold (e.g.,0.25) for the selection of PS1c can lead to a limited number of PS1 and so a poor initial network. This results in the occuring of type-I errors in the evaluation of 2nd order PS candidates. This limitation can be solved by using a higher threshold for the amplitude dispersion or by constraining the algorithm to have at least one PS1c in each grid cell. Also the size of the grid cell is important to have a denser initial network.

7.5.2   On the selection of 2st order PS candidates

In addition to 1st order PS candidates, a set of 2nd order PS candidates (PS2c) is also selected in the PSI processing using a higher amplitude dispersion threshold. These pixels are used in the densification step. The main reason for this selection is to avoid evaluation of all pixels in the densification and so to increase the computational speed. In this study, we decided to process all pixels as PS2c in the area of interest in order to evaluate the main reason of rejection of PS and also to gather statistics about all detected PS and try to comment on a initial selection approach by analyzing these statistics. Fig. 7.14 shows the histogram and the empirical CDF of all accepted PS2 amplitude dispersion in the Gardanne deforming area. We can see that with a threshold of 0.4 and 0.45 we can detect 25% and 55% of all detected PS2, respectively. Fig. 7.15 shows the final PSI results with 0.4 and 0.45 amplitude dispersion threshold in the deforming area. Although the number of PS is decreased significantly from 8020 to 1890 and 3819, the general pattern of the detected deformation signal is the same for all results. One of the reasons can be that we detect also a lot of sidelobes by evaluation all pixels, while the deformation rate of each PS and its sidelobes are the same. The conclusion is that a amplitude disperesion threshold between 0.4 and 0.5 is a reasonable threshold for selecting PS2c. This selection can significantly increase the computational speed. For example in our case study, with the threshold of 0.45, the number of PS2 candidates reduces from 625000 to 27582, resulting in a reduction of the computational time in the densification step by a factor of 20.

7.5.3   On the final selection of PS

In the conventional PSI methods the ensemble coherence is used for quality assessment and final selection of PS. Within the PSI methodology introduced by Kampes (2005), the a-posteriori variance factor is used for final selection of PS. We discussed that both ensemble coherence and a-posteriori variance factor are dependent on the assumed deformation model which is used in the temporal unwrapping step. So they are very sensitive to model imperfection and therefore they are not a good indicator for the observation precision. We showed that the spatio-temporal consistency (STC) can reduce the dependency of the quality assessment to the deformation model.
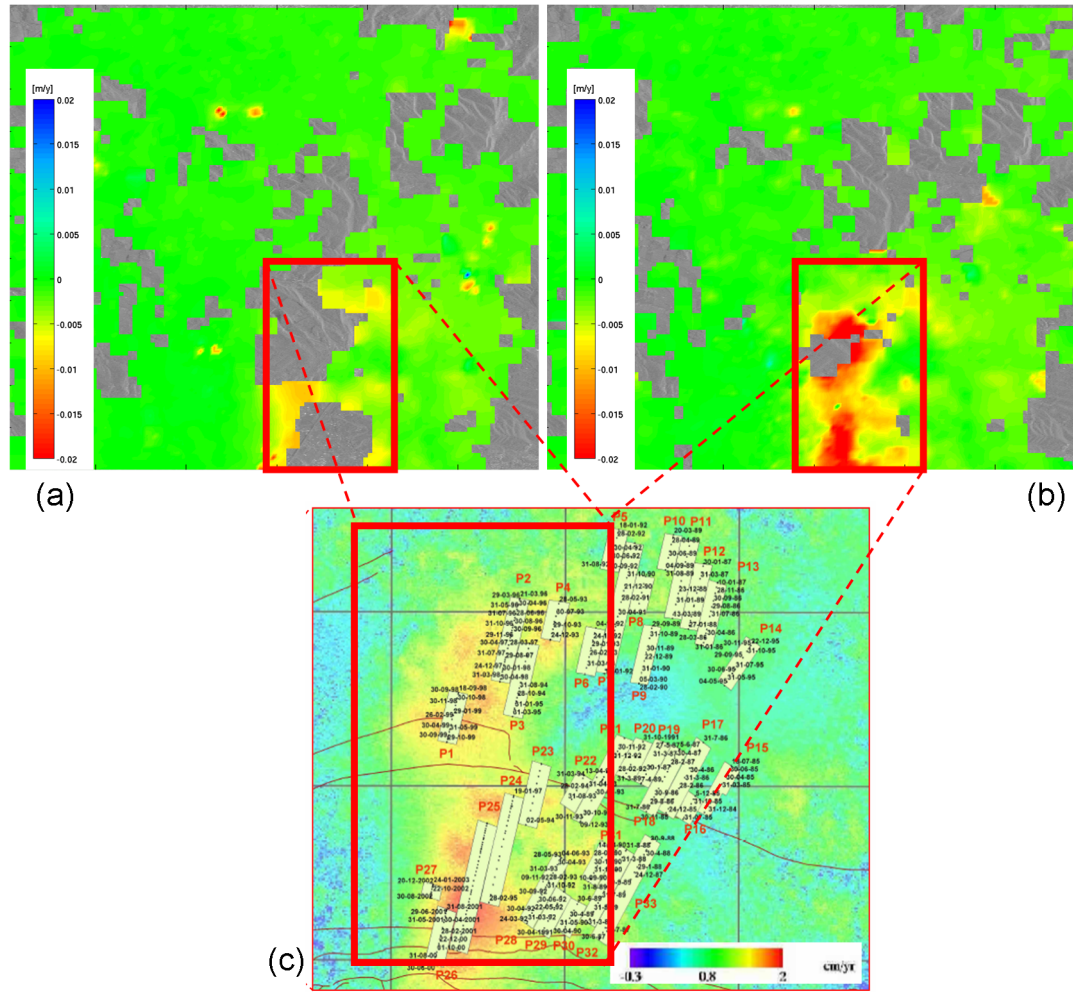
Figure 7.10: *a)Interpolated velocity map using kriging for the initial results , b) Interpolated velocity map using kriging for final results, c) The overlaid mining panels on the differential interferometric data which was obtained by stacking the coherent interferograms between 1995 and 2000 ((Racoules et al., 2006)). The red box is the deforming area. Note the difference in the colorscales.*

However, STC is not appropriate for isolated PS, and so it is not a good quality assessment for applications which try to monitor very local deformations (e.g., individual building deformation monitoring). Empirically we showed that a threshold of $8mm$ is a good indicator for selecting PS candidates as a PS.

Another limitation of all mentioned quality assessment approaches (even STC) is that non of them contains any information about the quality of the estimated ambiguities. So the final selection of PS based on the mentioned quality assessments results in the set of PS which contains unwrapping errors. Although PS with large unwrapping errors which are not consistent in time and space are removed by STC thresholding, other unwrapping errors which are temporally and spatially consistent are included in the final results. The interpretation for unwrapping errors which are spatially consistent are unwrapping errors due to the highly nonlinear deformation mechanism in a particular area (i.e., the fast evolution deformation mechanisms with respect to the radar wavelength). In such an area, all PS are similarly affected by unwrapping errors due to the same localized signal (e.g., nonlinear deformation). We proposed different methods for removing the unwrapping errors in the Section 7.3.1. We saw that the most of the detected PS in the Gardanne deforming area sufferer from unwrapping errors. We think that the main reason is the high nonlinear deformation mechanism in the area. We showed that with the double breakpoint model we can detect a lot of new PS, however due to the limited number of interferograms in some
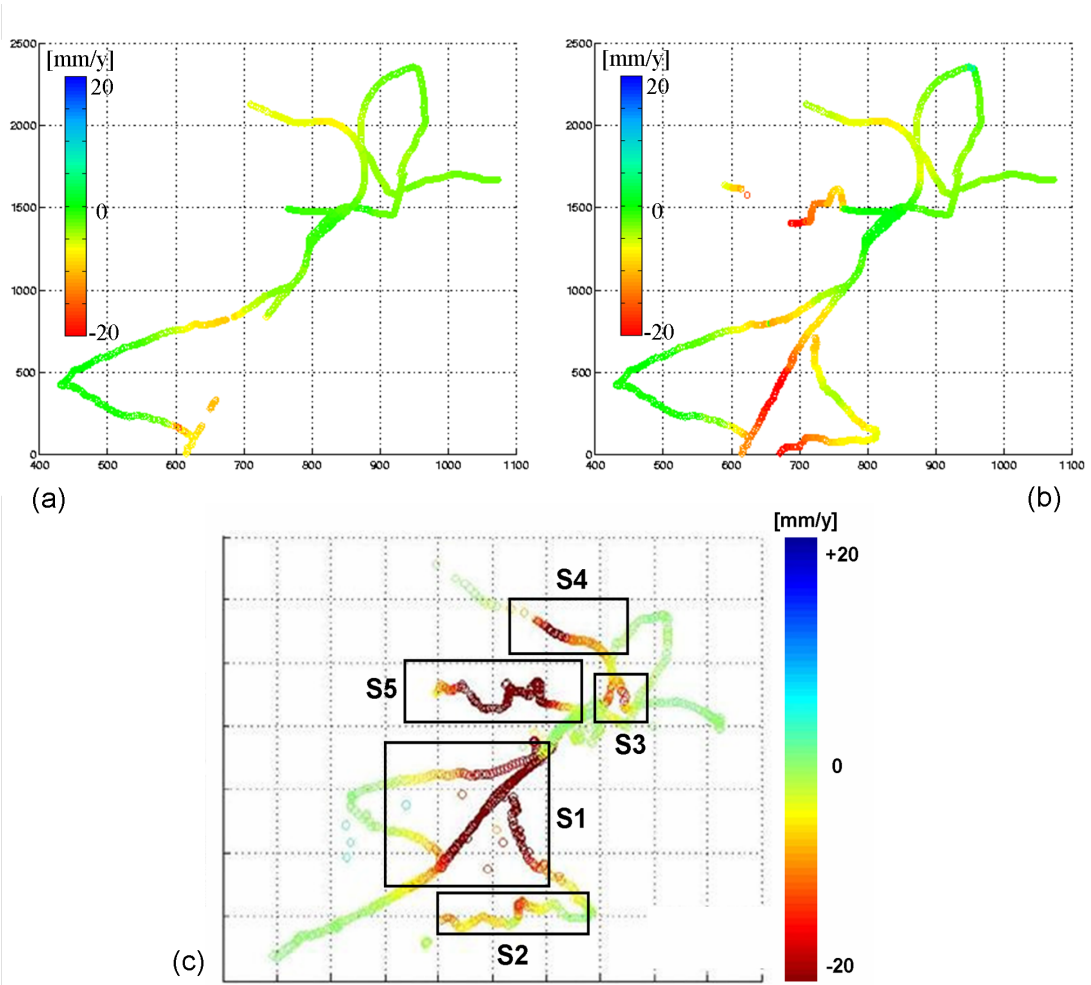
Figure 7.11: *a) Interpolated radar velocity map on the leveling profile location for the initial result , b) Interpolated radar velocity map on the leveling profile location for the final result, c) the annual cumulative deformation obtained from the leveling data((Racoules et al., 2006)), and the location of the five subsidence areas.*

time intervals (e.g., before the first breakpoint), the obtained results includes unwrapping errors. Note that we used the bootstrapping method for the ambiguity estimation because of the time limitation of the project. As we discussed earlier this method is not optimal for ambiguity estimation. It is recommended to apply all the proposed adaptations with the integer least squares method to reduce the number of unwrapping errors.

Finally, the decision for removing the unwrapping errors from final selected PS or relaxing the acceptance condition of the unwrapping errors is dependent to the application of the PSI results. For example, in the applications which only require a detection of a deformation pattern in particular areas, the small unwrapping errors in the results are acceptable. On the other hand, when a detail deformation time series is required, final PSI results need more post processing to analyze the possible unwrapping errors or removing them. In this study, we kept the unwrapping errors in the final results. We conclude that in the Gardanne deforming area, the main limitation of our PSI methodology is in coping with the unwrapping errors. This reveals the requirement of better quality assessment of PS with a quality indicator for estimated ambiguities, and a post-processing algorithm for analyzing and adapting the unwrapping errors.
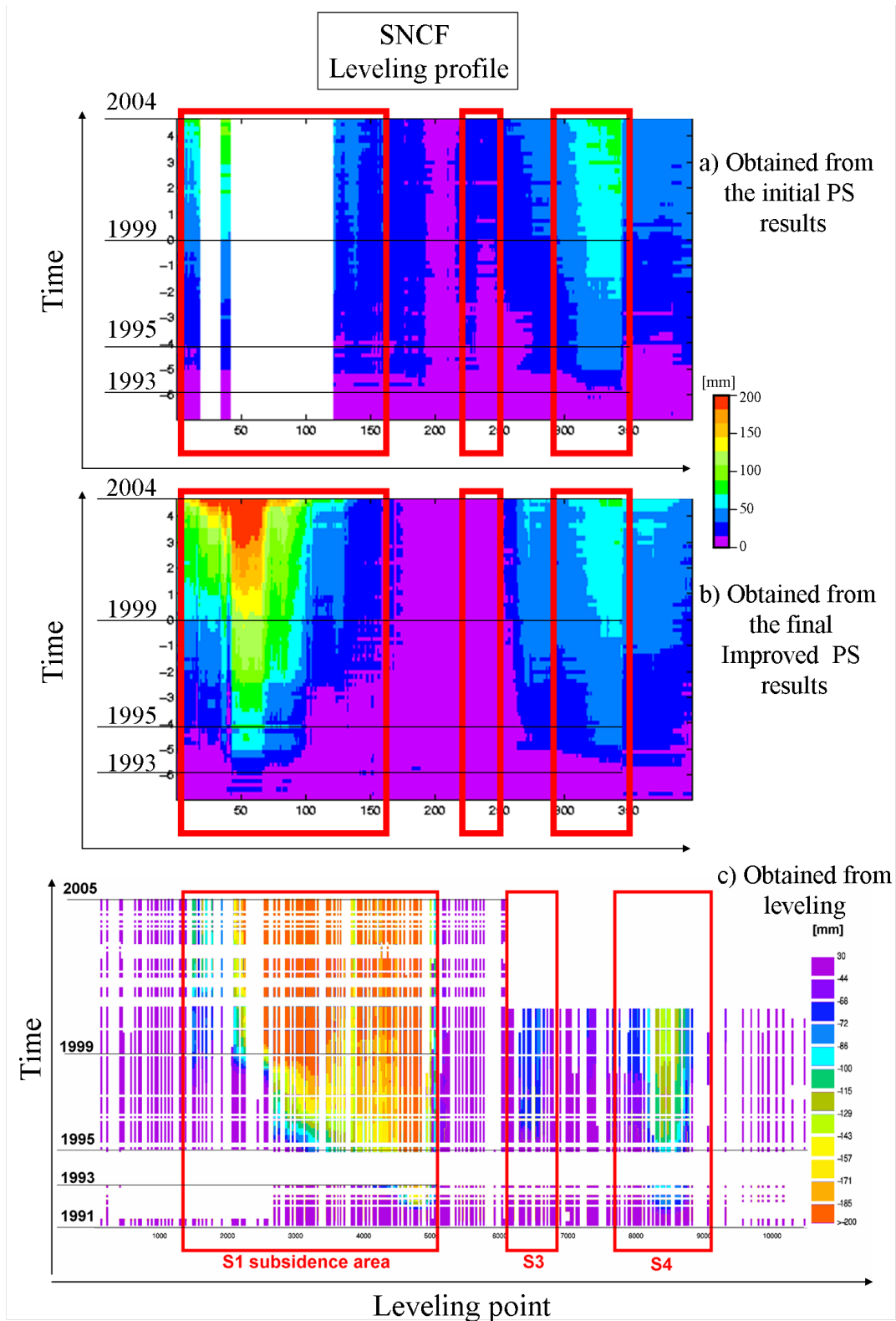
Figure 7.12: *a) Spatio-temporal profile of the SNCF leveling profile obtained form the initial PSI results, b)Spatio-temporal profile of the SNCF leveling profile obtained form the final PSI results, c) Spatio-temporal profile of the SNCF leveling profile obtained from the leveling data ((Racoules et al., 2006)). Cumulative displacement in mm; horizontal lower axis: distance in m; vertical axis: time; Red boxes are the section corresponding to the subsidence areas.(Note the difference in the colorscales).*
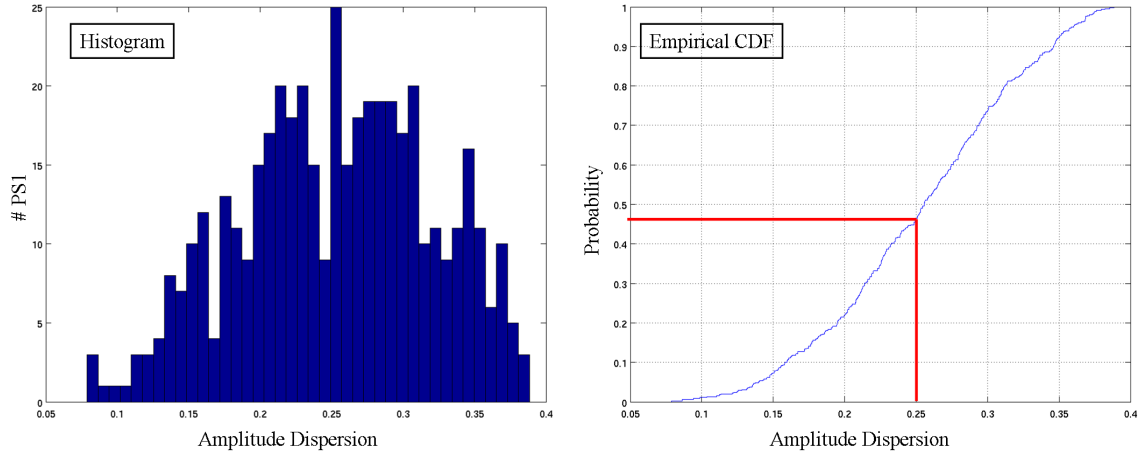
Figure 7.13: The histogram and empirical CDF for the amplitude dispersion of the accepted PS1
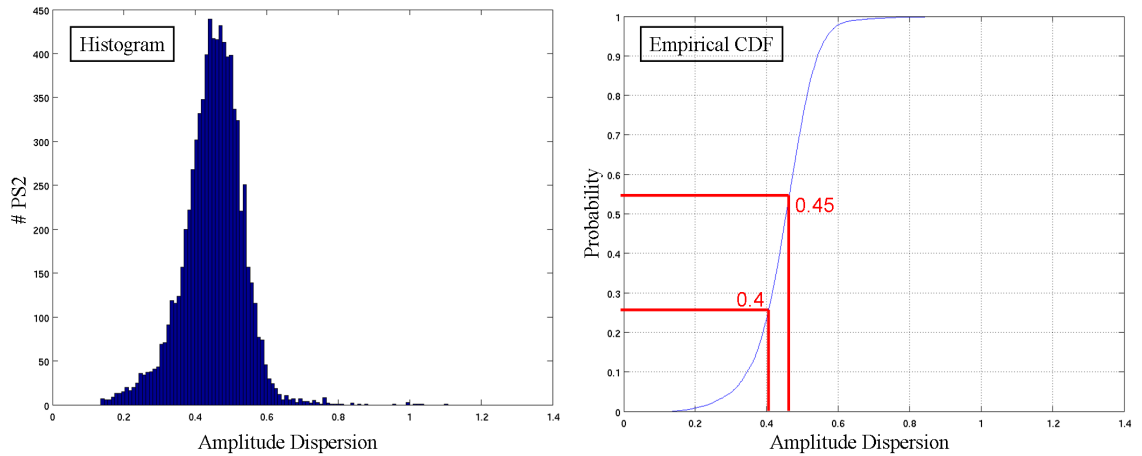
Figure 7.14: The histogram and empirical CDF for the amplitude dispersion of the accepted PS2

7.5.4 On the synergy effect among different optimizations

The density of PS in the final PSI results improved by the combination of different optimizations: 1) optimized initial network, 2) optimized APS estimation, 3) adaptive deformation models, and 4) adapted mathematical model for an azimuthal subpixel position. Fig. 7.16 presents the contribution of the different adaptations in the PS density in the Gardanne deforming area. We can see that the sum of the four contributions (248%) is not equal to the total improvement (236%). The main reason is that there are common detected PS detected by different optimizations. For example, 78% of newly detected PS by the subpixel position adaptation, are accepted also by improving in the APS estimation. On the other hand, there is also a synergy effect between some optimizations. For example, the proposed method for detection of pixels with azimuthal subpixel position is based on the assumption of the correct deformation model. So with a more feasible deformation model, the proposed method for dealing with a PS subpixel position has more influence on the final PS density. For example, using the adapted method for a subpixel position together with the linear deformation model increases the PS density for 9%, however with the double breakpoint model, it results in 12% improvement. So there are both synergy and reciprocal effect among the proposed optimizations.

(a) AD ≤ 0.40   (b) AD ≤ 0.45
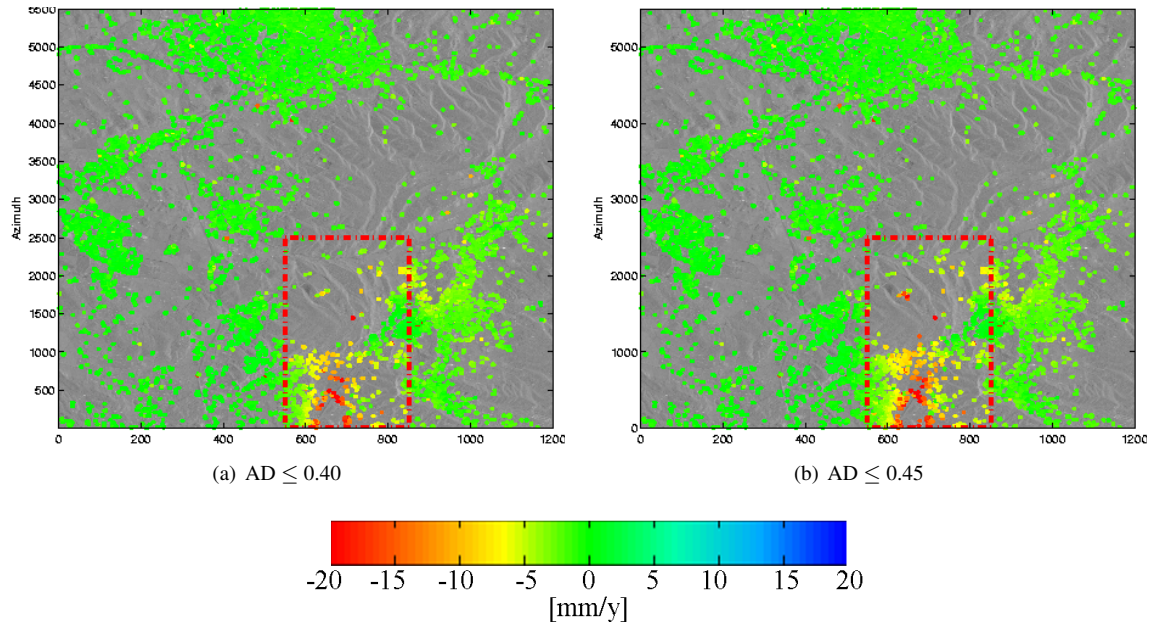
Figure 7.15: *The final results using different amplitude dispersion threshold in the deforming area. a) Amplitude dispersion threshold of* 0.4 *(*$\#PS = 1890$*) , and b) Amplitude dispersion threshold of* 0.45 *(*$\#PS = 3819$*)*
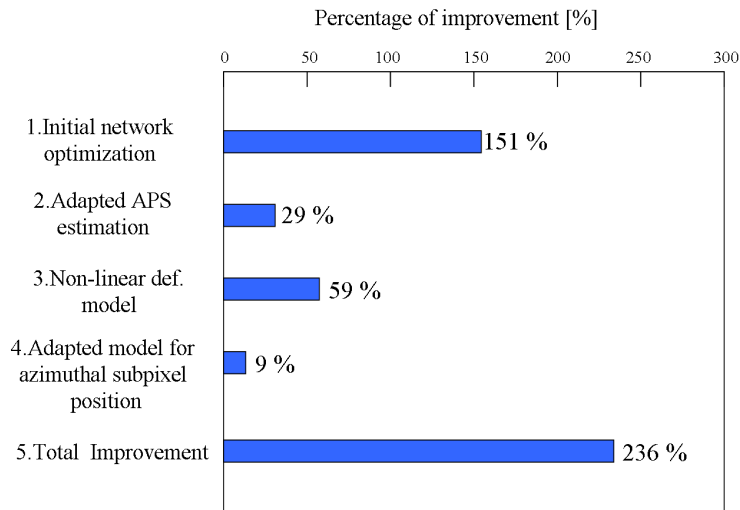
Figure 7.16: *Contribution of different adaptations in the PSI processing. Improvements are with respect to the initial results (the results before applying the adaptations).*

Chapter 8

Conclusions and Recommendations

The central research question of this study is: "How can the density of persistent scatterers be improved by optimizing the PSI densification algorithm?" In this chapter, we present the main conclusions of this research, followed by recommendations for further studies.

8.1   Conclusions

The results of the PSIC4 study have been used to evaluate the PSI algorithm performance and assess which approaches are most important to retrieve reliable deformation parameters at a high spatial density. We investigated the contribution of four factors and proposed new approaches to improve the PS density. These optimizations are: 1) initial network optimization, 2) adapted APS estimation with trend and stratification estimation, 3) non-linear deformation modeling , and 4)adapted mathematical model for PS with an azimuthal subpixel position. The percentage of improvement in the PS density in the deforming area by each optimization is summarized in Table. 8.1.

Optimization	Percentage of improvement
initial network optimization	151%
adapted APS estimation	29%
Non-linear deformation modeling	59%
adapted model for azimuthal subpixel position	9%
Applying all optimizations together	236%

Table 8.1: *Contribution of each proposed optimization in the final PS density improvement.*

The improvement percentages can be interpreted as the amount of influence of each optimization on false rejection of PS (type-I errors). The improved results present the improvement in capturing the deformation signal of all the subsidence areas (Figs. 7.10 and 7.11). However, the results of the study show that most of the newly detected PS in the deforming area suffer from the incorrect estimation of the ambiguities (unwrapping errors). Consequently, the estimated deformations per epoch (or deformation time series) are not very reliable. We can see the effect of the unwrapping errors as the significant discrepancies between the final deformation time series of the Gardanne case study and the leveling data (see Fig. 7.12). The main reason for this localized effect (as they occur mostly in the deforming area) is the fast evolution of the deformation mechanism in the Gardanne mining area. According to the leveling data (Racoules et al., 2006), the deformations range from few centimeters up to some decimeters occurred in few months. These deformations are strong "fast deformation" for the view point of C-band radar (with wavelength of 5.6 cm) with at most monthly acquisition of ERS data. In addition to the unwrapping errors, even after applying the proposed optimizations, there is still a limited number of PS in the north part of the Gardanne

deforming area due to the fact that this area has the totally non-urbanized landscape and therefore it is affected by the temporal decorrelation. The conclusions related to each proposed optimization are provided in this section based on the items which are already defined in Section 1.2.

Initial network optimization. Using the amplitude dispersion threshold of 0.25 for selecting 1st order PS candidates results in an initial network which contains a limited number of PS in the Gardanne deforming area. The optimization of the initial selection of 1st order PS candidates (PS1c) by constraining the algorithm to have at least one PS1c in each grid cell results in the denser network especially in the deforming area. This optimization leads to the significant improvement (151%) in the PS density. Moreover the quality of the APS estimation is improved by using a denser initial network. The main improvement in the final PS density is for the areas in which we can detect new PS1 in the initial network. Moreover, the area which still has a low number of PS are areas in which there are no PS1 in the initial network. This direct relation between the density of PS1 and PS2 show the vital influence of the 1st order PS detection on the density of the final set of PS.

Atmospheric phase screen estimation. The new APS estimation approach including trend, turbulence, and vertical stratification estimation was applied to the Gardanne dataset. The results show the better performance of the new approach than the conventional approach. Both tandem pair validation and PSI results confirm the improvement in the APS estimation. The rms of differences between the estimated APS and the tandem interferograms improved from 1.39 to 0.94 radians, comparable of 2 mm improvement in APS estimation precision. With the optimized initial network, the rms value reduces to 0.89 radians, that is 4 mm in term of deformation. Application of the proposed optimizations in the APS estimation shows the 39% increase in the number of detected PS in the deforming area, leading to better estimation of the deformation field.

The new method for estimation of the vertical stratification signal was presented. Application of the proposed method on the Gardanne dataset shows that the estimated stratification signal in this area is not significant (or not captured properly). Both tandem pair validation and PSI results show comparable results for APS estimation with and without the stratification estimation. The potential causes for this effect can be summarized as:

1. The stratification signal may be not significant or may has low signal to noise ratio. The unwrapped phases which are used for the stratification estimation include the APS effect and also the noise. If the amount of noise is very higher than the stratification effect, the proposed method may not capture this signal due to its low signal to noise ratio.

2. The level of details of the used DEM for stratification estimation is very low. We used the SRTM DEM with the 30 m horizontal resolution and about 5 m height standard deviation. This DEM is also very smooth, so the nearby pixels have approximately the comparable height. Using this DEM for the stratification estimation may not capture the small height variation between nearby PS1.

3. The vertical stratification signal has a seasonal behavior (Hanssen, 2001) and so correlation in the time domain. As the APS estimation step is applied after the temporal filtering of the unwrapped phase measurements, some part of the stratification signal can leak to the temporally correlated signal (i.e., unmodeled deformation). Therefore, the filtered phases which are used as observation for the estimation may not contain the full stratification signal.

PS subpixel position. The new method for detection of pixels with large azimuthal subpixel position was presented. It was shown that pixels with large azimuthal subpixel position effect can be detected by evaluating the correlation between their residuals and Doppler baselines. The result of simulation shows that thresholding on this correlation can effectively detect point scatterers with the large subpixel position. The proposed detection method assumes the correct estimation of ambiguities. Therefore, in areas where the assumed deformation model is not valid (e.g., areas with high non-linear deformation mechanism), and so the chance of unwrapping errors is higher, the performance of the detection method is limited.

Three different methods were proposed to deal with the azimuthal subpixel position of PS. Applying these methods on the Gardanne dataset revealed that it is better to deal with an azimuthal subpixel position stochastically rather than functionally. The reason that functional estimation of the subpixel position does not influence the PSI results significantly can be due to the low variability of Doppler baselines. Adaptation of

the stochastic model for pixels with large azimuthal subpixel positions results in 9% improvement in the PS density in the Gardanne deforming area.

Non-linear deformation model. The sequential hypothesis testing methodology with adaptive deformation models was introduced and applied on the Gardanne dataset. The proposed method showed to be an effective and resulted in an increase in the number of detected PS from 2380 to 4352, that is 83% improvement in the PS density. Especially the double breakpoint model shows effective capability in detection of PS in the Gardanne data set, as the deformation mechanism of the main subsidence area can be characterized by two breakpoint (start and end time of the mining activities). This improvement in the PS density significantly improved the results in capturing the deformation signal in all subsidence areas. However, the results using adaptive deformation models are more affected by unwrapping errors because the main subsidence took place in a relatively short time span. (35% of consecutive SAR acquisitions in the used dataset contains deformation larger than 2.8cm and 70% has deformation larger than 1.4cm (Racoules et al., 2006).). Even with the double breakpoint model, the obtained results are affected by unwrapping errors, especially due to the limited number of interferograms in some time intervals (e.g., before the first breakpoint). Note that we used the bootstrapping method for the ambiguity estimation because of the time limitation of the project. As we discussed earlier this method is not optimal for the ambiguity estimation. It is recommended to apply all the proposed adaptations with the integer least square method which has better success rate for estimation of the ambiguities.

Final selection of PS. Spatio-temporal consistency (STC) was introduced as a quality assessment for the final selection of PS. It was shown that using STC for final selection of PS (with STC threshold of 8 mm) can effectively remove type-II errors. The advantage of using STC is that it can reduce the dependency of the quality assessment to the assumed deformation model and therefore it is better indicator for the observations precision. However STC is not appropriate for isolated PS, and so it is not good quality assessment in applications which try to monitor localized deformations (e.g., individual building deformation monitoring).

Despite the successful application of STC, it does not include any information about the quality of the estimated ambiguities (the same as a-posteriori variance factor and the ensemble coherence). So the final set of PS selected by STC is affected by unwrapping errors. Different methods with restricted or relaxed conditions for removing the unwrapping errors were presented in the Chapter 7. We saw most of the detected PS in the Gardanne deforming area sufferer from unwrapping errors. As discussed earlier the main reason for these errors is the fast evolution of the deformation mechanism with respect to the C-band radar wavelength. The decision for removing the unwrapping errors from final selected PS or relaxing the acceptance condition of the unwrapping errors is dependent to the application of the PSI results. However, in order to deliver PSI results including unwrapping errors to the end users, a PS quality description which contains the quality of the estimated ambiguities is required.

8.2 Recommendations for further studies

In this section a few topics for further study are outlined to improve the optimizations which were proposed in this study and to extend the derived conclusions.

- All optimizations which are presented were only evaluated on the Gardanne dataset. For better validation of these methods, it is recommended to assess and verify their performance on the other datasets too.

- The proposed methods for dealing with non-linear deformations and the azimuthal subpixel position effect were only applied in the densification step, that is they are applied only for 2nd order PS candidates. It is expected that these optimization can also improve the temporal unwrapping and parameter estimation of the 1st order PS, leading to improvement in the initial network of PS1. As we showed in the study, the quality of the initial network has significant influence on the quality of the final results. We recommend applying the proposed methods also in temporal unwrapping of 1st order PS.

- We saw that the final PS results in the Gardanne area were affected significantly by the unwrapping errors. Due to the time limitation in this project, we used only the bootstrapping method which is not optimal for ambiguity estimation. It is expected that applying the integer least square method can improve the results in terms of the amount of the unwrapping errors. It is recommended to apply all proposed optimizations with the integer least squares technique.

- As discussed in the conclusions, there is a requirement for the PS quality assessment method which comprises a quality of estimated ambiguities. There is a need for further studies about how it is possible to include a quality of estimated ambiguities in the final quality assessment of PSI results.

- This study was limited to use only the single master approach. However there are useful information on the other interferograms of the dataset especially in coherent interferograms. An example is the DInSAR result (Fig. 3.2) which was used for the validation purpose in our study. It needs more study about how we can include this extra information in our mathematical model.

- The proposed approach for estimation of the vertical stratification, is based on the deterministic estimation using the linear function between PS1 heights and their unwrapped phases. We discussed that the resolution and height precision of the SRTM DEM (which was used in this study) may not sufficient to estimate the stratification signal. It is recommended to apply the proposed method in another dataset with available fine resolution DEM and to evaluate the performance of the method. Also a more stochastic approach for the stratification estimation may be effective. For example, we propose to apply the co-kriging method for stratification estimation using the unwrapped phases as observations and the heights as co-observations. The cross-covariance function between heights and phases should be used in the co-kriging system. In this way, the estimation is not only based on the deterministic relation between heights and unwrapped phases but also based on the stochastic characteristics of these (co)observations. (e.g., correlation between heights and phase measurements).

- we proposed the new method in Chapter 5 for detection of the PS with an azimuthal subpixel position. The method was validated based on the simulated data. The validation of the proposed detection approach needs further research. It is recommended to perform point target analysis for detected pixels in amplitude domain in order to estimate their actual azimuthal subpixel position and evaluate the performance of the method.

- In Chapter 5, we proposed the method for adaptation of the covariance matrix of the observations with a large azimuthal subpixel position. This adaptation is based on the deterministic relation between Doppler baselines and residuals. On the other hand, we already used the variance component estimation (VCE) for defining the covariance matrix. We recommend to perform VCE on the phase measurements of the detected pixels with an azimuthal subpixel position in order to estimate the adapted covariance matrix. This approach needs an extra co-factor matrix which accounts for the subpixel position effect.

- The sequential hypothesis testing using the double breakpoint model shows effective performance in the Gardanne dataset. The drawback of this deformation model is that it needs a-priori knowledge about the time of the breakpoints. The polynomial deformation model with degree of 3 (Cubic model) seems to be a good alternative for the double breakpoint model (see Fig. 6.2 and compare the shape of the double breakpoint model and the cubic model). The advantage of using the cubic model is that it does not need the knowledge about the breakpoint time. It is recommended to use this model in the framework of the sequential hypothesis testing on the Gardanne dataset.

Appendix A

Used SAR data

ERS	Date	orbit	Bperp[m]	Btemp[days]	Abs. Doppler diff.[Hz]
2	20-Mar-99	20460	0	0	0
1	6-May-92	4218	-67	-2509	120
1	10-Jun-92	4719	187	-2474	157
1	15-Jul-92	5220	-311	-2439	174
1	19-Aug-92	5721	-229	-2404	138
1	23-Sep-92	6222	-157	-2369	142
1	28-Oct-92	6723	499	-2334	123
1	2-Dec-92	7224	302	-2299	151
1	6-Jan-93	7725	-835	-2264	137
1	17-Mar-93	8727	267	-2194	128
1	21-Apr-93	9228	564	-2159	149
1	30-Jun-93	10230	-464	-2089	140
1	17-Nov-93	12234	515	-1949	102
1	14-Apr-95	19592	-234	-1436	124
1	19-May-95	20093	-334	-1401	156
1	1-Sep-95	21596	-258	-1296	154
2	2-Sep-95	1923	-320	-1295	132
1	6-Oct-95	22097	266	-1261	113
2	7-Oct-95	2424	754	-1260	166
1	10-Nov-95	22598	317	-1226	111
1	15-Dec-95	23099	534	-1191	119
1	19-Jan-96	23600	-432	-1156	81
2	24-Feb-96	4428	765	-1120	140

ERS	Date	orbit	Bperp[m]	Btemp[days]	Abs. Doppler diff.[Hz]
1	29-Mar-96	24602	-610	-1086	139
2	30-Mar-96	4929	-715	-1085	97
1	3-May-96	25103	662	-1051	119
2	4-May-96	5430	583	-1050	125
2	8-Jun-96	5931	-750	-1015	108
2	17-Aug-96	6933	-276	-945	139
2	26-Oct-96	7935	728	-875	157
2	30-Nov-96	8436	842	-840	128
2	4-Jan-97	8937	-179	-805	81
2	8-Feb-97	9438	272	-770	129
2	15-Mar-97	9939	-51	-735	123
2	19-Apr-97	10440	455	-700	117
2	24-May-97	10941	-163	-665	105
1	1-Aug-97	31616	-340	-596	111
2	2-Aug-97	11943	-150	-595	129
2	6-Sep-97	12444	369	-560	115
2	11-Oct-97	12945	278	-525	131
2	15-Nov-97	13446	-69	-490	150
2	20-Dec-97	13947	-91	-455	73
2	24-Jan-98	14448	-382	-420	126
2	28-Feb-98	14949	-993	-385	136
2	4-Apr-98	15450	-496	-350	125
2	9-May-98	15951	498	-315	69
2	13-Jun-98	16452	803	-280	88
2	18-Jul-98	16953	-895	-245	66
2	22-Aug-98	17454	-544	-210	83
2	26-Sep-98	17955	452	-175	127
2	31-Oct-98	18456	687	-140	119
2	5-Dec-98	18957	-464	-105	100
2	9-Jan-99	19458	-1128	-70	76
1	19-Mar-99	40133	40	-1	194
2	24-Apr-99	20961	-202	35	90
1	28-May-99	41135	614	69	189
2	29-May-99	21462	550	70	81
1	2-Jul-99	41636	-63	104	159
2	3-Jul-99	21963	-107	105	87
2	7-Aug-99	22464	486	140	148
2	11-Sep-99	22965	-785	175	118
2	16-Oct-99	23466	-296	210	135

ERS	Date	orbit	Bperp[m]	Btemp[days]	Abs. Doppler diff.[Hz]
2	20-Nov-99	23967	-465	245	118
2	25-Dec-99	24468	128	280	61
1	28-Jan-00	44642	-271	314	147
2	29-Jan-00	24969	-127	315	107
1	4-Nov-00	28977	-63	595	422
2	9-Dec-00	29478	-723	630	279
2	13-Jan-01	29979	208	665	103
2	7-Jul-01	32484	252	840	120
2	15-Sep-01	33486	271	910	35
2	9-Nov-02	39498	676	1330	172
2	25-Oct-03	44508	172	1680	164

Bibliography

Adam, N., B. M. Kampes, and M. Eineder (2004). The development of a scientific persistent scatterer system: Modifications for mixed ERS/ENVISAT time series. In *ENVISAT & ERS Symposium, Salzburg, Austria, 6–10 September, 2004*, pp. 9.

Amelung, F., D. L. Galloway, J. W. Bell, H. A. Zebker, and R. J. Laczniak (1999, June). Sensing the ups and downs of Las Vegas: InSAR reveals structural control of land subsidence and aquifer-system deformation. *Geology 27*(6), 483–486.

Amelung, F., S. Jónsson, H. Zebker, and P. Segall (2000, October-26). Widespread uplift and trap door faulting on Galápagos volcanoes observed with radar interferometry. *Nature 407*(6807), 993–996.

Bamler, R. and P. Hartl (1998). Synthetic aperture radar interferometry. *Inverse Problems 14*, R1–R54.

Bamler, R. and D. Just (1993). Phase statistics and decorrelation in SAR interferograms. In *International Geoscience and Remote Sensing Symposium, Tokyo, Japan, 18–21 August 1993*, pp. 980–984.

Counselman, C. C. and S. A. Gourevitch (1981). Miniature interferometer terminals for earth surveying: ambiguity and multipath with the Global Positioning System. *IEEE Transactions on Geoscience and Remote Sensing 19*(4), 244–252.

Ferretti, A., F. Morali, E. Passera, and F. rocca (2005). Statistical analysis of atmospheric components in ERS SAR data. In *Fourth International Workshop on ERS/Envisat SAR Interferometry, 'FRINGE05', Frascati, Italy, 28 Nov-2 Dec 2005*, pp. presentation.

Ferretti, A., C. Prati, and F. Rocca (2000, September). Nonlinear subsidence rate estimation using permanent scatterers in differential SAR interferometry. *IEEE Transactions on Geoscience and Remote Sensing 38*(5), 2202–2212.

Ferretti, A., C. Prati, and F. Rocca (2001, January). Permanent scatterers in SAR interferometry. *IEEE Transactions on Geoscience and Remote Sensing 39*(1), 8–20.

Gatelli, F., A. Monti Guarnieri, F. Parizzi, P. Pasquali, C. Prati, and F. Rocca (1994, July). The wavenumber shift in SAR interferometry. *IEEE Transactions on Geoscience and Remote Sensing 32*(4), 855–865.

Hanssen, R. (2004). Stochastic modeling of time series radar interferometry. In *International Geoscience and Remote Sensing Symposium, Anchorage, Alaska, 20–24 September 2004*, pp. cdrom, 4 pages.

Hanssen, R., F. Amelung, and H. Zebker (1998, November-10). Geodetic interpretation of land subsidence measurements at the Cerro Prieto geothermal field monitored by radar interferometry. *EOS Transactions, AGU 79*(45), F37.

Hanssen, R., B. Vermeersen, R. Scharroo, B. Kampes, S. Usai, R. Gens, and R. Klees (2000, February). Deformatiepatroon van de aardbeving van 17 augustus 1999 in Turkije gemeten met satelliet radar interferometrie. *Remote Sensing Nieuwsbrief 90*, 42–44. In Dutch.

Hanssen, R. F. (2001). *Radar Interferometry: Data Interpretation and Error Analysis*. Dordrecht: Kluwer Academic Publishers.

Hanssen, R. F. (2003). Subsidence monitoring using contiguous and PS-InSAR: Quality assessment based on precision and reliability. In 11th *FIG International Symposium on Deformation Measurements, Santorini, Greece, 23–28 May, 2003*, pp. cdrom, p.8.

Hanssen, R. F., F. van Leijen, G. Ketelaar, P. S. Marinkovic, and S. Gehlot (2005, February). PSIC4: PSI-processing over a validation test site. applicability report. Technical report, Delft University of Technology, Delft. European Space Agency Study report ESA Contract Nr. 18707/04/I-LG.

Hanssen, R. F., F. J. van Leijen, G. J. van Zwieten, S. Dortland, C. N. Bremmer, and M. Kleuskens (2008). Validation of PSI results of Alkmaar and Amsterdam within the Terrafirma validation experiment. In *Fifth*

International Workshop on ERS/Envisat SAR Interferometry, 'FRINGE07', Frascati, Italy, 26 Nov-30 Nov 2007, pp. 6 pp.

Hooper, A. (2006). *Persistent Scatterer Radar Interferometry for Crustal Deformation Studies and Modeling of Volcanic Deformation*. Ph. D. thesis, Stanford University.

Hooper, A., H. Zebker, P. Segall, and B. Kampes (2004, December). A new method for measuring deformation on volcanoes and other non-urban areas using InSAR persistent scatterers. *Geophysical Research Letters 31*, L23611, doi:10.1029/2004GL021737.

Humme, A. (2007, December). Point density optimization for SAR interferometry; a study tested on salt mine areas. Master's thesis, Delft University of Technology.

Joughin, I. R. (1995). *Estimation of Ice-Sheet Topography and Motion Using Interferometric Synthetic Aperture Radar*. Ph. D. thesis, University of Washington.

Kampes, B. and S. Usai (1999). Doris: the Delft Object-oriented Radar Interferometric Software. In *2nd International Symposium on Operationalization of Remote Sensing, Enschede, The Netherlands, 16–20 August, 1999*.

Kampes, B. M. (2005, September). *Displacement Parameter Estimation using Permanent Scatterer Interferometry*. Ph. D. thesis, Delft University of Technology, Delft, the Netherlands.

Kampes, B. M. and N. Adam (2003). Velocity field retrieval from long term coherent points in radar interferometric stacks. In *International Geoscience and Remote Sensing Symposium, Toulouse, France, 21–25 July 2003*, pp. cdrom, 4 pages.

Kampes, B. M. and R. F. Hanssen (2004, November). Ambiguity resolution for permanent scatterer interferometry. *IEEE Transactions on Geoscience and Remote Sensing 42*(11), 2446–2453.

Ketelaar, G., F. van Leijen, P. Marinkovic, and R. Hanssen (2005). Initial point selection and validation in PS-InSAR using integrated amplitude calibration. In *International Geoscience and Remote Sensing Symposium, Seoul, Korea, 25–29 July 2005*, pp. 5490–5493.

Laur, H., P. Bally, P. Meadows, J. Sanchez, B. Schaettler, E. Lopinto, and D. Esteban (2002, September). Derivation of the backscattering coefficient σ^0 in ESA ERS SAR PRI products. Technical Report ES-TN-RS-PM-HL09, ESA. Issue 2, Rev. 5d.

Marinkovic, P., G. Ketelaar, F. van Leijen, and R. Hanssen (2008). InSAR quality control: Analysis of five years of corner reflector time series. In *Fifth International Workshop on ERS/Envisat SAR Interferometry, 'FRINGE07', Frascati, Italy, 26 Nov-30 Nov 2007*, pp. 8 pp.

Massonnet, D. and K. L. Feigl (1998, November). Radar interferometry and its application to changes in the earth's surface. *Reviews of Geophysics 36*(4), 441–500.

Massonnet, D., M. Rossi, C. Carmona, F. Adagna, G. Peltzer, K. Feigl, and T. Rabaute (1993, July-8). The displacement field of the Landers earthquake mapped by radar interferometry. *Nature 364*(8), 138–142.

Massonnet, D. and H. Vadon (1995, March). ERS-1 internal clock drift measured by interferometry. *IEEE Transactions on Geoscience and Remote Sensing 33*(2), 401–408.

Meyer, F. (2004, January). *Simultane Schaetzung von Topographie und Dynamik polarer Gletscher aus multi-temporalen SAR Interferogrammen*. Ph. D. thesis, Munich University of Technology, Munich.

Racoules, D., B. Bourgine, M. de Michele, G. L. Cozannet, C. Luc, C. Bremmer, H. Veldkamp, D. Tragheim, L. Bateson, M. Crosetto, M. Agudo, and M. Engdahl (2006, June). Psic4: Persistent scatterer interferometry – independent validation and intercomparison of results. Technical report, BRGM. BRGM/RP-55640-FR.

Rosen, P., S. Hensley, I. R. Joughin, F. K. Li, S. Madsen, E. Rodríguez, and R. Goldstein (2000, March). Synthetic aperture radar interferometry. *Proceedings of the IEEE 88*(3), 333–382.

Sandwell, D. T. and E. J. Price (1998, December). Phase gradient approach to stacking interferograms. *Journal of Geophysical Research 103*(B12), 30183–30204.

Sandwell, D. T. and L. Sichoix (2000). Topographic phase recovery from stacked ERS interferometry and a low resolution digital elevation model. *Journal of Geophysical Research 105*(B12), 28211–28222.

Shimoni, M., F. van der Meer, R. F. Hanssen, E. Ben-Dor, and B. M. Kampes (2002). Monitoring of salt diapir movements using SAR interferometry. *International Journal of Remote Sensing submitted*.

Teunissen, P. J. G. (1993). Least-squares estimation of the integer GPS ambiguities. In *Invited Lecture, Section IV Theory and Methodology, IAG General Meeting, Beijing, China, august 1993*. Also in: Delft Geodetic Computing Centre, LGR Series, No. 6, 1994.

Teunissen, P. J. G. (1998). Success probability of integer GPS ambiguity rounding and bootstrapping. *Journal of Geodesy 72*, 606–612.

Teunissen, P. J. G. (1999). An optimality property of the integer least-squares estimator. *Journal of Geodesy 73*, 587–593.

Teunissen, P. J. G. (2001). GNSS ambiguity bootstrapping: Theory and application. In *International Symposium on Kinematic Systems in Geodesy, Geomatics and Navigation, Banff, Canada, 5–8 June 2001*.

Teunissen, P. J. G., P. J. de Jonge, and C. C. J. M. Tiberius (1995, April). A new way to fix carrier-phase ambiguities. *GPS World*, 58–61.

Teunissen, P. J. G., D. G. Simons, and C. C. J. M. Tiberius (2005). *Probability and observation theory*. Delft Institute of Earth Observation and Space Systems (DEOS), Delft University of Technology, The Netherlands.

Usai, S. (1997). The use of man-made features for long time scale insar. In *International Geoscience and Remote Sensing Symposium, Singapore, 3–8 Aug 1997*, pp. 1542–1544.

Usai, S. and R. Hanssen (1997). Long time scale INSAR by means of high coherence features. In *Third ERS Symposium—Space at the Service of our Environment, Florence, Italy, 17–21 March 1997*, pp. 225–228.

van Leijen, F. J. and R. F. Hanssen (2007). Persistent scatterer interferometry using adaptive deformation models. In *ESA ENVISAT Symposium, Montreux, Switzerland, 23–27 April 2007*, pp. pp.

Zebker, H. A., P. A. Rosen, R. M. Goldstein, A. Gabriel, and C. L. Werner (1994, October-10). On the derivation of coseismic displacement fields using differential radar interferometry: The Landers earthquake. *Journal of Geophysical Research 99*(B10), 19617–19634.

Zebker, H. A. and J. Villasenor (1992, September). Decorrelation in interferometric radar echoes. *IEEE Transactions on Geoscience and Remote Sensing 30*(5), 950–959.

Improving
Persistent Scatterer Interferometry Results
for Deformation Monitoring
(Case study on the Gardanne mining site)

Master of Science Geomatics - Thesis

Sami Samiei-Esfahany
August 2008

Mathematical Geodesy and Positioning (MGP)
Department of Earth Observation and Space Systems
Faculty of Aerospace Engineering
Delft University of Technology